Doctoral Thesis

Quantum field theory on the lattice: approximate and exact methods, with applications beyond the standard model

Author(s):
Akerlund, Oscar

Publication Date:
2016

Permanent Link:

https://doi.org/10.3929/ethz-a-010694339 →

DISS. ETH NO. 23485

QUANTUM FIELD THEORY ON THE LATTICE: APPROXIMATE AND EXACT METHODS, WITH APPLICATIONS BEYOND THE STANDARD MODEL

A thesis submitted to attain the degree of
DOCTOR OF SCIENCES of ETH ZURICH
(Dr. sc. ETH Zurich)

presented by

OSCAR CARL ÅKERLUND
MSc ETH Physics, ETH Zurich
born on 01.11.1988
citizen of Sweden

accepted on the recommendation of

Prof. Dr. Charalampos Anastasiou
Prof. Dr. Philipp Werner
Dr. Philippe de Forcrand

2016

ABSTRACT

Using a combination of exact and approximate methods we study a few different lattice quantum field theory models, ranging from lattice spin models emulating the heavy-dense regime of quantum chromodynamics, over Higgs-Yukawa models as a proxy for the Higgs sector in the standard model, to pure Yang-Mills theories on the lattice.

The approximate methods consist mainly of extended mean field theory, which has been adapted to the case of quantum field theories from its more general sibling dynamical mean field theory, which is mainly used in condensed matter physics. We also introduce mean distribution theory, which is a generalization of mean field theory which determines not only mean values of fields, but whole distributions, in a self-consistent manner.

First and foremost, we extend the concept of extended mean field theory by applying it to a series of models of increasing complexity. Starting from the complex ϕ^4 theory, which suffers from a "sign problem" in the usual formulation, we show that extended mean field theory works very well for theories with a Gaussian fixed point and we are able to reproduce the phase diagram of the model, obtained by exact worm-algorithm simulations, to a high accuracy. Next, we study a $\mathbb{Z}_3$ spin model with complex external fields, both with extended mean field theory and with exact Monte Carlo simulations. We show here that in three dimensions the model has non-monotonic spatial propagators, which can be interpreted as a liquid phase. Ultimately this may have implications for the phase diagram of quantum chromodynamics and for experimental signals in heavy-ion collisions.

We also investigate a Higgs-Yukawa model, which is a proxy for the Higgs and fermion sector of the standard model, in the presence of a higher dimension operator. Of particular interest is the finite temperature phase transition of this model, which is relevant in the context of electroweak baryogenesis. We determine the mass scale needed for a first order transition with a Higgs mass given by the experimental value and find that new particles should appear with masses of one to a few TeV in order to make this scenario viable.

Furthermore, we shed light on two concepts related to "beyond the standard model" physics on the lattice. Namely, the spontaneous gauge-symmetry breaking of gauge-Higgs unification and the signatures of conformal symmetry breaking on the lattice.

Finally, we study pure Yang-Mills theories on the lattice. One part of this is a study of compact $U(1)$ gauge theory with a non-conventional, so called "topological" action, which has no classical continuum limit. We demonstrate that it nonetheless reproduces the physics of the standard Wilson action, in a certain sense even with superior properties. The other part is a study of gauge theories, and spin models, with the approximative mean distribution approach, which is applied to models both with standard actions and with topological actions. We find that the mean distribution approach improves, in some cases greatly, the predictions of standard mean field theory. This is in particular the case if a change of variables from symmetry-variant to symmetry-invariant variables is made, e.g. from links to plaquettes for a gauge theory.

ZUSAMMENFASSUNG

Mittels einer Kombination von exakten Methoden sowie Näherungsverfahren untersuchen wir verschiedene Gittermodelle der Quantenfeldtheorie. Die Modelle reichen von Gitter-Spin-Modellen, welche das schwere dichte Regime der Quantenchromodynamik emulieren, über Higgs-Yukawa Modelle als einen Vertreter für den Higgs-Sektor im Standardmodell, bis hin zu reinen Yang-Mills-Theorien auf dem Gitter.

Die Näherungsverfahren stammen im Wesentlichen aus der erweiterten Molekularfeldtheorie, welche aus der allgemeineren dynamischen Molekularfeldtheorie (die vor allem in der Physik der kondensierten Materie verwendet wird) für den Fall der Quantenfeldtheorien angepasst wurde. Wir stellen auch den mittleren Verteilungsansatz vor - eine Verallgemeinerung der Molekularfeldtheorie, die nicht nur die Mittelwerte von Feldern, sondern sogar ganze Verteilungen in einer selbstkonsistenten Weise bestimmt.

In erster Linie erweitern wir das Konzept der erweiterten Molekularfeldtheorie indem wir sie an einer Reihe von Modellen mit zunehmender Komplexität anwenden. Wir beginnen mit der komplexen ϕ^4-Theorie, die in der üblichen Formulierung von einem "Zeichenproblem" leidet, und zeigen, dass die erweiterte Molekularfeldtheorie für Theorien mit einem Gaußschen Fixpunkt sehr gut funktioniert. Wir sind in der Lage das Phasendiagramm des Modells, welches auch durch numerisch exakte Wurmalgorithmus-Simulationen zu erhalten ist, mit einer hohen Genauigkeit zu reproduzieren. Als nächstes untersuchen wir ein $\mathbb{Z}_3$ Spin-Modell mit komplexen externen Feldern sowohl mit der erweiterten Molekularfeldtheorie als auch mit exakten Monte Carlo Simulationen. Wir zeigen hier, dass das Modell in drei Dimensionen nichtmonotone räumliche Korrelationsfunktionen aufweist, was als Hinweis für eine flüssige Phase interpretiert werden kann. Dies kann Auswirkungen auf das Phasendiagramm der Quantenchromodynamik und für experimentelle Signale in Schwerionenkollisionen haben.

Weiters untersuchen wir ein Higgs-Yukawa-Modell, welches einen Vertreter für die Higgs- und Fermionensektoren des Standardmodells darstellt, in Gegenwart eines Operators höherer Dimension. Von besonderem Interesse ist das Phasendiagramm des Modells bei endlicher

Temperatur, das im Zusammenhang mit der elektroschwachen Baryogenese relevant ist. Wir bestimmen die für einen Übergang erster Ordnung benötigte Massenskala, wobei wir die Higgsmassedes experimentellen Wertes als gegeben annehmen, und stellen fest, dass neue Teilchen mit Massen von einem bis wenigen TeV erscheinen sollten, um dieses Szenario rentabel zu machen.

Außerdem geben wir Aufschluss über zwei Konzepte der Physik "jenseits des Standardmodells" auf dem Gitter - die spontane Eichsymmetrie-Brechung der Eich-Higgs-Vereinigung und die Signaturen der konformen Symmetriebrechung auf dem Gitter.

Schlussendlich untersuchen wir reine Yang-Mills-Theorien auf dem Gitter. Ein Teil davon ist eine Studie der kompakten $U(1)$-Eichtheorie mit einer unkonventionellen - sogenannten "Topologischen" Wirkung - die kein klassisches Kontinuumlimit hat. Wir zeigen, dass sie dennoch die Physik der Standard- bzw. Wilsonwirkung wiedergibt, in gewisser Weise mit besseren Eigenschaften. Der andere Teil ist eine Studie von Eichtheorien und Spin-Modellen mit approximativem mittleren Verteilungsansatz, der auf Modelle mit Standardwirkungen als auch mit topologischen Wirkungen angewendet wird. Wir beobachten, dass der mittlere Verteilungsansatz die Prognosen von Standard-Molekularfeldtheorie verbessert, in einigen Fällen sogar signifikant. Dies ist insbesondere der Fall wenn eine Variablentransformation von einer Symmetrie-varianten zu Symmetrie-invarianten Variable besteht, wie zum Beispiel von Links zu Plaquettes im Fall einer Eichtheorie.

PUBLICATIONS

The following publications are included in parts or in an extended version in this thesis:

- Oscar Akerlund et al. „Extended Mean Field study of complex ϕ^4-theory at finite density and temperature." In: *Phys. Rev. D* 90 (6 Sept. 2014), p. 065008. arXiv: 1405.6613 [hep-lat]. URL: http://link.aps.org/doi/10.1103/PhysRevD.90.065008.
- Oscar Akerlund and Philippe de Forcrand. „Deformations of infrared-conformal theories in two dimensions." In: *PoS* LATTICE2014 (2014), p. 243. arXiv: 1410.1178 [hep-lat].
- Oscar Akerlund and Philippe de Forcrand. „Gauge-invariant signatures of spontaneous gauge symmetry breaking by the Hosotani mechanism." In: *PoS* LATTICE2014 (2015), p. 272. arXiv: 1503.00429 [hep-lat].
- Oscar Akerlund and Philippe de Forcrand. „U(1) lattice gauge theory with a topological action." In: *JHEP* 06 (2015), p. 183. arXiv: 1505.02666 [hep-lat].
- Oscar Akerlund and Philippe de Forcrand. „Higgs-Yukawa model with higher dimension operators via extended mean field theory." In: *Phys. Rev. D* 93.3 (2016), p. 035015. arXiv: 1508.07959 [hep-lat].
- Oscar Akerlund and Philippe de Forcrand. „Mean Distribution Approach to Spin and Gauge Theories." In: *Nucl. Phys. B* 905 (2016), pp. 1–15. arXiv: 1601.01175 [hep-lat].
- Oscar Akerlund, Philippe de Forcrand, and Tobias Rindlisbacher. „Oscillating propagators in heavy-dense QCD." in: (2016). Submitted to JHEP. arXiv: 1602.02925 [hep-lat].

The Background chapter is partly based on the publication

- Oscar Akerlund et al. „Dynamical Mean Field Approximation Applied to Quantum Field Theory." In: *Phys. Rev. D* 88 (2013), p. 125006. arXiv: 1305.7136 [hep-lat].

ACKNOWLEDGMENTS

First and foremost, I would like to express my utmost gratitude toward my advisor Dr. Philippe de Forcrand for his unwavering support and guidance, without which this work would never had been positive. I also deeply appreciate his infectious fascination for physics and his cheerful manner, which have made it a truly amazing experience, working in his group.

I would also like to thank Prof. Dr. Charalampos Anastasiou and Prof. Dr. Philipp Werner for accepting to be in the advisory committee and for the interest they have shown in my work.

A special thanks goes to Prof. Dr. Antoine Georges and Prof. Dr. Philipp Werner, for a, for me, very fruitful and instructive collaboration and for their continuous support towards my research.

My time in Zürich would not have been the same without the other members of the group: Dr. Wolfgang Unger, Dr. Jens Langelage, Dr. Hélvio Vairinhos and Tobias Rindlisbacher. I will certainly miss our cappuccino-fueled discussions.

Last, but not least, I would like to thank my family and friends for always being there for me and for giving my other ways to challenge my mind and body. Every time it snows in the alps, I will wish I was once again there, just a phone call away from fresh powder under my skis.

CONTENTS

1 INTRODUCTION 1

2 BACKGROUND 13

2.1 Lattice Quantum Field Theory . . . 13

2.1.1 Lattice Simulations . . . 18

2.1.2 The Sign Problem . . . 19

2.2 Mean Field Theory . . . 20

2.3 Dynamical Mean Field Theory . . . 23

2.4 Extended Mean Field Theory . . . 30

2.4.1 k-integrated Green's functions . . . 37

3 EXTENDED MEAN FIELD STUDY OF COMPLEX ϕ^4-THEORY AT FINITE DENSITY AND TEMPERATURE 41

3.1 Introduction . . . 41

3.2 Complex φ^4 Theory . . . 41

3.3 Mean Field Theory . . . 43

3.4 Extended Mean Field Theory . . . 44

3.4.1 Formalism . . . 44

3.4.2 Finite lattices . . . 47

3.4.3 Observables . . . 47

3.4.4 Extra constraints . . . 49

3.5 Results . . . 51

3.5.1 Finite temperature . . . 52

3.5.2 Dimensional reduction . . . 54

3.5.3 First-order transition . . . 55

4 OSCILLATING PROPAGATORS IN HEAVY-DENSE QCD 59

4.1 Introduction . . . 59

4.2 Model . . . 59

4.2.1 Transfer matrix . . . 61

4.2.2 EMFT solution . . . 63

4.3 Results . . . 68

5 THE HIGGS-YUKAWA MODEL WITH HIGHER DIMENSION OPERATORS VIA EMFT 77

5.1 Introduction . . . 77

5.2 Higgs-Yukawa model . . . 77

5.3 Diagonalizing the Overlap operator for arbitrary constant Higgs field . . . 79
5.4 The effective action and EMFT solution . . . 81
5.4.1 Scale setting and observables . . . 83
5.5 Results . . . 84
5.5.1 The zero-temperature phase diagram . . . 86
5.5.2 Higgs mass lower bound . . . 87
5.5.3 Finite temperature . . . 90
6 GAUGE-INVARIANT SIGNATURES OF SPONTANEOUS GAUGE-SYMMETRY BREAKING BY THE HOSOTANI MECHANISM 95
6.1 Introduction . . . 95
6.2 The Hosotani mechanism . . . 95
6.3 Gauge symmetry breaking seen in a gauge-invariant way 97
6.3.1 Abelian flux . . . 98
6.3.2 Magnetic monopoles . . . 101
7 DEFORMATIONS OF INFRARED-CONFORMAL THEORIES IN TWO DIMENSIONS 105
7.1 Introduction . . . 105
7.2 Deformed correlators . . . 105
7.3 The 2d critical Ising model . . . 106
7.4 The Sommerfield model . . . 109
7.4.1 On the lattice . . . 112
7.4.2 Results . . . 112
8 $u(1)$ LATTICE GAUGE THEORY WITH A TOPOLOGICAL ACTION 115
8.1 Introduction . . . 115
8.2 The action . . . 115
8.3 Magnetic monopoles . . . 117
8.3.1 Creating monopoles . . . 117
8.4 The Helicity modulus . . . 119
8.5 Continuum limit . . . 121
8.6 Free energy . . . 122
8.6.1 1d XY model . . . 122
8.6.2 Higher dimensions and gauge theories . . . 124
8.7 Results . . . 125
9 MEAN DISTRIBUTION APPROACH TO SPIN AND GAUGE THEORIES 133
9.1 Introduction . . . 133

9.2 Method . . . 133
9.2.1 Mean Field Theory . . . 133
9.2.2 Mean Distribution Theory . . . 134
9.3 Spin models . . . 137
9.3.1 Mean link approach . . . 139
9.3.2 Mean distribution approach . . . 140
9.4 Gauge theories . . . 141
10 DISCUSSION 149
10.1 Outlook . . . 154

BIBLIOGRAPHY 157
NOTATION 169
ACRONYMS 171

Figure 1.1 The change of variables from spins s_i (*left panel*) to links l_{ij} (*right panel*) that leads to the Bianchi identity $l_{12}l_{23}l_{34}l_{41}(= s_1 s_2^\dagger s_2 s_3^\dagger s_3 s_4^\dagger s_4 s_1^\dagger) = 1$. . . . 10

Figure 2.1 The shape of the bare potential $V(\varphi)$ in the ϕ^4-theory for $m_0^2 > 0$ (*left panel*), for $m_0^2 = 0$ (*middle panel*) and for $m_0^2 < 0$ (*right panel*). The potential is always $\mathbb{Z}_2$ symmetric but a spontaneous breaking of the symmetry and a second order phase transition occur at $m_0^2 = 0$ (classically), when the ground state chooses either the left or the right minimum. 14

Figure 2.2 Graphical interpretation of the cavity method where the action (2.37) is decomposed into an internal part, S_{int}, an external part, S_{ext}, and an interaction part, ΔS. The external degrees of freedom are then integrated out after a Taylor-expansion of the interaction, $\exp(-\Delta S)$. 28

Figure 2.3 Schematic depiction of the Dynamical Mean Field Theory (DMFT) procedure. For a given quartic coupling λ and either κ or ϕ_{ext} fixed we make a guess for Δ and the non-fixed variable. This defines an impurity action via eq. (2.48). We then solve this effective model for the Green's function and the expectation value of the field, $\langle\varphi\rangle$. The local Green's function of the full model is approximated via eq. (2.33). The self-consistency equations (2.34) and (2.35) are then used to calculate new values for Δ and ϕ_{ext} or κ. This procedure is iterated until the self-consistency equations are satisfied. 31

Figure 2.4 The frequency-dependent part of the self-energy, normalized to that of the inverse free propagator (i.e. divided by 2κ)), for $\lambda = 1$ ($d = 2, 3$) and $\lambda = 2$ ($d = 4$). The self-energy is only weakly frequency-dependent, especially for larger dimension, and can be further approximated by a constant, in the Extended Mean Field Theory (EMFT) approximation. 32

Figure 2.5 The tricritical quartic coupling for EMFT as a function of dimension. The critical dimension at $\lambda = 0$ is $d_c(0) \approx 4.00$. The inset shows a power law behavior as d approaches $d_c(0)$. 38

Figure 3.1 The relative deviation of the critical chemical potential μ_c due to finite size effects as a function of the spatial extent of the lattice, L, on an $L^3 \times \infty$ lattice. We fit the amplitude of a sum of Yukawa potentials, eq. (3.37), taking mirror particles up to the distance $r_{\max}$ into account. In both cases the common amplitude of the Yukawa potentials is the only free parameter. The mass is fixed to $\mu_c(\infty)$. 53

Figure 3.2 $(T/\mu_c(T=0), \mu/\mu_c(T=0))$ phase diagram of complex φ^4 theory at $\lambda = 1$ obtained by EMFT and world line Monte Carlo (Gattringer and Kloiber [50]). The two different blue symbols correspond to different observables used in determining the transition point, $\times$ for the variance of φ and $*$ for the density. We have used two values of η and the results agree very well for both. 54

Figure 3.3 The density n, eq. (3.22), as a function on μ for a few different temperatures, $T/\mu_c \equiv 1/(N_t \mu_c(T = 0))$, at $\lambda = 1$, $\eta = 9$ (*left panel*) and $\lambda = 1$, $\eta = 7.44$ (*right panel*). The Monte Carlo data [50] were obtained on a $N_s^3 \times N_t$ lattice with $N_s = 20$ for $\eta = 9$ and $N_s = 24$ for $\eta = 7.44$. The small temperature differences come from slightly different values of $\mu_c(T = 0)$, see table 3.1. The EMFT results are obtained in the thermodynamic limit, i.e. $N_s = \infty$. 55

Figure 3.4 The expectation value of the field, $\langle \mathrm{Re}\varphi \rangle$ (*left panel*), and the correlation length, ξ (*right panel*), as a function of the distance to the critical chemical potential for a few different temperatures at $\lambda = 1$ and $\eta = 7.44$ on a log-log scale. We see how the power law changes from 0.5 at zero temperature to approximately $1/3$ at finite temperature for both observables. To increase readability the curves have been multiplied by $c_T = 15, 5, 1$ and 0.1, going from top to bottom. 56

Figure 3.5 The expectation value of the field at the chemical potential where $\partial \langle \varphi \rangle / \partial \mu = \infty$ as a function of the temperature, both made dimensionless by division by $\mu_c(T = 0)$. 57

Figure 4.1 Phase diagram of the $1d$ $\mathbb{Z}_3$ spin model in the (h_R, h_I)-plane for fixed $\beta = 0.08$. The crystalline phase III is outside the region of parameter space where the worm algorithm can be applied but the liquid phase II is susceptible to lattice simulations. For a more detailed description of the phases see the text. The phase diagram is periodic in h_I with period $\pi/\sqrt{3}$ 62

Figure 4.2 Phase diagram of the $3d$ three-states Potts model at fixed $\beta = 0.08$ obtained by EMFT. The thick red lines are disorder lines where the mass spectrum turns complex and on the dashed blue lines the real part of the mass vanishes. Those lines bound the region of convergence of EMFT. Inside the wedge bounded by the thin black lines the model (4.2) is sign-problem free and the blue region marks the image of the map from the standard $\mathbb{Z}_3$ model to the flux-tube model of [38]. 67

Figure 4.3 Two components of the spin-spin correlator in one dimension for $\beta = 0.5, e^{-M/T} = 0.02$ and $\mu/T = 3.689$. There is a clear oscillation in both correlators and the result agrees perfectly with the exact result obtained using the transfer matrix. The complex mass is given by $m_\pm \approx 1.306 \pm 0.663i$. 69

Figure 4.4 The different junctions allowed in the flux-variable representation of the $\mathbb{Z}_3$ model described in the text. The red crosses represent quarks and the lines represent the directed flux-tubes. The junction is located in the center of each network where the flux sums up to three. Note that the quarks bounding the network may also be replaced by arbitrary larger networks of charge one. In one dimension only junction A is possible. The three-dimensional junction D is only present in dimension three or higher. 70

Figure 4.5 The junction-junction correlator in one dimension for $\beta = 0.5, e^{-M/T} = 0.02$ and $\mu/T = 3.689$ (*left panel*) and for $\beta = 1.2, e^{-M/T} = 0.0042$ and $\mu/T = 4$ (*right panel*). The signal of oscillation is even clearer than in the spin-spin correlator since this observable is less noisy, cf. fig. 4.3. The fits are given by eq. (4.4) with the mass fixed at the value obtained with the transfer matrix. . . . 70

Figure 4.6 *Left*: the masses obtained by EMFT as a function of $\tanh \mu/T = h_I/h_R$ for fixed $\beta = 0.08$ and $e^{-M/T} = 0.05$. *Right*: imaginary part versus real part of the complex mass, for the same parameters as in the left panel. The feature that the real part rises approximatively linearly with the imaginary part is generic, as is the fairly large value of the real part at $\mu = 0$. In the part of the curve to the left of the cusp, both masses are real and their half-difference is shown as a function of their half-sum. 71

Figure 4.7 The correlator of the imaginary part of the spins for three different chemical potentials μ at fixed $\beta = 0.08$ and $e^{-M/T} = 0.05$. The minimum of the correlator moves towards zero and its width decreases as μ increases, suggesting that the imaginary part of the mass increases with μ, as expected. The significant staggered contribution to the correlator makes a fit to the data difficult. The data sets are shifted vertically for clarity and the data points at $r \leq 1$ are far above the shown data points, i.e. we have zoomed in on the minimum of the correlators. 72

Figure 4.8 The correlator of the absolute value of the junction number (*left panel*) and the correlator of the junction number (*right panel*) for $\beta = 0.08, e^{-M/T} = 0.05$ and $\mu/T = 3.3$ on a 12^3 lattice. The depletion in the left correlator and the enhancement in the right correlator around distance 2 support the proposition that the system behaves as a liquid. However, the strong staggered character still leaves some doubt. In the right panel, the data point at $\sqrt{2}$ and 2 are far below 0.99 and are omitted such that it can be clearly seen that the points at $\sqrt{3}$ and $\sqrt{5}$ are above 1. 73

Figure 4.9 The correlator of the absolute value of the junction number (*left panel*) and the correlator of the junction number (*right panel*) for $\beta = 0.26, e^{-M/T} = 0.04$ and $\mu/T = 3$ on a 16^2 lattice. The depletion in the left correlator and the enhancement in the right correlator around distance 2 is similar to what is seen in three dimensions, see fig. 4.8. In this case the correlators on both sublattices shows a maximum in the right panel, but there is a rather large phase difference between the two components. 74

Figure 4.10 Histograms of the distribution of flux-network size, the number of junctions in a network and the network charge for $\beta = 0.08, e^{-M/T} = 0.05$ and $\mu = 2.0$ on a 12^3 lattice. 75

Figure 5.1 The Higgs vacuum expectation value in lattice units as a function of the coupling κ at various λ, for $\lambda_6 = 0.1$ (*left panel*) and $\lambda_6 = 1$ (*right panel*). The solid lines are EMFT calculations from this work and the pluses and dashed lines are full Monte Carlo simulations and Contraint Effective Potential (CEP) calculations respectively, both taken from [60]. The EMFT results follow the Monte Carlo data closely for both values of λ_6, whereas the CEP calculation gives reasonably accurate results for the upper, perturbative value only. 85

Figure 5.2 Finite volume relative correction to the Higgs mass for two different lattice spacings calculated with EMFT with $\lambda_6 = 1/10$ and $M_h = \xi^{-1} = 125$ GeV. The horizontal line corresponds to a 50% correction. In order to see the asymptotic $(\xi/L)^3$ corrections due to the massless Nambu-Goldstone modes, rather large lattices are needed, which poses a challenge to full Monte Carlo simulations. In EMFT one can avoid the problem of thermodynamic extrapolation entirely by working directly in the thermodynamic limit. 86

Figure 5.3 The tricritical point at zero temperature. For λ below the line the transition is first order and above it is second order. 87

Figure 5.4 Zero- and finite-temperature transition in the (λ, κ)-plane at fixed $\lambda_6 = 1/4$. The transition turns from second to first order at the first-order endpoint marked by the star. The color of the line denotes the order of the transition, blue for second order and red for first order. As the lattice size is reduced in the temporal direction the endpoint moves along the arrow, and thus the gray shaded area marks the region in the plane where the finite temperature transition is first order. 88

Figure 5.5 The Higgs mass M_h as a function of aM_h for various combinations of aM_{BSM} and λ, together with the Standard Model (SM) lower bound on the Higgs mass obtained at $M_{\text{BSM}} = \infty$ and $\lambda = 0$. In the presence of a ϕ^6 operator a negative value of λ is allowed and the Higgs mass can be lowered well below the SM bound, as indicated by the arrows. 90

Figure 5.6 The N_t dependence of the tricritical point for $\lambda_6 = 1/4$. The trajectory is very well described by a straight line. 92

Figure 5.7 The critical Higgs mass below which the finite temperature transition is first order for various values of aM_{BSM}. The color coding gives the transition temperature in GeV. The 3 curves give a measure of the sensitivity of our effective theory to the cutoff. A higher cutoff makes the transition weaker. 92

Figure 5.8 The critical Higgs mass below which the finite temperature transition is first order for $aM_{\text{BSM}} = 2$ and different strengths of the transition measured in terms of ϕ_c/T_c where ϕ_c is the critical Higgs vev at the transition. The color coding gives the transition temperature in GeV. 93

Figure 5.9 The critical Higgs mass below which the finite temperature transition is first order for various values of aM_{BSM} with and without the SM fermions. The correction due to the fermions (shown by the arrows) is small and of indefinite sign. 94

Figure 6.1 Contour lines of the effective potential $V_{\text{eff}}(\text{Tr}P_5)$ in the two independent angles of P_5, resulting from different matter contents and boundary conditions in the extra dimension. Black dots mark the minima in each case. 96

Figure 6.2 Mass squared of the Higgs field, as a function of the size of the extra dimension, for two adjoint fermions. In the split phase, the two Abelian components of the Higgs field have different masses. Perturbative calculation and figure from [40]. 98

Figure 6.3 Average xy and xz plaquettes in a $U(1)$ system, under the introduction of one unit of xy magnetic flux every 50 sweeps. The dotted line is the leading prediction. Flux states are long-lived and cause a shift of the in-plane plaquette. . . . 99

Figure 6.4 In an $SU(3)$ system in the reconfined phase ($U(1) \times U(1)$), magnetic flux is introduced in the xy plane. The corresponding shift in the xy plaquette, normalized to that in a pure $U(1)$ system, is shown for several flux combinations in the λ_3 and λ_8 subgroups. The dotted lines show the classical predictions. After 1000 sweeps, the gauge-symmetry breaking potential is turned off: the full gauge-symmetry is restored and the flux states decay immediately. 101

Figure 6.5 (*left*) DeGrand-Toussaint magnetic monopole in an elementary cube of size a. (*right*) The same construction on the scale L of the whole lattice ensures the presence of a magnetic monopole somewhere inside. Charge-conjugated boundary conditions are required to obtain non-zero fluxes at the boundary. 103

Figure 6.6 (*left*) Minimum action of a $U(1)$ magnetic monopole as a function of the size L of the cubic lattice. The $1/L$ correction is caused by the cubic array of image-charges with alternating signs, and its magnitude is exactly given by Madelung's constant. (*right*) Same, for a $U(1)$ magnetic monopole in the λ_3 or λ_8 sector of an $SU(3)$ system in the reconfined ($U(1) \times U(1)$) phase. The two types of monopoles have different masses. The $1/L$ correction is given by the correspondingly rescaled Madelung constant. 103

Figure 7.1 Zero-momentum correlators (*left*) and effective masses (*right*) of the critical $2d$ Ising model for various lattice sizes $L \times (\tau L)$. Note the false plateau of the effective mass far away from the lowest mass for $\tau = 1$. 109

Figure 7.2 (Shifted) "unparticle" mass, $m_{\mathcal{O}}$, as a function of the bare mass deformation, m_q, and three different strategies to improve the data collapse. Note that the exact value of the anomalous mass dimension is $y_m = 1$. The results are obtained with periodic boundary conditions. 113

Figure 8.1 Forbidden regions (hatched areas) and allowed regions (black lines) for the angle of a link surrounded by three (the others are omitted for clarity) staples s_i. When the restriction angle $\delta_{\max} > \pi/2$ (*left panel*) the region can be disconnected whereas if it is smaller than $\pi/2$ (*right panel*) it will always be connected. $\delta_{\max}$ is the angle between an arrow and the edge of the hatched area opposite to it. 116

Figure 8.2 The smallest possible nontrivial loop of monopoles world lines which has Euclidean length $2\sqrt{2}a$. The y and z dimensions are collapsed into one so that each cube is represented by a plaquette and each plaquette by a link. The fat link represents the plaquette shared by all four cubes which contain a monopole. A $+(-)$ in a plaquette symbolizes a positively(negatively) charged monopole in the corresponding cube. 118

Figure 8.3 Monopole creation with a single link update (*upper panel*) and a multiple link update (*lower panel*). The fat links are the ones updated and the flux of π is spread over the plaquettes on the right which means that the single link update is ergodic down to $\delta_{max} = \pi/2$ and the two-link one to $\pi/3$. 119

Figure 8.4 The derivative $\partial f/\partial\delta_{\max}$ of the free energy density $f = -V^{-1}\log Z$ for the $2d$ XY-model (*left panel*) and the $4d$ $U(1)$ gauge theory (*right panel*) as obtained from Monte Carlo simulations with a topological action. There is a clear distinction between the smooth derivative in the XY-model which has an infinite order phase transition and the discontinuous behavior, signaling a first order transition, in the $U(1)$ gauge theory. The vertical line marks the critical restriction $\cos\delta_c$. In the case of the XY-model it has been taken from [23] where it was extracted from a fit of the diverging correlation length. 125

Figure 8.5 The monopole density n for the topological action (*left panel*) and the Wilson action (*right panel*). For the Wilson action the first order nature of the transition is rather evident even for a 12^4 lattice whereas for the topological action we have to go to much larger lattices to see a fairly distinct jump. 127

Figure 8.6 The helicity modulus h for the topological action (*left panel*) and the Wilson action (*right panel*). The lines are the best fit to eq. (8.15), which describes the data in the confining phase (the model assumes a constant h in the Coulomb phase) very well for both actions. 127

Figure 8.7 The probability distribution of the monopole density close to the transition for various volumes (*left panel*) and the corresponding Monte Carlo history for the 24^4 volume (*right panel*). The distributions are rescaled in such a way that one peak is at -1 and the other at $+1$. That way the separation of the peaks in relation to the widths can be directly compared between different volumes. It is evident that the two peaks become more distinct for larger volumes which indicates a first order transition. Also the obvious tunneling between two different states in the Monte Carlo history backs up this statement. . . 128

Figure 8.8 The Creutz ratios $\chi(R)$ given by eq. (8.16) as well as an $R \to \infty$ extrapolation assuming corrections of the form e^{-R} as a function of the restriction $\cos\delta_{\max}$ obtained on an 8^4 lattice. There is a clear transition between a confining phase with nonzero string tension and a deconfined phase with an perimeter law for the Wilson loops. . . . 129

Figure 8.9 The monopole density in the Coulomb phase as a function of the renormalized coupling β_R, for the topological and the Wilson actions. The different rates of decay could be attributed to different lattice spacings for the two actions. . . 130

Figure 8.10 The monopole density for the topological action as a function of the restriction. There seems to be a smooth transition from an exponential decay to a power law at $\cos\delta_{\max} \approx -0.12$. 131

Figure 9.1 The distribution of plaquettes angles $p(\theta_P)$ in the $4d$ $U(1)$ lattice gauge theory with the Wilson action close to the critical coupling (*left panel*) and with the topological action at the critical restriction δ_c (*right panel*) obtained by Monte Carlo on an 8^4 lattice and by the mean distribution approach, together with the Haar measure. . . . 137
Figure 9.2 Two choices of domains of live links for $2d$ spin models. The live links are denoted by the solid lines, whereas the dashed lines denote links which are assumed to take mean values or to be distributed according to the mean distribution. The left panel shows the unique domain with one live link and the right panel shows one of many domains with nine live links. 139
Figure 9.3 (*left*) Mean-field and mean-link approximation in the $2d$ Ising model for two choices of live domains. (*Right*) Mean-link and mean-distribution in the $2d$ $\mathbb{Z}_4$ model. In the Ising case, mean-link and mean-distribution are equivalent. 142
Figure 9.4 The mean link in the $2d$ XY spin model as a function of the Wilson coupling β (*left panel*) and of the restriction δ (*right panel*) from Monte Carlo, from the mean link and from the mean distribution methods. 142
Figure 9.5 The mean plaquette in the $4d$ $U(1)$ gauge theory as a function of the Wilson coupling β (*left panel*) and the restriction δ (*right panel*) from Monte Carlo, and from the mean plaquette and the mean distribution methods. 143
Figure 9.6 The monopole density in the $4d$ $U(1)$ gauge theory as a function of the Wilson coupling β (*left panel*) and the restriction δ (*right panel*) from Monte Carlo and the mean distribution method. 144

Figure 9.7 The average plaquette for the $SU(2)$ gauge theory as a function of the Wilson coupling β (*left panel*) and the restriction α (*right panel*) from Monte Carlo simulation, the mean plaquette method and the mean distribution method. For comparison the mean link result obtained with the formalism in [43] is also shown in the left panel. 147

LIST OF TABLES

Table 3.1 Comparison of the critical chemical potential, $\mu_c(T = 0)$ of four-dimensional complex φ^4-theory at $\lambda = 1$ obtained by mean field (MF) theory, EMFT, Monte Carlo [50] and complex Langevin [2]. 51

Table 5.1 Separations of three scales in units of the inverse lattice spacing at the tricritical point for different values of aM_{BSM}. 93

1

INTRODUCTION

Except in highly symmetric special cases, quantum field theorys (QFTs) can not be solved exactly. For weakly coupled theories, perturbation theory typically works well, but there are many examples, for example quantum chromodynamics (QCD) at low energies, where non-perturbative effects are essential. Since the seminal work of Wilson on Lattice QCD [100], the lattice regularization, together either with analytic or computational methods, has been the foremost approach for studying such models. With ever-increasing computer power, lattice calculations of in particular QCD have reached impressive accuracy and are now in the state of both yielding experimental predictions as well as vital input to perturbative calculations. However, some problems remain out of reach from conventional computational methods, due to for instance exponential degradation of the signal-to-noise ratio as the volume in the calculation is increased. To ameliorate the situation several directions should be considered. On the one hand, it is always of interest to design or improve approximate methods which capture at least the qualitative features of the models they are applied to. On the other hand, constructing new, exact methods or reformulating the original problem may also allow progress in the understanding of previously impenetrable models.

Among the most serious obstacles in lattice QFT and computational physics is the so-called "sign problem," [1] which spoils the probabilistic interpretation of the partition function and thus a foundation of the otherwise powerful Monte Carlo method. A sign (or phase) problem may have different origins. On the one hand, the statistics of the fields might cause some configurations to appear with a negative (fermions) or complex (anyons) weight. While it is possible, in principle, to consider suitable subsets of the configuration space [25] or to use another set of variables [35] to end up with only non-negative weights, appropriate subsets or new variables have only been found for a small number of models so far. On the other hand, the action itself can be complex,

1 Which is to say that the Boltzmann factors in the partition sum are not all non-negative real numbers.

leading to sign problems even in bosonic systems. A typical example for this case is when a chemical potential μ is introduced, which creates an asymmetry between particles and antiparticles. Also here, the sign problem can sometimes be solved by considering a different set of variables, like in the world-line Monte Carlo approach [45, 50]. Recent progress in the understanding of the complex Langevin equations [1, 3] and gauge cooling [88] has promoted yet another approach for simulating models with complex actions.

Mean field (MF) methods, although approximative, can be useful alternatives. They are computationally cheap, and many results can be obtained analytically, or at least semi-analytically. Furthermore, most of the time the symmetries of the Lagrangian can be used to make the action real, hence avoiding the sign problem. However, standard MF methods have some obvious shortcomings. Although MF theory is known to reproduce the correct qualitative critical behavior at and above the upper critical dimension d_{uc} (up to logarithmic corrections at d_{uc}), quantitative predictions are usually very approximative. Another shortcoming of MF theory is that it cannot be used to determine correlation functions or to study nonzero temperature. A simple extension of mean field theory which aims to overcome these limitations is Extended Mean Field Theory (EMFT) [80, 10], which incorporates self-consistency at the level of the propagator.

EMFT can be seen as a simpler variation of Dynamical Mean Field Theory (DMFT) which is a method widespread in the condensed matter community and has been applied to both fermionic, bosonic and mixed systems. As its name suggests it is a variation on standard MF theory. The core merit of the method is the way an approximation to the two-point correlation function is used in the self-consistency equations, which leads to several nice properties. There is for example direct control over the lattice on which the full theory is formulated, although the effective EMFT action only contains the field at a single point in space-time. Additionally it is possible to extract an approximation of the mass through the correlation function.

Since MF methods in general, and EMFT in particular, maps the a higher-dimensional model to a zero-dimensional one, the volume scaling in the sign problem is removed and it is expected that EMFT will not suffer from any sign problem. In many cases it is even possible to completely get rid of the sign problem by a convenient choice of

variables. In chapter 3 we apply EMFT to a model with a sign problem due to a non-zero chemical potential.

It is also duly noted that some models with complex actions display interesting physically phenomena which are closely related to the very fact that the action is complex. An example is the possibility of models with complex saddle point to develop a complex spectrum, which leads to oscillating propagators.

Oscillating propagators have been the subject of several studies and carry important information about the underlying physics. Patel [81, 83] has argued that many-body correlations among the hadrons produced in heavy-ion collisions may be oscillatory and has shown how those signals can be related to properties of the quark-gluon plasma (QGP) [82]. The underlying idea is that the QGP can be described as a network of quarks and of flux tubes into which the gluonic degrees of freedom are concentrated. The flux tubes are assumed to interact mainly via three-point vertices, from here on called junctions, where three flux tubes join together to form an $SU(3)$ singlet. It has been suggested that this system behaves like a liquid with an oscillating two-body spatial correlation between junctions and this structure might remain as the QGP hadronizes. This would be the case if the string network breaks up via pair production rather than via coalescence of junctions. If that happens, then the oscillatory signature should persist also in the two-body correlations of transversely outgoing hadrons.

Another situation when oscillating correlation functions may occur is in a possible crystalline phase in the QCD phase diagram, which may occur at high density and low temperature. The existence of such a phase is supported by the exact solution of the $(1+1)$-dimensional Gross-Neveu (GN) model at high density [95, 48]. While the system described above may show liquid-like correlations, i.e. exponential decay modulated by a cosine, the signature of a crystalline phase would be a purely trigonometric correlation function.

To understand better when to expect such non-monotonic behavior, Ogilvie et al. have in a series of papers [71, 78, 79] studied models which break charge conjugation $\mathcal{C}$, but remain invariant under the combined action of $\mathcal{C}$ and complex conjugation $\mathcal{K}$. QCD at nonzero chemical potential μ has this property, but also simpler models like the Polyakov-Nambu-Jona Lasinio (PNJL) model with nonzero μ, $SU(3)$ (Polyakov loop) spin models with nonzero μ, and even the three-state Potts model with nonzero μ have the same property. So before tackling full QCD

one can hope to learn the implications of this symmetry pattern from simpler models, which may even in some cases be mapped to limiting cases of QCD itself. It is well known that for QCD, the expectation value of the Polyakov loop differs from the expectation value of its Hermitian conjugate, $\langle \mathrm{Tr}_F\, L \rangle \neq \langle \mathrm{Tr}_F\, L^\dagger \rangle$ when the chemical potential μ is nonzero. However, the free energies are real because of the $\mathcal{CK}$ symmetry. As a further consequence of the breaking of $\mathcal{C}$, the transfer matrix T is not Hermitian, which means that the eigenvalues are not all necessarily real. Because of the invariance under $\mathcal{CK}$, however, if λ is an eigenvalue of T, then so is λ^*, i.e. the eigenvalues are either real or occur in complex conjugate pairs. This is interesting because it implies, in the case where complex eigenvalues occur, that the Polyakov loop correlator is non monotonic. In general three scenarios are possible. Firstly, all eigenvalues can be real and the correlator is a conventional, exponentially decaying function. Secondly, if the largest eigenvalue is real and the next two are a complex-conjugate pair, then the correlator also decays exponentially but is modulated by a cosine, and the system behaves as a liquid. Finally, if the largest (in magnitude) eigenvalue is part of a conjugated pair, then the correlator is a pure trigonometric function and a crystalline behavior is observed. All these three cases have been found by Ogilvie et al [71] in 1-dimensional models, which are to be seen as dimensionally reduced effective models of $(1+1)$-dimensional QCD at finite temperature, where the complete phase diagram can be obtained using transfer-matrix methods. Recently [79] it has been proposed that also higher dimensional models show these characteristics, based on the fact that the 1-dimensional solution can be seen as the first order in a character expansion. It has, however, to our knowledge, not been demonstrated with first-principles lattice simulations that this is actually the case.

Chapter 4 is devoted to the study of the $\mathbb{Z}_3$ spin model with nonzero chemical potential μ in 1 and 3 dimensions, by the use of EMFT and exact lattice simulations.

There are also other situations where a method like EMFT can be of interest. For example, models which includes dynamical chiral fermions are extremely expensive to simulate due to technical reasons. For such models, a fast but accurate approximative method can be very valuable, in part because it can guide the Monte Carlo simulations so that valuable computer resources are spent where they yield maximum return, but also because the approximative method can give reliable

results about the properties of the model. One such model is the Higgs-Yukawa sector of the Standard Model (SM), which contains the Higgs field and the massive SM fermions. It is generally accepted that the SM is an effective field theory which needs to be extended by an ultraviolet (UV) completion at some energy scale. Depending on this scale, higher dimension operators may or may not be relevant for the infrared (IR) physics in the SM. Especially interesting is the possibility of a first-order electroweak finite temperature (EWFT) transition, which is relevant in the context of electroweak (EW) baryogenesis. The nature of the transition is sensitive to both the Higgs boson mass and the scale of the inevitable new physics.

Even before the Higgs boson was discovered several studies where the SM couplings were run to very large energies were conducted. This resulted in both upper and lower bounds on the Higgs mass stemming from the triviality of the Higgs self-interaction and the EW vacuum stability, respectively. Sandwiched between these bounds is a small region of Higgs masses for which the SM can be run at least up to the Planck scale [46, 28]. Due to the huge success of the SM when it comes to explaining results from accelerator experiments it was predicted that the Higgs mass would indeed lie inside this region and that the UV completion of the SM would enter only at the Planck scale where gravity becomes important. As the Atlas and CMS experiments announced the discovery of a Higgs-like particle at 125 GeV, which is at least very close to the special region, these speculations about no new physics before the Planck scale got a lot of deserved attention. It is certainly interesting and important to thoroughly investigate this possibility, see [46] and references therein.

However, the apparent special value of the Higgs mass of course in no way excludes new physics at a lower scale and we will in this paper deal with generic aspects of UV completions at a fairly low scale of a few to tens of TeV. It is well motivated to depart from the arbitrarily postulated quartic self-interaction of the Higgs field for the following reason. The SM does not include dark matter or gravity, so it is only an effective theory anyway, and there is no reason to assume a renormalizable Higgs sector. We may add higher-dimension operators, which may not directly be relevant for the low energy physics but which can, for example, play an important role for the stability of the EW vacuum or in the context of EW baryogenesis, in an effective field theory way. This will of course drastically change the running of the

SM coupling constants so the question of whether the Higgs mass puts the universe in a near critical state or not loses its relevance in this context. For the purpose of generality it is useful to consider generic higher-dimension operators instead of a specific UV extension of the SM because then aspects common to a broad class of models can be investigated. For example, it has previously been demonstrated [55, 56, 44], using the Functional Renormalization Group (FRG) and various simplified versions of the SM, that the Higgs lower mass bound can indeed be lowered when higher dimension operators are included.

Since the Yukawa coupling of the top quark is of order one, and because the phase transition of interest takes place at a finite temperature, it is desirable to use a non-perturbative approach, i.e. a lattice regularization of the model; for a perturbative study, see [57]. Unfortunately, it is not known how to regularize chiral fermion interactions on the lattice, which makes it impossible to study the full SM using a lattice discretization. There are two sectors of the SM which can be studied separately, the gauge-Higgs sector, consisting of the weak gauge bosons and the Higgs field, and the Higgs-Yukawa sector, consisting of the Higgs field and the SM fermions. For a study of the first, see [67, 41, 16, 91, 92]. In chapter 5, we investigate the latter, because of the large contribution to the SM Higgs sector from the Higgs-top interaction. The use of EMFT in this models allows us to obtain results with a computing effort orders of magnitude smaller than with full Monte Carlo simulations of the same model [32, 60, 36], at the same time as giving access to the physical region in parameter space at which the Monte Carlo simulations suffer from a sign problem. See also [31] for a study of the Higgs-Yukawa model with an additional heavy fourth fermion family.

When it comes to questions about what the UV completion of the SM is, one can but speculate. There are numerous possible scenarios and so far the experiments at the Large Hadron Collider (LHC) has been rather reluctant to give any clues. One suggestion that has seen some popularity over the last years is the possibility of extra dimensions, which in some instances can explain the origin of the Higgs field.

Dimensional reduction tells us that QCD at high temperature can be effectively described as a $3d$ Yang-Mills theory, plus an adjoint Higgs field generated by the static mode of the gauge field component A_0, i.e. by the Polyakov loop. Dimensional reduction also occurs in the case of a compact *extra* dimension: a $(4+1)d$ Yang-Mills theory is effectively described as a $4d$ Yang-Mills, plus an adjoint Higgs field

coming from the Polyakov loop P_5 in the extra dimension. This led Hosotani [63, 62], in 1983, to the scenario of "gauge-Higgs unification": by a judicious choice of matter content and boundary conditions in the extra dimension, the minimum of the effective potential for $\mathrm{Tr}P_5$ can be displaced from its trivial value $A_5 = 0$. Then, the corresponding $4d$ adjoint Higgs field acquires a non-trivial vacuum expectation value, which can [partially] break the gauge symmetry of the Yang-Mills theory. While this scenario seems to be disfavored phenomenologically, we are concerned here with a different aspect: how can one diagnose the claimed breaking of *gauge* symmetry? In chapter 6 we will deal with this question in some detail and we will see that the proposal presented there actually applies also to genuine (gauge + Higgs) systems.

Other possible candidates for the physics beyond the Standard Model (BSM) are (near-)conformal theories, for example walking Technicolor. For these models to be phenomenologically relevant, large anomalous dimensions are required at the infrared fixed point, which often cannot be realized at weak coupling. Strongly coupled gauge theories are best studied on the lattice but the lattice is a priori not well suited to study (near-)conformal theories because of explicit breaking of rotational and scale invariance through the UV and IR cutoffs, i.e. the lattice spacing a and the finite extent of the lattice $L_\mu = N_\mu a$, where N_μ is the number of lattice sites in the direction μ. It is therefore of great importance to properly understand how a conformal theory is deformed by the lattice in order to correctly interpret potential remnant signatures of its conformality, this will be addressed in chapter 7.

A further interesting direction of research within the field of lattice QFT is the development of improved actions. In recent years lattice QFT has seen a surge of efforts to construct new lattice actions which aim at improving the approach to the continuum limit. The best-known strategy is that advocated by Symanzik, where irrelevant operators of higher and higher dimension are added to the "standard" (e.g. Wilson plaquette) action, with coefficients adjusted perturbatively or non-perturbatively to cancel discretization errors of the corresponding power in the lattice spacing a [94, 99]. This kind of improvement is thus a parametric one, allowing for a faster approach to the continuum limit than exhibited by the "standard" action.

However, this is not the only possible strategy for improvement. It has long been recognized that departure from the continuum limit is more violent for large fields, so that suppressing these large fields produces

a non-parametric improvement [73]. For instance, this happens when one trades the Wilson action for the Manton action [74], based on the length of the geodesic in group space, or for a "perfect" action [87]: large fields, corresponding to small values of the plaquette trace, are more suppressed than with the Wilson action, and at the same time continuum behavior is better approximated for a given value of the lattice spacing a.

A more radical suppression of large fields is achieved by imposing a strict cutoff: for instance, in a spin model one can demand that neighboring spin angles do not differ by more than a limiting value; or in a gauge theory, one may require that the plaquette trace be larger than a limiting value. The best-known example of the latter is the positive-plaquette action for $SU(2)$ lattice gauge theory [70, 27, 47]. While the approach to the continuum limit is also improved in this strategy, an important side-effect may happen. Localized topological defects can only form if the cutoff is not too restrictive. For instance, an $O(2)$ spin model on a square lattice can support vortices only if the spins can rotate by $\pi/2$ or more between neighboring sites. If not, the disordered phase of this system disappears entirely. Thus, the cutoff may change the phase diagram of the model. A similar situation occurs in lattice gauge theory: as pointed out by Lüscher [69], if the plaquette trace is restricted to "admissible" values greater than about 0.97 (for $SU(2)$), changes in the topological charge become impossible, and topology becomes well defined on the lattice. Topological sectors arise as in the continuum theory.

In chapter 8, we consider the extreme strategy where the action consists *only* of a cutoff. In other words, the action takes only two values: 0 if all cutoff restrictions are satisfied, $+\infty$ if not. This kind of action has been called *topological* [22], because it does not have any classical small-a limit, and the action remains invariant under small admissible deformations of the field. A simple example of topological action for an $O(N)$ spin model is:

$$S = \sum_{\langle i,j \rangle} R_\theta(S_i \cdot S_j), \quad R_\theta(x) = \begin{cases} 0 & x > \cos\theta \\ +\infty & \text{else} \end{cases}. \tag{1.1}$$

Topological actions raise an interesting puzzle: as the constraint between neighboring spins becomes more restrictive, the correlation length increases and diverges; but what is the action associated with

this continuum limit? Several studies have investigated different spin models [22, 21, 23], and it has been shown in analytically solvable $O(N)$ models that the continuum limit is that associated with the usual, sigma-model action. In higher dimensions numerical investigations also support this claim very strongly.

Here we want to investigate the properties of a topological action in a gauge theory, and consider the simplest case, namely compact $U(1)$ lattice gauge theory in 4 dimensions. Aside from the continuum limit, we also want to study the phase diagram of this system. With the Wilson action, a first-order phase transition separates a strong-coupling, confining phase and a weak-coupling Coulomb phase. This phase transition is associated with condensation of magnetic monopoles in the strong-coupling phase [42]. With a topological action, the constraint on the plaquette trace, when restrictive enough, is going to make it impossible for magnetic monopoles to exist. This may completely alter the phase diagram of the theory.

Finally, topological actions may be interesting for algorithmic reasons: it may be computationally easier to move in the space of admissible configurations since they all have the same action. While this does not seem to be a significant effect for the Monte Carlo update of such configurations, in spin models or in the gauge theory we study, we show below that extracting the free energy (or equivalently here, the entropy) is extremely simple numerically, and yields valuable information.

For EMFT, gauge-theories pose great challenges due to the local gauge symmetry and there is no obvious way to apply a method like EMFT to the type of topological action described above. However, it is always of interest to think about other methods that allow easy extraction of approximate results, even though the computer power available for exact simulations is growing at an ever increasing pace. MF methods are often qualitatively reliable in their self-consistent determination of the long-distance physics, and have a wide range of applications, with spin models as typical examples. For a gauge theory, formulated in terms of the gauge links, however, it is questionable what a *mean link* would mean, because of the local nature of the symmetry. This can be addressed by fixing the gauge, but the MF solution will then in general depend on the gauge-fixing parameter. Nevertheless, Drouffe and Zuber developed techniques for a MF treatment of general Lattice Gauge Theories in [43] and showed that for fixed βd, where β is the inverse gauge coupling and d the dimension, the MF approximation can

be considered the first term in a $1/d$ expansion. They established that the MF approximation can be thought of as a resummation of the weak coupling expansion in a particular gauge and that there is a first order transition to a strong coupling phase at a critical value of β. Since it becomes exact in the $d \to \infty$ limit, this MF approximation can be used with some confidence in high-dimensional models [64].

The crucial problem of gauge invariance was tackled and solved by Batrouni in a series of papers [17, 18], where he first changed variables from gauge-variant links to gauge-invariant plaquettes. The associated Jacobian is a product of lattice Bianchi identities, which enforce that the product of the plaquette variables around an elementary cube is the identity element. In the Abelian case this is easily understood, since each link occurs twice (in opposite directions) and cancels in this product, leaving the identity element. In the non-Abelian case the plaquettes in each cube have to be parallel transported to a common reference point in order for the cancellation to work. It is worth noting that in two dimensions there are no cubes, so the Jacobian of the transformation is trivial and the new degrees of freedom completely decouple (up to global constraints).

This kind of change of variables can be performed for any gauge or spin model whose variables are elements of some group. Apart from gauge theories, examples include $\mathbb{Z}_N$-spin models, $O(2)$- and $O(4)$-spin models and matrix-valued spin models. In spin models, the change of variables is from spins to links and the Bianchi constraint dictates that the product of the links around an elementary plaquette is the identity element. A visualization of the transformation and the Bianchi constraint for a $2d$ spin model is given in fig. 1.1.

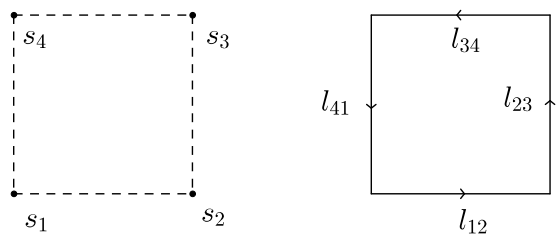

Figure 1.1: The change of variables from spins s_i (*left panel*) to links l_{ij} (*right panel*) that leads to the Bianchi identity $l_{12}l_{23}l_{34}l_{41}(= s_1 s_2^\dagger s_2 s_3^\dagger s_3 s_4^\dagger s_4 s_1^\dagger) = 1$.

Let us review the change of variables for a gauge theory [18]. The original variables are links. The new ones are plaquettes. Under the action of the original symmetry of the model, the new variables transform within equivalence classes and it is possible to employ a mean field analysis to determine the "mean equivalence class". As usual we first choose a set of *live* variables, which keep their original dynamics and interact with an external bath of mean-valued fields. Interactions are generated through the Jacobian, which is a product of Bianchi identities represented by δ-functions

$$\delta\left(\prod_{P\in\partial C} U_P - 1\right), \tag{1.2}$$

where P denotes a plaquette and ∂C denotes the oriented boundary of the elementary cube C. The δ-functions can be represented by a character expansion in which we can replace the characters at the external sites by their expectation, or mean, values. Upon truncating the number of representations, this yields a closed set of equations in the expectation values which can be solved numerically. The method can be systematically improved by increasing the number of representations used and the size of the live domain.

While this method works surprisingly well, even at low truncation, it determines the expectation value of the plaquette in only a few representations. In chapter 9, we propose a method that self-consistently determines the complete distribution of the plaquettes (or links) and thus the expectation value in all representations. This is due to an exact treatment of the lattice Bianchi identities which does not rely on a character expansion. The only approximation then lies in the size of the live domain which can be systematically enlarged, as in any mean field method. It is worth noting that our method works best for small β and low dimensions: it does not become exact in the infinite dimension limit. In this way it can be seen as complementary to the MF approach of [43]. We will however see that the mean distribution approach proposed here actually works rather well for both small and large β.

The rest of this thesis is structured as follows. In chapter 2 some preliminaries to the main body of the thesis are given. In chapter 3 we study complex ϕ^4-theory in four dimensions using EMFT. This model has a sign problem but can still be simulated after a change of variables and thus serves as a benchmark for EMFT. In chapter 4 we look for

signals of liquid-like behavior in the $\mathbb{Z}_3$-spin model with a chemical potential, which serves as a proxy for heavy-dense QCD, using EMFT and exact numerical simulations. We then investigate the EWFT phase transition in the presence of higher-dimension operators by applying EMFT to the Higgs-Yukawa sector of the SM. In the two following chapters we study two phenomena related to BSM physics, the notion of spontaneous gauge-symmetry breaking, related to the Hosotani mechanism and gauge-Higgs unification, in chapter 6 and conformal-symmetry breaking by the lattice, relevant for example in technicolor models, in chapter 7. The last two chapters are devoted to lattice gauge theories. In chapter 8 we study by exact numerical simulations the compact $U(1)$ lattice gauge theory by the use of a special kind of action, called a topological action, which does not have a classical continuum limit. The last chapter 9 introduces another generalization of mean field theory, called the mean distribution approach, which is applied to spin models and lattice gauge theories.

2

BACKGROUND

2.1 LATTICE QUANTUM FIELD THEORY

The path-integral formulation by Feynman has proven to be an invaluable tool to evaluate S-matrix elements in QFTs, be they part of the SM of particle physics or mere toy models. Even though the purist may argue about the mathematical foundations of the path integral, the remarkable calculations, mainly via perturbation theory, which the formalism enables, and their agreement with experimental data can not be contested. However, a naive evaluation of the path integral of even simple field theories inevitably leads to infinities, which need to be tamed by regularization, which generally involves the introduction of an additional, artificial mass scale. Renormalization then ensures that the final, physical result does not depend on any arbitrary parameters. The main work horse of particle physics is perturbation theory, usually coupled with dimensional regularization, which, through heroic efforts by its practitioners, has brought unprecedented agreement between theory and experiment.

However, perturbation theory requires weak couplings to justify the inclusion of only the first few terms in the perturbative expansion. To deal with strongly coupled theories, other methods are needed. To date, the only general purpose, non-perturbative approach to QFTs is to use a lattice regularization, i.e. a discretization of space-time. In fact, introducing a finite lattice to evaluate the path integral on, is a way to make it mathematically well defined, which makes the approach appealing not only from the practitioners point of view. The rest of this section will remind the reader of the main features of QFTs on a lattice.

As usual, the methodology is best explained by a hands-on example, so let us consider the king of all text-book examples, the real ϕ^4-theory, which describes a real-valued, scalar field with a repulsive quartic interaction. In Minkowski space its Lagrangian density is given by

$$\mathcal{L}[\varphi] = \frac{1}{2}\partial_\mu\varphi\partial^\mu\varphi - \frac{m_0^2}{2}\varphi^2 - \frac{g_0}{4!}\varphi^4, \tag{2.1}$$

where m_0 is the bare mass parameter and g_0 is the bare quartic coupling. Despite its simplicity, this model contains some interesting behavior. There is a global $\mathbb{Z}_2$ symmetry and depending on the sign of m_0^2, the potential can have either a single global minimum at $\varphi = 0$ or two global minima at $\varphi = \pm\sqrt{-6m_0^2/g_0}$, and correspondingly a local maximum at $\varphi = 0$. In the latter case, spontaneous symmetry breaking occurs. Since the location of these symmetry-breaking minima goes to zero smoothly with m_0^2, there is a second order phase transition at $m_0^2 = 0$. This description is valid in the classical limit. In the quantum theory the bare parameters will be renormalized such that the transition occurs at vanishing renormalized mass m_R instead. The shape of the potential in the different phases is shown in fig. 2.1.

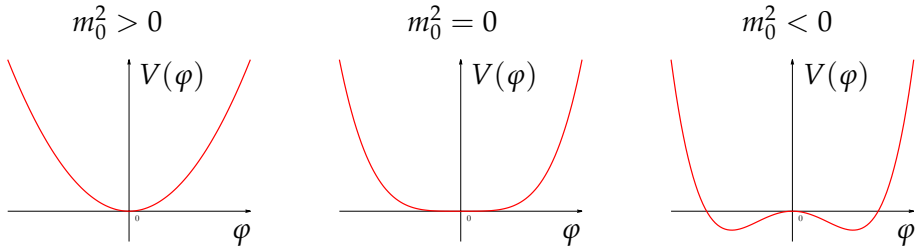

Figure 2.1: The shape of the bare potential $V(\varphi)$ in the ϕ^4-theory for $m_0^2 > 0$ (*left panel*), for $m_0^2 = 0$ (*middle panel*) and for $m_0^2 < 0$ (*right panel*). The potential is always $\mathbb{Z}_2$ symmetric but a spontaneous breaking of the symmetry and a second order phase transition occur at $m_0^2 = 0$ (classically), when the ground state chooses either the left or the right minimum.

The partition function of the theory is then given by the path integral

$$Z = \int \mathcal{D}[\varphi] e^{\frac{i}{\hbar} S}, \tag{2.2}$$

where the action $S = \int \mathrm{d}^d x \mathcal{L}$ is the integral of the Lagrangian density over all of space-time and $\int \mathcal{D}[\varphi]$ formally denotes infinite-dimensional integral over all the fields φ at all points of space-time. As is well known, the i in front of the action leads to the interference between different paths, which is at the core of quantum mechanics. However, from a computational point-of-view, that is an extreme nuisance, which is called the sign (or phase) problem, which makes it exponentially hard to numerically evaluate observables in the path integral formalism. Hence,

the first step to put the theory on a lattice and make it computationally tractable, is to Wick rotate time to the imaginary axis. This will turn the quantum problem into a statistical problem where instead of pure interference, each configuration will be exponentially suppressed with respect to the ground state, with a suppression factor given by the difference of actions.

The Wick-rotated, Euclidean action S_{E} and partition function Z_{E} are given by

$$S_{\mathrm{E}} = \int \mathrm{d}^d x \left(\frac{1}{2} \partial_\mu \phi \partial_\mu \phi + \frac{m_0^2}{2} \varphi^2 + \frac{g_0}{4!} \varphi^4 \right), \tag{2.3}$$

$$Z_{\mathrm{E}} = \int \mathcal{D}[\varphi] e^{-\frac{1}{\hbar} S_{\mathrm{E}}}, \tag{2.4}$$

where d is the dimension of space-time. Since the action is real, $e^{-S_{\mathrm{E}}/\hbar}/Z_{\mathrm{E}}$ plays the role of a probability distribution, i.e. it is the Boltzmann factor in the language of statistical physics, and all the methods of statistical physics are available to analyze the theory. In principle, all information of the quantum problem on the real-time axis is available also in the statistical-physics picture on the imaginary-time axis, but just as the original evaluation of observables is exponentially hard, so is the analytic continuation. However, some static properties of the system, for example the mass spectrum, bound-state structure and scattering phase shifts, are readily measurable also at imaginary times.

We are now ready to discretize Euclidean space-time and make the number of degrees of freedom finite, and thus make the problem computationally tractable. There is no unique way of discretizing Euclidean space, but the most generally used scheme in lattice QFT is to introduce a hyper-cubic lattice and a finite-difference scheme for the derivatives. Any discretization with the correct continuum limit is of course valid, and in general different choices will lead to different discretization errors. A discretization with small discretization errors will make the inevitable continuum extrapolation more robust but also the simplicity of the scheme will play a role in the choice. Another important issue is what to do at the boundary of the lattice. In the end, we are interested in the system in an infinite volume[1], so boundary effects will not play a role, but also here different choices will lead to different corrections to the infinite volume limit. The best choice of

1 Or in a box of finite extent, but then the boundary conditions are of course already determined.

boundary conditions depends on the problem at hand but the general consensus is that periodic boundary conditions are the best choice in most situations.

Taking the lattice to have N_μ sites in direction μ and an isotropic lattice spacing a, it will have linear extents $L_\mu = aN_\mu$ and volume $V = \prod_{\mu=1}^{d} L_\mu$. The total number of lattice sites is $N = \prod_{\mu=1}^{d} N_\mu$. The field φ is defined on the lattice sites and is given by

$$\varphi(x + mN_\mu) = \varphi(x), \quad m \in \mathbb{Z}, \tag{2.5}$$

$$x_\mu = an_\mu, \quad n_\mu = 0, \ldots, N_\mu - 1. \tag{2.6}$$

The space-time integrals will turn into finite sums and field derivative to finite differences

$$\int \mathrm{d}^d x \to a^d \sum_{n_1=0}^{N_1-1} \cdots \sum_{n_d=0}^{N_d-1} \equiv a^d \sum_n, \tag{2.7}$$

$$\partial_\mu \varphi(x) \to \frac{\varphi_{x+a\hat{\mu}} - \varphi_x}{a}, \tag{2.8}$$

where $\hat{\mu}$ is the unit vector in the μ-direction. Also the integration measure in the path integral simplifies and turns into a product measure over the fields at all lattice sites

$$\mathcal{D}[\varphi] \to \prod_x \mathrm{d}\varphi(x). \tag{2.9}$$

The lattice action now takes the form

$$S_{\text{Latt}} = a^d \sum_x \left(-\frac{1}{a^2} \sum_\mu \varphi(x)\varphi(x + a\hat{\mu}) + \frac{m_0^2 + 2d/a^2}{2} \varphi(x)^2 + \frac{g_0}{4!} \varphi(x)^4 \right). \tag{2.10}$$

Since a computer can only work with pure numbers we need to rewrite the action purely in terms dimensionless quantities. We will work with units where $c = \hbar = 1$, which means that the action itself is dimensionless. In fact everything can be expressed in terms of its mass dimension. Length has a mass dimension $[L] = -1$ so in order to cancel the a^d in the action it follows that

$$[\varphi] = \frac{d-2}{2}, \quad [g_0] = d - 4. \tag{2.11}$$

It is conventional to trade the bare parameters m_0 and g_0 for dimensionless parameters κ and λ via the relations

$$a^{\frac{d-2}{2}} \varphi(x) = \sqrt{2\kappa}\varphi_x, \quad (am_0)^2 = \frac{1 - 2\lambda}{\kappa} - 2d, \quad a^{d-4} g_0 = 6\lambda, \tag{2.12}$$

after which the lattice action can be written

$$S_{\text{Latt}} = \sum_x \left(-2\kappa \sum_\mu \varphi_x \varphi_{x+a\hat{\mu}} + \varphi_x^2 + \lambda(\varphi_x^2 - 1)^2 \right). \tag{2.13}$$

There is no longer any explicit dependence of the lattice spacing a. Instead, it is implicitly determined by the parameters κ and λ. In order to recover the continuum theory we need to take the continuum limit $a \to 0$ somehow. All observables of the lattice system will be measured in units of the lattice spacing, so for all practical purposes the lattice spacing can be taken to be $a = 1$. This may seem counter intuitive when we really want to let $a \to 0$, but imagine for example that we measure the lightest mass m of the excitation's of the φ field. However, what we really measure is am. Since the lightest mass is also the inverse correlation length $\xi = 1/m$ of the system we see that small values of the mass, measured in units of the lattice spacing, corresponds to large values of the correlation length, also in units of a. This is exactly what can be considered an approach to the continuum limit, since if the field is correlated over distances covering many lattice spacings, then it will be blind to the discrete nature of the underlying lattice. It is well known that the correlation length of a system diverges at a second-order phase transition, and the phase diagram of the real ϕ^4 model does feature a critical line of second-order phase transitions. So in order to take the continuum limit, we need to tune κ and λ to this line. As usual in physics only relative quantities, like mass ratios, can be measured on the lattice. In order to set an absolute scale some external input, typically from experiment, is needed. However, up to this ambiguity of scale, everything which comes out of the lattice simulation is in principle a prediction which can be tested against experiment.

It is not always the case that the model under investigation features a second order phase transition, this is for example true for many Yang-Mills theories. In those cases the continuum limit must be taken by other means, for example by exploiting asymptotic freedom, we will not expand upon this here.

As the continuum limit is taken we have to be aware of boundary effects, because as the correlation length grows larger the field will start to interact with its mirror images at the periodic extensions of the lattice. In order to prevent this, the thermodynamic limit $N \to \infty$ should be taken before the continuum limit. This is often impractical so usually the continuum limit is taken at fixed physical volume $L/\xi = \text{const}$,

where after an infinite volume extrapolation $L/\xi \to \infty$ can be attempted. Oftentimes, however, finite volume corrections are of the form $e^{-L/\xi}$ and are simply considered negligible if $L/\xi \gtrsim 5$.

2.1.1 *Lattice Simulations*

Now that the lattice discretization and its generalities have been explained we turn to the more practical issue of how to use it to measure observables. Even though the lattice discretization has made the number of degrees of freedom in the system finite, the path integral is still an integral of exceedingly high dimension. For such an integral, the only practical method of evaluation is to use Monte Carlo techniques, which sample the configuration space randomly. The price to pay for evaluating the integral with a random process is that there will always be a statistical uncertainty in the result. The advantage, however, is that under reasonable assumptions this uncertainty scales as the inverse square root of the number of samples, i.e. to reduce the statistical uncertainty by a factor N, the number of samples has to be increased by a factor of N^2, which means that it is possible to achieve arbitrary accuracy in polynomial time. Since the contribution of a field configuration to the partition function is proportional to the exponential of minus its action, only a fairly small subset of the huge configuration space actually contributes significantly to the partition function. It is therefore essential not to sample configuration space uniformly, but to propose configurations with probability exactly given by their contribution to the partition function. In this way, we can evaluate expectation values in the given model with maximal efficiency. The problem is that we do not know the underlying distribution, and even if we did, it is so high dimensional that we could not store it in our computer, so how can we sample configurations from it? The solution is called Markov Chain Monte Carlo (MCMC) which relies on a random process called a Markov Chain which will automatically generate samples from the target distribution, without actually having to store it. Many shelf-meters of excellent texts have been written on this matter, see for example [20, 29], so we will not go further into the details. Instead, let us give an example of a measurement. Given a model, for example the ϕ^4-theory in eq. (2.13), with action $S[\varphi]$, we want to evaluate the expectation value

of some observable $O[\varphi]$, for example the square of the field φ^2. The integral we would like to evaluate is

$$\langle O \rangle = \frac{\int \mathcal{D}[\varphi] O[\varphi] e^{-S[\varphi]}}{\int \mathcal{D}[\varphi] e^{-S[\varphi]}}. \tag{2.14}$$

This integral can be approximated by the sum over a finite number N_s of sample configurations $\{\varphi^{(i)}\}_{i=1}^{N_s}$. If the probability of drawing configuration $\varphi^{(i)}$ was p_i then the corresponding term in the sum should be weighted by $1/p_i$ and we obtain

$$\langle O \rangle \approx \frac{\sum_{i=1}^{N_s} O[\varphi^{(i)}] e^{-S[\varphi^{(i)}]} p_i^{-1}}{\sum_{i=1}^{N_s} e^{-S[\varphi^{(i)}]} p_i^{-1}}. \tag{2.15}$$

We see now that if $p_i = e^{-S[\varphi^{(i)}]}/Z$ as the Markov Chain will assure, then the expectation value will simply be

$$\langle O \rangle \approx \frac{1}{N_s} \sum_{i=1}^{N_s} O[\varphi^{(i)}], \tag{2.16}$$

with a statistical error

$$\delta \langle O \rangle \propto \sqrt{\frac{\mathrm{var}(O)}{N_s}}. \tag{2.17}$$

2.1.2 *The Sign Problem*

So far, we have assumed that the action is real and thus that the Boltzmann factor e^{-S} can be interpreted as a probability. However, this is not always the case, sometimes the action acquires a sign or a phase, the most extreme case being the initial real-time path integral, where the Boltzmann factor is a pure complex phase. Regardless of whether the phase occurs just for a few configurations or for all, the probability picture of the Boltzmann factor is spoiled. In principle, there is a work-around to this problem, which consists of moving the phase from the Boltzmann factor to the observable using the identity

$$\begin{aligned} \langle O \rangle &= \frac{\int \mathcal{D}[\varphi] O e^{-S}}{\int \mathcal{D}[\varphi] e^{-S}} = \frac{\int \mathcal{D}[\varphi] O[\varphi] e^{-i\mathrm{Im}[S]} e^{-\mathrm{Re}[S]}}{\int \mathcal{D}[\varphi] e^{-\mathrm{Re}[S]} \frac{\int \mathcal{D}[\varphi] e^{-i\mathrm{Im}[S]} e^{-\mathrm{Re}[S]}}{\int \mathcal{D}[\varphi] e^{-\mathrm{Re}[S]}}} \\ &= \frac{\left\langle O e^{-i\mathrm{Im}[S]} \right\rangle_{\mathrm{Re}[S]}}{\left\langle e^{-i\mathrm{Im}[S]} \right\rangle_{\mathrm{Re}[S]}}, \end{aligned} \tag{2.18}$$

where only the absolute value of e^{-S} is used to generate configurations. However, closer inspection of the expectation value in the denominator reveals that there is a problem. The partition function of the original model can be expressed in terms of the free-energy density f as $Z = e^{-Vf}$ where V is the physical volume of the system. The model where only the real part of the action is taken into account is also a valid model, called the phase quenched version of the original model. Its partition function can likewise be expressed in terms of its free-energy density f_{pq} as $Z_{\mathrm{pq}} = e^{-Vf_{\mathrm{pq}}}$. Since the two models are different, their free energies will differ by some finite amount δf and thus the ratio of their partition functions will be given by $Z/Z_{\mathrm{pq}} = e^{-V\delta f}$. But this ratio is nothing else that the expectation value of the phase

$$\left\langle e^{-i\mathrm{Im}[S]} \right\rangle_{\mathrm{Re}[S]} = \frac{\int \mathcal{D}[\varphi] e^{-S}}{\int \mathcal{D}[\varphi] e^{-\mathrm{Re}[S]}} = \frac{Z}{Z_{\mathrm{pq}}} = e^{-V\delta f}. \tag{2.19}$$

In order to accurately measure this expectation value, the statistical error must also be exponentially small in the volume, which would require an exponential number of measurements. This is what is meant by the sign problem. For some models with complex action it is possible to find a change of variables with only non-negative weights in the partition sum but there is no general solution to this problem and it can be shown that solving the sign problem is equivalent to solving an NP-hard problem [96].

After this very brief introduction to lattice QFT, let us turn to some alternatives to simulating the full d-dimensional model.

2.2 MEAN FIELD THEORY

Mean field (MF) theory is a very useful tool in almost any field of physics and its historical importance can hardly be exaggerated. As an approximation it is simple enough to be applicable and yield results in almost any situation and yet, in many cases, it captures the qualitatively important features of the model it is applied to. As such, MF theory serves either as a last resort when all else fails or as first probe to shine light on the general properties of a given model and to guide the choice of a more sophisticated and accurate technique to attack the problem with. There are of course many cases where MF theory is known to completely fail, but any approximation has its limits of validity. The MF-theory concept is also immense and it encompasses a multitude of

formulations and variations of the general idea. It is far beyond the scope of this thesis to in depth elucidate and rigorously formalize this large field. Let us instead focus on a practical approach to the matter and give examples of MF solutions to theories which will occur and be relevant in the main part of the thesis and that will bring us more directly to the various extensions to MF theory, in particular EMFT, that will be explained in more detail in section 2.4. For readers familiar with MF theory the rest of this section will contain nothing new and can thus be skipped.

As stated above there are many ways of deriving the MF equations of a given theory and even though the final equations may be the same, different methods have different merits since they may make various extensions and generalizations more or less accessible. The derivation given below may not be the most sophisticated but it is quite succinct and it will suffice for our purposes at the same time as being susceptible to straightforward generalizations to DMFT and EMFT. Let us for definiteness consider a real ϕ^4-theory on a d-dimensional lattice. The partition function is given by

$$Z = \int \mathcal{D}[\varphi] \prod_x \exp\left(-\varphi_x^2 - \lambda(\varphi_x^2 - 1)^2 + 2\kappa \sum_{\mu=1}^{d} \varphi_x \varphi_{x+\widehat{\mu}} \right). \tag{2.20}$$

In essence, we want to determine the mean field, i.e. vacuum expectation value, of the field $\varphi \in \mathbb{R}$ in this model. The MF approximation works by coupling a domain D of *live* sites, which are allowed to take values on all of $\mathbb{R}$, to an exterior bath D^c, the complement of D, where the fields are fixed to the sought mean value. The mean value is then tuned until the fields in D also on average take this value, in what is called a self-consistency equation. This method of deriving the self-consistency equation is sometimes called the cavity method, since the live domain can be thought of as a cavity within the external bath. The resulting MF action clearly neglects all interactions between the fluctuations in the fields but serves as a first approximation and can be shown to be exact in the limit where the coordination number of the lattice goes to infinity ($d \to \infty$). To derive the self-consistency equation we thus simply keep all integrals over the live fields in the partition function (2.21), set all other fields equal to a constant m and throw away

everything that does not explicitly depend on the value of a live field. We then end up with

$$Z_{\mathrm{MF}} = \int \prod_{i \in D} \mathrm{d}\varphi_i \, e^{S_{\mathrm{MF}}}, \tag{2.21}$$

$$S_{\mathrm{MF}} = \sum_{i \in D} \left\{ \varphi_i^2 + \lambda \left(\varphi_i^2 - 1 \right)^2 - 2\kappa z_i m \varphi_i - 2\kappa {\sum_{\langle i,j \rangle}}' \varphi_i \varphi_j \right\}, \tag{2.22}$$

where z_i are the number of nearest neighbors of $i \in D$ which lie in D^c and the sum ${\sum}'_{\langle i,j \rangle}$ denotes the sum over all nearest neighbors j of i which are also inside D. Now, it is a straightforward matter to determine, for example by fixed-point iteration, the self-consistent value of m such that $\langle \varphi \rangle_{Z_{\mathrm{MF}}} = m$. Let us consider the solution when the live domain D is a single site on a hyper-cubic lattice in d dimensions. The partition function then takes a particularly simple form

$$Z_{\mathrm{MF}} = \int_{-\infty}^{\infty} \mathrm{d}\varphi \, e^{-\varphi^2 - \lambda \left(\varphi^2 - 1 \right)^2 + 4d\kappa m \varphi}, \tag{2.23}$$

with the self-consistency equation

$$m = \frac{\int_{-\infty}^{\infty} \mathrm{d}\varphi \, \varphi e^{-\varphi^2 - \lambda \left(\varphi^2 - 1 \right)^2 + 4d\kappa m \varphi}}{\int_{-\infty}^{\infty} \mathrm{d}\varphi \, e^{-\varphi^2 - \lambda (\varphi^2 - 1)^2 + 4d\kappa m \varphi}}. \tag{2.24}$$

Close to the critical point we can expand in m and obtain a closed form for the critical coupling κ_c, and for the magnetization as a function of $\kappa - \kappa_c$. If we define

$$M_k = \frac{\int_{-\infty}^{\infty} \mathrm{d}\varphi \, \varphi^k e^{-\varphi^2 - \lambda \left(\varphi^2 - 1 \right)^2}}{\int_{-\infty}^{\infty} \mathrm{d}\varphi \, e^{-\varphi^2 - \lambda (\varphi^2 - 1)^2}} \tag{2.25}$$

the self-consistency equation becomes (up to order m^3)

$$4d\kappa M_2 m + \frac{(4d\kappa)^3}{6} m^3 \left(M_4 - 3M_2^2 \right) = m, \tag{2.26}$$

or equivalently, for $m \neq 0$,

$$\kappa = \frac{1}{4dM_2} \left(1 + \frac{1}{2M_2} \left(1 - \frac{M_4}{3M_2^2} \right) m^2 \right), \tag{2.27}$$

from which $\kappa_c = (4dM_2)^{-1}$ is immediately obtained. Since $M_4 \leq 3M_2^2$ for any $\lambda > 0$ we find that, for $\kappa - \kappa_c$ small and positive, the magnetization m behaves as

$$m = \sqrt{\frac{2M_2(\kappa - \kappa_c)}{1 - \frac{M_4}{3M_2^2}}}, \tag{2.28}$$

and thus the mean field value of the critical exponent $\beta = 1/2$. In the limit $\lambda \to \infty$ the Ising model is recovered from eq. (2.20) and $M_4 = M_2 = 1$, which leads to the familiar results $\kappa_c = (4d)^{-1}$ and $m = \sqrt{3(\kappa - \kappa_c)}$. For general λ the moments M_k can be expressed in terms of modified Bessel functions but their exact form is not very enlightening.

For other models an analogous derivation is typically possible and it is also possible to consider for example models where there are independent mean fields for φ and $\varphi^\dagger$, when $\varphi \in \mathbb{C}$. The dimension above which MF theory yields correct (mean-field) critical exponents is called the upper critical dimension d_{uc} and for the ϕ^4 model above it is $d_{\text{uc}} = 4$. In the limit of infinite number of dimensions d (or infinite coordination number z of the lattice), the sum over nearest neighbors becomes equal to the space average of the field,

$$\kappa\varphi_0 \frac{1}{z} \sum_{\langle 0,j \rangle} \varphi_j \underset{z\to\infty}{\to} \kappa\varphi_0 \frac{1}{V} \int \mathrm{d}x\, \varphi_x = \kappa\varphi_0 m. \tag{2.29}$$

Thus, using translation invariance, the field at each point in space couples only to itself locally and to the spatial average, and the partition function eq. (2.20) reduces exactly to the MF partition function eq. (2.23). Unless the translation invariance of the theory is spontaneously broken, the MF approximation thus becomes exact in the limit of infinite number of dimensions.

2.3 DYNAMICAL MEAN FIELD THEORY

In addition to simply enlarging the live domain D, there are many ways of generalize standard MF theory to include some of the fluctuations between the fields. One such generalization which has seen much success and many applications within the condensed matter community is Dynamical Mean Field Theory [53, 52]. Here, the word "dynamical"

refers to the fact that the mean field can fluctuate in one direction, typically the Euclidean time direction, because of the special role time plays in condensed matter physics, while remaining constant in the $(d-1)$ other dimensions. The d-dimensional lattice problem is thus mapped onto a 1-dimensional problem with non-local interactions representing the influence of the remaining degrees of freedom. Due to this dynamical dimension, DMFT gives access to correlation functions which are localized in the frozen directions. If the dynamical dimension is the imaginary-time axis, DMFT furthermore enables the calculation of finite-temperature expectation values. Obtaining access to this kind of information is an additional motivation to explore the DMFT approach.

In general, the effective 1-dimensional model must be solved numerically, for example using a (Quantum) Monte Carlo method [59]. As in MF theory, the DMFT calculation involves a self-consistent computation of the (dynamical) mean field, which in practice amounts to solving a set of non-linear equations self-consistently. The increased complexity arises from the fact that the field to be optimized is a function (or a collection of functions) of one variable.

DMFT was initially developed for fermionic systems, but the theory was later extended and successfully applied to bosonic lattice systems [33, 13, 14] and Bose-Fermi mixtures [15]. The bosonic version of DMFT can, with rather straightforward modifications, be applied to the φ^4 QFT. It is thus an interesting question how well this approach, which manifestly breaks Lorentz invariance, can capture the phase diagram and critical behavior of lattice QFTs. In non-relativistic condensed-matter systems it intuitively makes sense to treat space and time differently. In the spatial dimensions the system is typically a crystal with fixed lattice spacing(s) whereas time is a continuous variable. In other words, the correlation function certainly behaves differently in the spatial and in the temporal directions. For a relativistic QFT (at zero temperature) this is, however, not the case, so the singling out of one dimension is somewhat questionable: why should we neglect the effect of spatial correlations but take temporal ones into account when they are related by Lorentz transformations? A pragmatist's answer to this question could be "Let us just try it out, and see how well it works." Another way around this objection is to notice that a finite, periodic temporal direction corresponds to a finite temperature in the system. Thus the very breaking of Lorentz invariance can be an interesting and desired

feature. The Lorentz invariance of the observables is then recovered by extrapolating to zero temperature.

Also here it is beyond the scope of this thesis to give a full recapitulation of DMFT and its extensions since there already exists excellent review articles on the subject, see for example [53]. We will focus here on the applications of DMFT to QFTs, and in particular bosonic QFTs, like ϕ^4-theory. In a nutshell, DMFT is like single-site MF theory for a world line. Instead of just interacting with an external bath via en effective external field, the field at a given spatial site is now also allowed to interact with itself at a later time, via effective propagation in the external bath. In other words, the goal is to self-consistently map the full model to a 1-dimensional model with a non-local kernel $\Delta(t - t')$, which couples the field $\varphi(t)$ to the field $\varphi(t')$. In addition to the expectation value of the field φ, now also the kernel $\Delta(t)$ has to be self-consistently determined. The new observable in the 1-dimensional model, as opposed to the 0-dimensional one, is the time-dependent propagator along the world line $G_{\mathrm{wl}}(t)$ and its Fourier transform $\widetilde{G}_{\mathrm{wl}}(\omega)$. We want this to, as closely as possible, match the point-to-point correlator of the full model $G(\vec{0}, t)$. The approximate matching between the full and the effective models is done through the self-energy Σ. Quite generally we can express the Green's function of some interacting theory in momentum space as

$$\widetilde{G}(\boldsymbol{k}, \omega) = \frac{1}{\widetilde{G}_0^{-1}(\boldsymbol{k}, \omega) + \widetilde{\Sigma}(\boldsymbol{k}, \omega)}, \tag{2.30}$$

where $\widetilde{G}_0^{-1}(\boldsymbol{k}, \omega)$ is the Green's function of some reference theory which can be calculated analytically. In the case of ϕ^4-theory, this would be the free, $\lambda = 0$, theory. $\widetilde{\Sigma}$ is the self-energy which captures the interaction effects. The "local" Green's function, from $\vec{x} = \vec{0}$ to $\vec{x} = \vec{0}$, is obtained by summing over all spatial momenta,

$$\widetilde{G}_{\mathrm{loc}}(\vec{x} = \vec{0}, \omega) = \sum_{\boldsymbol{k}} \frac{1}{\widetilde{G}_0^{-1}(\boldsymbol{k}, \omega) + \widetilde{\Sigma}(\boldsymbol{k}, \omega)}, \tag{2.31}$$

where the momentum sum (or integral) is normalized such that $\sum_{\boldsymbol{k}} 1 = 1$. The Green's function of the world-line model also satisfies such a relation,

$$\widetilde{G}_{\mathrm{wl}}(\omega) = \frac{1}{\widetilde{G}_{\mathrm{wl},0}^{-1}(\omega) + \widetilde{\Sigma}_{\mathrm{wl}}(\omega)}, \tag{2.32}$$

where $\widetilde{G}_{\mathrm{wl},0}(\omega)$ is likewise the Green's function of some reference system which can be calculated analytically. DMFT approximates the

exact self-energy $\widetilde{\Sigma}$ with the self-energy $\widetilde{\Sigma}_{\mathrm{wl}}$ of the world-line model, i.e. $\widetilde{\Sigma}(\boldsymbol{k},\omega) \approx \widetilde{\Sigma}_{\mathrm{wl}}(\omega) = \widetilde{G}_{\mathrm{wl}}^{-1}(\omega) - \widetilde{G}_{\mathrm{wl},0}^{-1}(\omega)$, which can be substituted in eq. (2.31). The approximate local Green's function G_{loc} may then be expressed as

$$\widetilde{G}_{\mathrm{loc}}(\omega) = \sum_{\boldsymbol{k}} \frac{1}{\widetilde{G}_0^{-1}(\boldsymbol{k},\omega) + \widetilde{G}_{\mathrm{wl}}^{-1}(\omega) - \widetilde{G}_{\mathrm{wl},0}^{-1}(\omega)}. \tag{2.33}$$

The self-consistency condition identifies the local Green's function (2.31) with the world-line Green's function (2.32), which thus implicitly determines Δ (we shall shortly see how Δ enters the equation). The two coupled self-consistency functional equations then read

$$\widetilde{G}_{\mathrm{wl}}(\omega) = \widetilde{G}_{\mathrm{loc}}(\omega), \tag{2.34}$$

$$\langle \varphi \rangle_{S_{\mathrm{wl}}} = \phi_{\mathrm{ext}}. \tag{2.35}$$

To understand how the world-line model is constructed from the original model a concrete example is in order. We will consider the same model as in the previous section, namely real ϕ^4-theory on a d-dimensional, hyper-cubic lattice. For clarity, let us repeat the partition function here:

$$Z = \int \mathcal{D}[\varphi] \prod_x \exp\left(-\varphi_x^2 - \lambda(\varphi_x^2 - 1)^2 + 2\kappa \sum_{\mu=1}^{d} \varphi_x \varphi_{x+\hat{\mu}} \right). \tag{2.36}$$

The derivation proceeds much in the same way as that for standard MF theory. In fact, the self-consistency equation of the previous section can be obtained as an intermediate result of the following derivation. We assume that the global $\mathbb{Z}_2$ symmetry $\varphi(x) \to -\varphi(x)\ \forall x$ is spontaneously broken, since this is the more general case; the equations for the symmetric phase can be easily obtained by setting the expectation value of the field to zero. The expectation value of the field in the broken-symmetry phase will then be determined self-consistently as in standard MF theory.

We consider a lattice with $N_s^{d-1} N_t$ sites (N_s can formally be taken to be infinite) and denote by $\varphi_{\vec{i},t}$ the field on the site $(\vec{i},t) = (x_1,\ldots,x_{d-1},t)$. We then single out $\vec{i} = \vec{0} \equiv (0,\ldots,0)$ and call the world line at the spatial origin, $\varphi_{\mathrm{int},t} \equiv \varphi_{\vec{0},t}$, the *internal* degrees of freedom. All other sites are considered an external effective bath or *external* degrees of freedom, $\varphi_{\mathrm{ext},t} = \{\varphi_{\vec{j},t} : \vec{j} \neq \vec{0}\}$.

We can write the action, eq. (2.36), as a sum of three terms, the action of the world line S_{int}, the action of the external sites S_{ext} and the interaction of the world line with the external bath ΔS:

$$\begin{aligned} S &= \sum_x \left[-2\kappa \sum_\mu \varphi_{x+\hat{\nu}} \varphi_x + \varphi_x^2 + \lambda(\varphi_x^2 - 1)^2 \right] \\ &= S_{\text{int}} + \Delta S + S_{\text{ext}}, \end{aligned} \tag{2.37}$$

with

$$S_{\text{int}} = \sum_t \left[-2\kappa \varphi_{\text{int},t+1} \varphi_{\text{int},t} + \varphi_{\text{int},t}^2 + \lambda \left(\varphi_{\text{int},t}^2 - 1 \right)^2 \right], \tag{2.38}$$

$$\Delta S = -2\kappa \sum_t \sum_{\langle \text{int,ext} \rangle} \varphi_{\text{int},t} \varphi_{\text{ext},t}, \tag{2.39}$$

$$S_{\text{ext}} = \sum_{x \neq (\vec{0},t)} \left[-2\kappa \sum_{\substack{\mu \\ x+\hat{\mu} \neq (\vec{0},t)}} \varphi_{x+\hat{\mu}} \varphi_x + \varphi_x^2 + \lambda \left(\varphi_x^2 - 1 \right)^2 \right]. \tag{2.40}$$

The sum over $\langle \text{int}, \text{ext} \rangle$ is shorthand for the sum over all external sites ext at time t which are nearest neighbors to the internal site int at time t. A visual representation of this decomposition is given in fig. 2.2.

The surrounding bath is considered to be of infinite size and can thus spontaneously break the symmetry and develop an expectation value. The world-line subject to the action S_{int} can not spontaneously break the symmetry, since $d = 1$ is the lower critical dimension of the Ising universality class. At and below the lower critical dimension, the system is always disordered since the entropy gain of introducing a domain wall wins over the energy cost. In a 1-dimensional chain of Ising spins the energy cost of breaking one bond is constant but it does not cost any energy to move the broken bond along the chain. However, via the interaction with the external bath, which in part acts as an external field, the field in the world-line can also acquire an expectation value. In order to account for this possibility we write,

$$\varphi_{\text{ext},t} = \phi_{\text{ext}} + \delta\varphi_{\text{ext},t}, \qquad \langle \varphi_{\text{ext},t} \rangle = \phi_{\text{ext}}, \tag{2.41}$$

$$\varphi_{\text{int},t} = \phi_{\text{int}} + \delta\varphi_{\text{int},t}, \qquad \langle \varphi_{\text{int},t} \rangle = \phi_{\text{int}}. \tag{2.42}$$

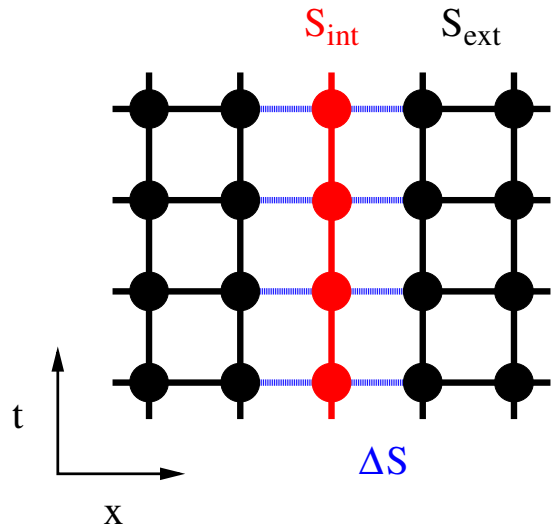

Figure 2.2: Graphical interpretation of the cavity method where the action (2.37) is decomposed into an internal part, S_{int}, an external part, S_{ext}, and an interaction part, ΔS. The external degrees of freedom are then integrated out after a Taylor-expansion of the interaction, $\exp(-\Delta S)$.

Note that the two expectation values are not dynamical variables but rather constants that can be tuned to achieve self-consistency. Inserting this in ΔS yields,

$$\Delta S = -2\kappa \sum_t \Bigg(2(d-1)\phi_{\text{ext}}\delta\varphi_{\text{int},t} + \delta\varphi_{\text{int},t} \sum_{\langle \text{int,ext} \rangle} \delta\varphi_{\text{ext},t} + 2(d-1)\phi_{\text{int}}\delta\varphi_{\text{ext},t} \Bigg). \quad (2.43)$$

There are three different terms which are dealt with differently. The first term can be included in S_{int}. We assume small fluctuations around the classical solution so the second term can be used to expand the Boltzmann weight. The third term is independent of the internal

degrees of freedom (ϕ_{int} is considered fixed) and is included in S_{ext}. Let us define

$$S_1 = -4\kappa(d-1)\sum_t \phi_{\text{ext}}\delta\varphi_{\text{int},t}, \tag{2.44}$$

$$\delta S = -2\kappa\sum_t \sum_{\langle \text{int,ext}\rangle} \delta\varphi_{\text{int},t}\delta\varphi_{\text{ext},t} \equiv \sum_t \delta S(t), \tag{2.45}$$

and expand $\exp(-\delta S)$ to get

$$\begin{aligned} Z &= Z_{\text{ext}} \int \mathcal{D}\varphi_{\text{int}} \exp(-S_{\text{int}} - S_1)\zeta, \\ \zeta &= 1 - \sum_t \langle \delta S(t)\rangle_{\text{ext}} + \frac{1}{2}\sum_{t,t'}\langle \delta S(t)\delta S(t')\rangle_{\text{ext}} + \dots, \end{aligned} \tag{2.46}$$

where $Z_{\text{ext}} \equiv \int \mathcal{D}[\varphi_{\text{ext}}]\exp(-S_{\text{ext}})$ is the partition function of the action including only $\varphi_{\text{ext},t}$. The expectation values are with respect to Z_{ext}. The first order term in ζ is proportional to the expectation value of $\delta\varphi_{\text{ext}}$ which is zero by construction. The second-order term is non-zero and we find,

$$\begin{aligned} \langle \delta S(t)\delta S(t')\rangle_{\text{ext}} &= 4\kappa^2\delta\varphi_{\text{int},t}\left[\sum_{\langle \text{int,ext}\rangle}{\sum_{\langle \text{int,ext}\rangle}}' \langle \delta\varphi_{\text{ext},t}\delta\varphi_{\text{ext},t'}\rangle_{\text{ext}}\right]\delta\varphi_{\text{int},t'} \\ &\equiv 2\delta\varphi_{\text{int},t}\Delta(t-t')\delta\varphi_{\text{int},t'}, \end{aligned} \tag{2.47}$$

where the prime on the second sum means that there are two different external sites. This corresponds to a field propagating in the effective medium subjected to the unknown propagator, between creation and annihilation at the spatial origin. This term is called "hybridization function" $\Delta(t-t')$. It originates from connected diagrams and will be determined self-consistently by demanding that the local Green's function of the effective model coincide with the local Green's function of the full model, as explained above. $\Delta(t)$ is a real-valued function but in more general cases where the field φ may have multiple components, it will be matrix-valued. Here we can see that DMFT is a better approximation at high dimensionality. We have already argued that MF theory should be exact in $d = \infty$ and in MF theory quadratic fluctuations are completely ignored. That means that expectation values like $\langle \delta\varphi_{\text{ext},t}\delta\varphi_{\text{ext},t'}\rangle_{\text{ext}}$ factorize and thus we recover eq. (2.24) if we ignore

the contribution of δS. After the re-exponentiation eq. (2.46) we find the world-line action,

$$\begin{aligned} S_{\text{wl}} &= \sum_t \left[-2\kappa\varphi_{t+1}\varphi_t + \varphi_t^2 + \lambda(\varphi_t^2 - 1)^2 - 4\kappa(d-1)\phi\varphi_t \right] \\ &\quad - \sum_{t,t'} \delta\varphi_t \Delta(t-t')\delta\varphi_{t'} \\ &= \sum_t \left[-2\kappa\varphi_{t+1}\varphi_t + \varphi_t^2 + \lambda(\varphi_t^2 - 1)^2 - 2\phi(2\kappa(d-1) - \widetilde{\Delta}(0)\varphi_t \right] \\ &\quad - \sum_{t,t'} \varphi_t \Delta(t-t')\varphi_{t'} \\ &= \sum_{t,t'} \varphi_t G^{-1}_{\text{wl},0}(t-t')\varphi_{t'} + \lambda \sum_t (\varphi_t^2 - 1)^2 - h \sum_t \varphi_t, \end{aligned} \tag{2.48}$$

where $\widetilde{G}^{-1}_{\text{wl},0}(\omega) = 1 - 2\kappa\cos(\omega) - \widetilde{\Delta}(\omega)$ is the inverse of the connected two-point Green's function of the free theory and $h = 2\phi\left(2\kappa(d-1) - \widetilde{\Delta}(0)\right)$ plays the role of an external magnetic field. The DMFT procedure is illustrated as a flowchart with an iterative loop in fig. 2.3.

Because of the non-local coupling Δ, this 1-dimensional system will typically have to be solved using Monte Carlo methods, but since the dimensionality has been reduced from four to one, a considerable speed-up can be achieved compared to solving the original model. The result is of course an approximation but for some models the approximation is very good and a significant improvement over standard MF [10].

2.4 EXTENDED MEAN FIELD THEORY

It was noted in [10] that the self-consistent self-energy, especially in high dimensions ($d \gtrsim 4$), only weakly depend on momentum and is well described by a constant in Fourier space, and thus a contact term in real space, see fig. 2.4. This leads us to consider a further simplification of DMFT, where only the contact term in Δ is retained. Since the effective action is now 0-dimensional, like in standard MF, but there is an extra external field related to the point-to-point correlator, this local-time limit of DMFT has been dubbed Extended Mean Field Theory (EMFT). This approximation was, with a slightly different motivation, first introduced by Pankov [80]. EMFT, being 0-dimensional, treats all space-time directions on equal footing, although the lattice still breaks the full Lorentz symmetry down to the hyper-cubic symmetry. The temperature can however still be controlled and can be either zero or nonzero. In

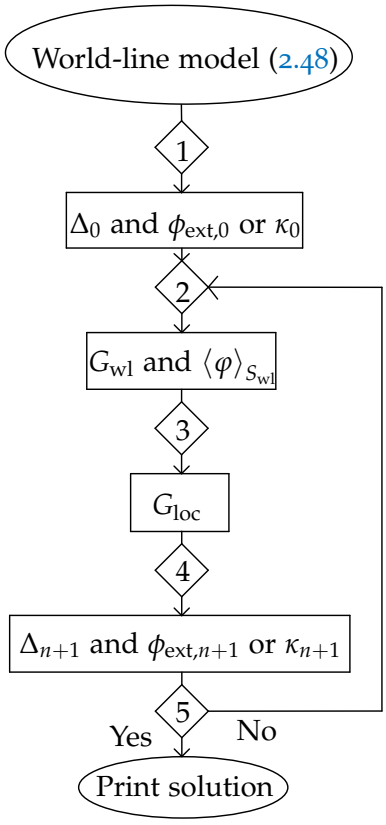

1 Starting guess

2 World-line solver

3 Dyson equation (2.33)

4 Self-consistency equations (2.34) and (2.35)

5 Convergence?

Figure 2.3: Schematic depiction of the DMFT procedure. For a given quartic coupling λ and either κ or ϕ_{ext} fixed we make a guess for Δ and the non-fixed variable. This defines an impurity action via eq. (2.48). We then solve this effective model for the Green's function and the expectation value of the field, $\langle\varphi\rangle$. The local Green's function of the full model is approximated via eq. (2.33). The self-consistency equations (2.34) and (2.35) are then used to calculate new values for Δ and ϕ_{ext} or κ. This procedure is iterated until the self-consistency equations are satisfied.

short EMFT offers a minimal extension of standard MF theory which also incorporates a mass renormalization, which is an essential component in order to accurately approximate observables, especially in models with Gaussian fixed points.

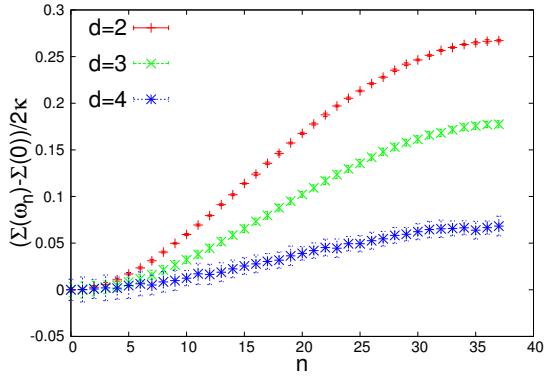

Figure 2.4: The frequency-dependent part of the self-energy, normalized to that of the inverse free propagator (i.e. divided by 2κ)), for $\lambda = 1$ ($d = 2, 3$) and $\lambda = 2$ ($d = 4$). The self-energy is only weakly frequency-dependent, especially for larger dimension, and can be further approximated by a constant, in the EMFT approximation.

Although the EMFT action can be obtained from the world-line action (2.48) by just dropping the non-local terms, let us repeat the derivation in a more general situation. Let $\vec{\varphi}$ be a field with real-valued components and action

$$S = -2\kappa \sum_{\langle i,j \rangle} \vec{\varphi}_i^{\mathsf{T}} A \vec{\varphi}_j + \sum_i V\left(\vec{\varphi}_i\right), \tag{2.49}$$

where A is an invertible, Hermitian matrix and $V(\vec{\varphi})$ is some general potential which goes to infinity as $|\vec{\varphi}| \to \pm\infty$. Expanding the field around its expectation value $\vec{\varphi} = \vec{\phi}_{\text{ext}} + \delta\vec{\varphi}$, the part of the action which depends on the field at the origin is

$$S_0 = -2\kappa z \vec{\varphi}_0^{\mathsf{T}} A \vec{\phi}_{\text{ext}} - 2\kappa \sum_{\langle 0,j \rangle} \delta\vec{\varphi}_0^{\mathsf{T}} A \delta\vec{\varphi}_i + V\left(\vec{\varphi}_0\right), \tag{2.50}$$

where z is the number of nearest neighbors on the lattice. We now formally integrate over all fields except at the origin and truncate the

induced couplings at second order, just as in DMFT. This is equivalent to the substitution

$$2\kappa \sum_{\langle 0,j\rangle} \delta\vec{\varphi}_0^{\intercal} A \delta\vec{\varphi}_i \to \delta\vec{\varphi}_0^{\intercal} \Delta \delta\vec{\varphi}_0, \tag{2.51}$$

where Δ is a symmetric matrix of a priori unknown couplings, which play the role of a shift in the mass matrix. This interpretation of Δ will be even clearer when we give a concrete example of how it enters in the self-consistency equations. To finish the derivation of the effective action we re-express it in terms of the non-shifted field to obtain

$$S_{\text{EMFT}} = -\vec{\varphi}_0^{\intercal}\Delta\vec{\varphi}_0 + \vec{\varphi}_0^{\intercal}\left(2\kappa z A - 2\Delta\right)\vec{\phi}_{\text{ext}} + V\left(\vec{\varphi}_0\right). \tag{2.52}$$

To fully appreciate the full self-consistent model, let us go back to the case of real ϕ^4 theory in d dimensions. In this case the EMFT action is given by

$$S_{\text{EMFT}} = (1-\Delta)\varphi^2 + \lambda\left(\varphi^2 - 1\right)^2 - 2\varphi\phi_{\text{ext}}(2\kappa d - \Delta), \tag{2.53}$$

where the external fields ϕ_{ext} and Δ are to be determined self-consistently. The self-energy of the EMFT action is given by

$$\Sigma_{\text{EMFT}} = \left(2\left(\langle\varphi^2\rangle - \langle\varphi\rangle^2\right)\right)^{-1} + 1 - \Delta. \tag{2.54}$$

The free Green's function in the full theory is given by $G_0^{-1}(k) = 1 - 2\kappa\sum_{\mu=1}^{d}\cos k_\mu$ and according to eqs. (2.33) to (2.35) the self-consistency equations becomes

$$2\left(\langle\varphi^2\rangle - \langle\varphi\rangle^2\right) = \sum_k \frac{1}{\left(2\left(\langle\varphi^2\rangle - \langle\varphi\rangle^2\right)\right)^{-1} + \Delta - 2\kappa\sum_{\mu=1}^{d}\cos k_\mu}, \tag{2.55}$$

$$\langle\varphi\rangle = \phi_{\text{ext}}. \tag{2.56}$$

It is now evident that the mass in the propagator is given by

$$M = \frac{1}{\kappa}\left(\left(2\left(\langle\varphi^2\rangle - \langle\varphi\rangle^2\right)\right)^{-1} + \Delta - 2\kappa\right), \tag{2.57}$$

which constitutes a very attractive feature of EMFT. Even though the effective action is 0-dimensional, we still have access to the ground-state

mass, through the self-consistency equation of the variance of the field. In the following chapters this will be used to draw conclusions about the models studied there.

A few comments about the momentum sum in the self-consistency eq. (2.55) are also in order. A priori, we are considering a model on a d-dimensional lattice of size $N_1 \times \cdots \times N_d$, i.e. the sum over (bosonic) momentum modes on the lattice is given by

$$\sum_k = \prod_{i=1}^{d} \frac{1}{N_i} \sum_{n_i=0}^{N_i-1}, \quad k_i = \frac{2\pi n_i}{N_i}. \tag{2.58}$$

The self-consistent solution thus depends on the lattice extent in the different directions, which allows us, for example, to consider finite temperature by making the extent of one of the directions smaller than the others. In general there is no advantage to keep the spatial dimensions finite since this would just induce finite size effects which are generally undesirable. If we identify the last dimension with the temporal one, the momentum sum thus usually takes one of the following forms

$$\sum_k = \int_{-\pi}^{\pi} \frac{\mathrm{d}^{d-1}k}{(2\pi)^{d-1}} \times \begin{cases} \frac{1}{N_t} \sum_{n_t=0}^{N_t-1} & T > 0 \\ \int_{-\pi}^{\pi} \frac{\mathrm{d}k}{(2\pi)} & T = 0 \end{cases}. \tag{2.59}$$

For the simple dispersion relation of a Gaussian free model we can in addition factorize the summand in the momentum sum by the introduction of an auxiliary variable

$$\frac{1}{\kappa M + 2\kappa \sum_{\mu=1}^{d} \left(1 - \cos k_\mu\right)} = \int_0^\infty \mathrm{d}\tau \, e^{-\kappa M \tau} \prod_{\mu=1}^{d} e^{2\kappa\tau(\cos k_\mu - 1)}. \tag{2.60}$$

The momentum integrals in all dimensions of infinite extent can now be performed using

$$\int_{-\pi}^{\pi} \frac{\mathrm{d}k}{(2\pi)} e^{2\kappa\tau(\cos k_\mu - 1)} = e^{-2\kappa\tau} I_0(2\kappa\tau) \equiv \hat{I}_0(2\kappa\tau), \tag{2.61}$$

where $I_0(x)$ is a modified cylindrical Bessel function and $\hat{I}_0(x) \sim \frac{1}{\sqrt{2\pi x}}$ for $x \gg 1$. For zero temperature, the local Green's function thus takes the form

$$G_{\mathrm{loc}}(M) = \frac{1}{\kappa} \int_0^\infty \mathrm{d}\tau \, e^{-M\tau} \left(\hat{I}_0(2\tau)\right)^d, \tag{2.62}$$

where it is clearly visible how the mass M guarantees an exponential suppression of the integrand, although for $d > 2$, the integral will converge also for $M = 0$. Expressing the momentum sum as a 1-dimensional integral, instead of a d-dimensional one, makes the method extremely computationally efficient.

In this simplified form some semi-analytic analysis of the self-consistent system becomes possible. Especially the critical coupling κ_c can be determined exactly. Since the dimension d now enters only in the exponent of a Bessel function, it is possible to extend the self-consistency equations from integer to real-valued dimensionality. Close to the phase transition, where ϕ_{ext} is very small, we can expand the exponential of the action in powers of ϕ_{ext}. It is convenient to define,

$$Z_0 \equiv \int \mathrm{d}\varphi \exp\left(-S_{\text{EMFT}}|_{\phi_{\text{ext}}=0}\right), \tag{2.63}$$

$$M_k \equiv \left\langle \varphi^k \right\rangle_{Z_0}. \tag{2.64}$$

In Z_0 we only discard the explicit dependence on ϕ_{ext} but not the implicit dependence in Δ, which will be determined below. In this setup M_k actually depends on ϕ_{ext}. A naive expansion to order $\mathcal{O}\left(\phi_{\text{ext}}^4\right)$ gives:

$$\begin{aligned}\langle\varphi\rangle &= 2(2d\kappa - \Delta)\phi_{\text{ext}} M_2 \\ &\quad + \frac{8}{6}(2d\kappa - \Delta)^3 \phi_{\text{ext}}^3 \left(M_4 - 3M_2^2\right), \end{aligned} \tag{2.65}$$

$$G_{\text{EMFT}} = 2\left(M_2 + 2\phi_{\text{ext}}^2 (2d\kappa - \Delta)^2 \left(M_4 - 3M_2^2\right)\right). \tag{2.66}$$

Using the self-consistency condition $\langle\varphi\rangle = \phi_{\text{ext}}$ we can determine Δ up to order ϕ_{ext}^2,

$$\Delta = 2d\kappa - \frac{1}{2M_2} + \frac{\phi_{\text{ext}}^2}{12M_2^2}\left(\frac{M_4}{M_2^2} - 3\right), \tag{2.67}$$

which leads to an effective action in terms of $\kappa, \phi_{\text{ext}}$ and M_2, M_4, which needs to be determined self-consistently. More precisely,

$$S_{\text{EMFT}} = \left(1 - 2d\kappa + \frac{1}{2M_2} - \frac{\phi_{\text{ext}}^2}{12M_2^2}\left(\frac{M_4}{M_2^2} - 3\right)\right)\varphi^2 + \lambda\left(\varphi^2 - 1\right)^2, \tag{2.68}$$

$$G_{\text{loc}} = \frac{1}{\kappa}\int_0^\infty \mathrm{d}\tau \exp\left[-\tau\frac{\phi_{\text{ext}}^2}{2\kappa M_2^2}\left(1 - \frac{M_4}{3M_2^2}\right)\right]\hat{I}_0(2\tau)^d, \tag{2.69}$$

$$G_{\text{EMFT}} = 2M_2 - 3\phi_{\text{ext}}^2\left(1 - \frac{M_4}{3M_2^2}\right), \tag{2.70}$$

which defines our self-consistency equations. M_4 already multiplies ϕ_{ext}^2, so, to order ϕ_{ext}^2, we can use its value at $\phi_{\text{ext}} = 0$, i.e. $M_4 \equiv M_4|_{\phi_{\text{ext}}=0}$. However, the ϕ_{ext}^2 correction to M_2 contributes and must be calculated. We find,

$$M_2 = M_2|_{\phi_{\text{ext}}=0} - \frac{\phi_{\text{ext}}^2}{6}\left(\frac{M_4}{(M_2|_{\phi_{\text{ext}}=0})^2} - 1\right), \tag{2.71}$$

which gives the Green's function,

$$G_{\text{EMFT}} = 2M_2|_{\phi_{\text{ext}}=0} - \frac{2\phi_{\text{ext}}^2}{3}\left(4 - \frac{M_4}{(M_2|_{\phi_{\text{ext}}=0})^2}\right). \tag{2.72}$$

$M_2|_{\phi_{\text{ext}}=0}$ must be determined self-consistently using the action in eq. (2.68). Equating G_{EMFT} and G_{loc} at $\phi_{\text{ext}} = 0$ yields,

$$2M_2|_{\phi_{\text{ext}}=0} = \frac{1}{2\kappa}\int_0^\infty \mathrm{d}\tau \hat{I}_0(\tau)^d, \tag{2.73}$$

which defines the critical coupling. Just as in the MF case, $M_2|_{\phi_{\text{ext}}=0}$ has an expression in terms of modified Bessel functions but eq. (2.73) still needs to be solved numerically. In the Ising limit the situation simplifies since $M_4 = M_2 = 1$ and using $\lim_{d\to\infty} d\int_0^\infty \mathrm{d}\tau\, \hat{I}_0(\tau)^d = 1$ we recover the MF result.

It was found in [10] and commented upon in [80] that EMFT sometimes wrongly predicts the phase transition to be first order, when it is in fact second order. This is related to how the κ which equates G_{EMFT} and G_{loc} behaves as a function of ϕ_{ext}. The analysis with arbitrary λ is quite involved but we can learn a lot by considering the Ising limit where $\lambda = \infty$. We have to distinguish between two cases: when $d > 4$ the integral

$$\int_0^\infty \mathrm{d}\tau\ \tau e^{-\tau d} I_0(\tau)^d \equiv I'_d \tag{2.74}$$

is finite and we can expand the exponential in eq. (2.69). After some algebra we find,

$$\kappa = \frac{I_d}{4} + \left(\frac{I_d}{4} - \frac{I'_d}{6I_d}\right)\phi_{\text{ext}}^2, \tag{2.75}$$

$$I_d = \int_0^\infty \mathrm{d}\tau\; e^{-\tau d} I_0(\tau)^d. \tag{2.76}$$

If the coefficient in front of ϕ_{ext}^2 is negative we have a first order transition because we will have a region with multiple solutions and this indeed happens for $d < 4.90249$. For larger d the coefficient is positive and we find a second order transition with critical exponent $\beta = 1/2$.

For $d = 2$ $G_{\text{loc}}(M)$ diverges logarithmically as $M \to 0$, so we cannot expect that EMFT will be accurate close to the transition. For $2 < d < 4$ $G_{\text{loc}}(0)$ is defined but it is easy to verify through the asymptotic form of the integrand $e^{-M\tau}(4\pi\tau)^{d/2}$ that $G_{\text{loc}}(M) = G_{\text{loc}}(0) - AM^{\frac{d-2}{2}} + \mathcal{O}(M)$, with $A > 0$ for $M \ll 1$. Since $M \propto \phi_{\text{ext}}^2$, this means that for small enough ϕ_{ext} the self-consistency equation takes the form,

$$\frac{I_d}{2\kappa} - \frac{B}{\kappa_c^2}\phi_{\text{ext}}^{d-2} = 2, \tag{2.77}$$

for $B > 0$, which gives,

$$\kappa = \frac{I_d}{4} - 32\frac{B}{I_d^3}\phi_{\text{ext}}^{d-2}. \tag{2.78}$$

Again, due to the negative prefactor, the transition is first order. The analysis for finite quartic couplings can be done numerically and in fig. 2.5 we show the value of λ for which the transition turns second order as a function of the dimension.

2.4.1 *k-integrated Green's functions*

Our goal is to efficiently calculate the local Green's function from the Green's function in momentum space. This is equivalent to integrating it over all momenta,

$$G_{xx} = \int \frac{\mathrm{d}^d k}{(2\pi)^d}\, \widetilde{G}(k). \tag{2.79}$$

The main complication is that we only know $\widetilde{G}^{-1}(k)$ explicitly. Let us consider the general case where we have N real or $N/2$ complex fields.

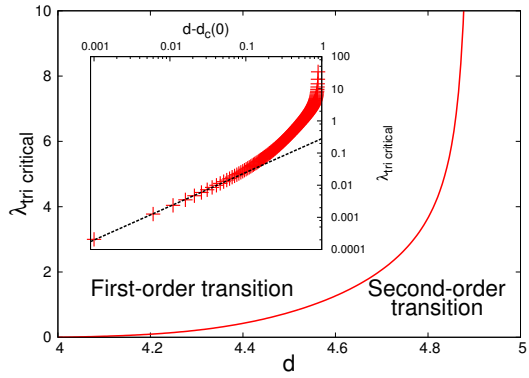

Figure 2.5: The tricritical quartic coupling for EMFT as a function of dimension. The critical dimension at $\lambda = 0$ is $d_c(0) \approx 4.00$. The inset shows a power law behavior as d approaches $d_c(0)$.

In this case the free Green's functions form a diagonal $N \times N$ matrix and the EMFT Green's functions form a full matrix,

$$\begin{aligned}\widetilde{G}(k) &= \left[G^{-1}_{\mathrm{EMFT}} + \Delta - 2\sum_{\nu=1}^{d} \cos(k_\nu - i\mu\delta_{\nu,t})\mathrm{Id}_d \right]^{-1} \\ &\equiv \left[A - \epsilon(k,\mu)\mathrm{Id}_d \right]^{-1},\end{aligned} \tag{2.80}$$

with the kinetic part

$$\epsilon(k,\mu) = 2\sum_{\nu=1}^{d} \cos(k_\nu - i\mu\delta_{\nu,t}). \tag{2.81}$$

The self-energy matrix A can be found by inverting the measured G_{EMFT}. Now, when $N = 1$, we can rewrite this in a form which allows for an analytic integration of the d components of k,

$$\frac{1}{a - \epsilon(k,\mu)} = \int_0^\infty \mathrm{d}\tau\, e^{-a\tau} \prod_{\nu=1}^{d} e^{2\tau\cos(k_\nu - i\mu\delta_{\nu,t})}. \tag{2.82}$$

We can integrate over k by using an integral representation of the modified Bessel function of first order, $I_0(x)$,

$$I_0(x) = \int_{-\pi}^{\pi} \frac{\mathrm{d}k}{2\pi}\, e^{x\cos(k+z)}. \tag{2.83}$$

Note that the (complex) constant z is irrelevant. The final result reads

$$\int \frac{\mathrm{d}^d k}{(2\pi)^d} \frac{1}{a - \epsilon(k,\mu)} = \int_0^\infty \mathrm{d}\tau \, e^{-a\tau} I_0^d(2\tau). \tag{2.84}$$

To study finite volume (temperature) we simply replace the relevant Bessel functions with what is obtained when the integral in eq. (2.83) is replaced by a discrete sum.

We will now show that $\widetilde{G}(k)$ can be written as a sum of such integrable terms for any value of N. Since $\widetilde{G}^{-1}(k)$ is symmetric and the k dependence is only on the diagonal, $\widetilde{G}^{-1}$ is diagonalized by a k-independent orthogonal matrix U which also diagonalizes $\widetilde{G}(k)$. The eigenvalues which make up the diagonal $\widetilde{D}(k) = U^\intercal \widetilde{G}(k) U$ are given by $(\lambda_i - \epsilon(k,\mu))^{-1}$ where $\{\lambda_i\}_{i=1}^N$ are the N eigenvalues of A. Using the k-independence of U we just have to integrate the elements of $\widetilde{D}(k)$, which are all integrals of the form of eq. (2.84). The matrix elements of $G(0)$ are then trivially recovered by applying U. Explicitly they are given by

$$(G_{xx})_{ij} = \sum_{k=1}^N U_{ik} U_{jk} \int_0^\infty \mathrm{d}\tau \, e^{-\lambda_k \tau} I_0^d(2\tau). \tag{2.85}$$

So, instead of performing one complicated d-dimensional integral for each matrix element, we can diagonalize the matrix and compute N 1-dimensional integrals.

3

EXTENDED MEAN FIELD STUDY OF COMPLEX ϕ^4-THEORY AT FINITE DENSITY AND TEMPERATURE

3.1 INTRODUCTION

In this chapter we review the derivation of the EMFT equations and apply them to complex scalar φ^4 theory with a nonzero chemical potential, one of the simplest models with a sign problem which comes from complex terms in the action. The chemical potential couples to a conserved charge, which is a consequence of Noether's theorem and of the global $U(1)$ symmetry. The model describes a relativistic Bose gas and its properties are well studied. It is possible to map the model to a so called world-line model [50], which is sign problem free and thus susceptible to unbiased Monte Carlo simulations. We will take advantage of this to evaluate the quality of the EMFT approximation. The main focus of the study will be to determine the phase diagram in the (μ, T)-plane.

The content of this chapter has been published in

- Oscar Akerlund et al. „Extended Mean Field study of complex ϕ^4-theory at finite density and temperature." In: *Phys. Rev. D* 90 (6 Sept. 2014), p. 065008. arXiv: 1405.6613 [hep-lat]. URL: http://link.aps.org/doi/10.1103/PhysRevD.90.065008.

3.2 COMPLEX φ^4 THEORY

φ^4 theories are important quantum field theories in many respects. As explained in chapter 2, even the simplest incarnation, with a single real scalar field, exhibits interesting phenomena like spontaneous symmetry breaking with a second-order phase transition. The $U(1)$ symmetric complex φ^4 theory with nonzero chemical potential is one of the simplest models which has a sign problem. One important application of the latter is in the Standard Model Higgs sector, which consists of

a two-component complex φ^4 theory, which will be investigated in greater detail in chapter 5.

In dimension higher than two, complex φ^4 exhibits a second-order phase transition as a function of the chemical potential μ. At low μ the system is a dilute Bose gas which Bose condenses above a critical chemical potential μ_c. We are mainly interested in the 4-dimensional case but for the sake of generality we will work in d dimensions and specify d only when necessary. The Lagrangian density of complex scalar φ^4 theory at finite chemical potential reads

$$\mathcal{L}[\varphi(x)] = \partial_\nu \varphi^*(x)\partial^\nu \varphi(x) - \left(m_0^2 - \mu^2\right)|\varphi(x)|^2 - \lambda|\varphi(x)|^4 + i\mu j_0(x), \tag{3.1}$$

$$j_\nu(x) = \varphi^*(x)\partial_\nu\varphi(x) - \partial_\nu\varphi^*(x)\varphi(x), \tag{3.2}$$

using a d-dimensional Minkowski metric, $(+,-,\ldots,-)$. $\left(m_0^2 - \mu^2\right)$ is a physically irrelevant shift of the bare mass, which is convenient when putting the theory on the lattice, where the μ^2 will drop out. j_ν is the conserved current due to the global continuous $U(1)$ symmetry, $\varphi(x) \leftrightarrow e^{i\theta}\varphi(x)\ \forall x$, with the conserved charge

$$Q = i\int \mathrm{d}^{d-1}x\ j_0(x). \tag{3.3}$$

The charge represents the number of particles minus the number of antiparticles, and a positive μ thus favors the creation of particles over antiparticles and renders the Lagrangian density (and action) complex.

After Wick rotating time to the imaginary axis to obtain a Euclidean metric, we discretize the action and put it on a regular d-dimensional hypercubic lattice with lattice spacing a. The chemical potential is associated with the (imaginary) time direction which will be referred to as t. All parameters are understood to be in terms of the lattice spacing, so we refrain from explicitly writing for example $a\mu$ instead of μ without causing confusion. With $\eta \equiv m_0^2 + 2d$ we arrive at the lattice action [1]

$$S = \sum_x \left(\eta|\varphi_x|^2 + \lambda|\varphi_x|^4 \quad - \sum_{\nu=1}^{d}\left[e^{-\mu\delta_{\nu,t}}\varphi_x^*\varphi_{x+\hat{\nu}} + e^{\mu\delta_{\nu,t}}\varphi_x^*\varphi_{x-\hat{\nu}}\right]\right). \tag{3.4}$$

1 In this chapter we will use a different notation from the one used in chapter 2 and chapter 5 to facilitate the direct comparison with pre-existing Monte Carlo simulations. It is a trivial matter to pass from one parametrization to another.

Because of different couplings in the forward and backward time direction the action is complex when $\mu \neq 0$. This prevents the usual probabilistic interpretation of the partition function and Monte Carlo methods cannot be blindly applied. The sign problem can be circumvented by a change of variables which allows to express the action in terms of world lines. The partition function can then be sampled using a worm algorithm, see e.g. [45, 50]. Another alternative is to use a complex Langevin method [1, 2]. We will approximate the model using EMFT and show that it also avoids the sign problem.

3.3 MEAN FIELD THEORY

The upper critical dimension of the complex φ^4 theory is $d_{\text{uc}} = 4$, so we expect that the MF solution will show a qualitatively correct behavior and provide a first approximation to quantitative results. Taking the action in eq. (3.4) and setting the field to its expectation value ("Weiss field"), $\varphi_x = \langle\varphi\rangle$, for all $x \neq 0$, gives us the single-site MF action

$$S_{\text{MF}} = \eta|\varphi_0|^2 + \lambda|\varphi_0|^4 - 4\langle\varphi\rangle \operatorname{Re}[\varphi_0](d - 1 + \cosh(\mu)). \tag{3.5}$$

We have used the $U(1)$ symmetry to rotate the expectation value to the real axis. The magnitude of the expectation value, $\langle\varphi\rangle$, is determined self-consistently by requiring

$$\langle\varphi_0\rangle_{S_{\text{MF}}} = \langle\varphi\rangle\,. \tag{3.6}$$

It is easy to check that there is a second-order phase transition at a critical chemical potential μ_c, whose exact value depends on d, η and λ. By expanding $\exp(-S_{\text{MF}})$ in powers of $\langle\varphi\rangle$, demanding self-consistency for $\langle\varphi\rangle$ and letting it go to zero, we find the critical chemical potential:

$$\cosh\mu_c(\eta,\lambda) = \frac{\sqrt{\lambda}}{2\frac{\exp(-K^2)}{\sqrt{\pi}\operatorname{Erfc}(K)} - 2K} + (1-d), \tag{3.7}$$

with $K = \frac{\eta}{2\sqrt{\lambda}}$. We can determine the continuum limit in the MF approximation by searching the critical value of η for which μ_c vanishes. For $d = 4$ and $\lambda = 1$ we find $\eta_c = 7.51366$.

3.4 EXTENDED MEAN FIELD THEORY

3.4.1 *Formalism*

As explained in chapter 2, EMFT improves upon MF theory by taking also quadratic fluctuations into account. Although a general derivation of the self-consistency equations was given in section 2.4, let us give a detailed account of the specific case at hand, because of the non-isotropic hopping term. For convenience we will use a slightly unconventional notation intended to make the derivation more transparent. The action, eq. (3.4), in this notation reads

$$S = \sum_x \left[-\sum_\nu \mathbf{\Phi}^\dagger_{x+\hat{\nu}} \boldsymbol{E}(\mu\delta_{\nu,t}) \mathbf{\Phi}_x + \frac{\eta}{2}|\mathbf{\Phi}_x|^2 + \frac{\lambda}{4}|\mathbf{\Phi}_x|^4 \right], \tag{3.8}$$

with

$$\mathbf{\Phi}^\dagger = (\varphi^*, \varphi), \quad \boldsymbol{E}(x) = \begin{pmatrix} e^{-x} & 0 \\ 0 & e^{x} \end{pmatrix}. \tag{3.9}$$

In the free case ($\lambda = 0$) the action is quadratic in $\mathbf{\Phi}$ and the inverse of the connected Green's function in Fourier space can be expressed as a matrix,

$$\begin{aligned} \widetilde{\boldsymbol{G}}_0^{-1}(k) &= \left\langle \mathbf{\Phi}\mathbf{\Phi}^\dagger \right\rangle_c = \left\langle \mathbf{\Phi}\mathbf{\Phi}^\dagger \right\rangle - \langle \mathbf{\Phi} \rangle \langle \mathbf{\Phi} \rangle^\dagger \\ &= \begin{pmatrix} \eta - 2\sum_{\nu=1}^{d} \cos\left(k_\nu - i\mu\delta_{\nu,t}\right) & 0 \\ 0 & \eta - 2\sum_{\nu=1}^{d} \cos\left(k_\nu + i\mu\delta_{\nu,t}\right) \end{pmatrix}, \end{aligned} \tag{3.10}$$

where the tilde denotes the Fourier transform. The full lattice Green's function can then be expressed as

$$\widetilde{\boldsymbol{G}}^{-1}(k) = \widetilde{\boldsymbol{G}}_0^{-1}(k) - \widetilde{\mathbf{\Sigma}}(k), \tag{3.11}$$

where $\mathbf{\Sigma}$ is the self-energy due to $\lambda \neq 0$. This point is paramount to EMFT and similar methods. The Green's function is known at some point in parameter space, at $\lambda = 0$ in this case, and the deviation of the full Green's function from the known one can be quantified by a function that depends on the interaction, λ. The aim is then to find a simpler but (at least approximately) equivalent model which can be solved more easily than the full model. If the simpler model yields

the same interaction-dependent deviation of the Green's function as the full model, solving the simpler model is equivalent to solving the full model. If the simpler model is only approximately equivalent then naturally an approximate solution is obtained. It can also happen that the simpler model is a valid approximation only in some limited regime such that it can only be used to determine some subset of all observables of the full model. We will now derive an equivalent model to eq. (3.4) which will turn out to be valid for local observables.

As in any MF approach we expand the field $\boldsymbol{\Phi}$ around its (real) mean, $\langle \boldsymbol{\Phi} \rangle = \bar{\phi}$: $\boldsymbol{\Phi} = \bar{\phi} + \boldsymbol{\delta\Phi}$. Focusing on the field at the origin, $\boldsymbol{\Phi}_0$, the action can be written as

$$\begin{aligned} S &= S_0 + \delta S + S_{\text{ext}}, \\ S_0 &= \frac{\eta}{2}|\boldsymbol{\Phi}_0|^2 + \frac{\lambda}{4}|\boldsymbol{\Phi}_0|^4 - 2\bar{\phi}^{\intercal}\boldsymbol{\Phi}_0(d - 1 + \cosh(\mu)), \\ \delta S &= -\sum_{\pm\nu} \boldsymbol{\delta\Phi}^{\dagger}_{0+\hat{\nu}} \boldsymbol{E}(\pm\mu\delta_{\nu,t})\boldsymbol{\delta\Phi}_0. \end{aligned} \tag{3.12}$$

The term S_{ext} does not depend on φ_0 and is irrelevant for our purpose. The term δS contains the interaction of $\boldsymbol{\Phi}_0$ with its nearest neighbors $\boldsymbol{\Phi}_{0\pm\hat{\nu}}$, which are to be integrated out. The field at those sites is collectively denoted by φ_{ext}. The integration over φ_{ext} is formally done by replacing δS by its cumulant expansion with respect to S_{ext},

$$Z = \int \mathrm{d}\varphi_0 \mathcal{D}\varphi_{\text{ext}}\, e^{-S_0 - \delta S - S_{\text{ext}}} = \int \mathrm{d}\varphi_0\, e^{-S_0 - \langle \delta S \rangle^{\text{C}}_{\text{ext}}}, \tag{3.13}$$

where $\langle \delta S \rangle^{\text{C}}_{\text{ext}}$ denotes the cumulant expansion. To second order in the fluctuation $\boldsymbol{\delta\Phi}_0$ it reads:

$$\begin{aligned} \langle \delta S \rangle^{\text{C}}_{\text{ext}} &\approx \left\langle \sum_{\pm\nu} \boldsymbol{\delta\Phi}^{\dagger}_{\hat{\nu}} \boldsymbol{E}(\pm\mu\delta_{\nu,t})\boldsymbol{\delta\Phi}_0 \right\rangle_{S_{\text{ext}}} \\ &\quad + \frac{1}{2}\left\langle \sum_{\pm\nu} \boldsymbol{\delta\Phi}^{\dagger}_{\hat{\nu}} \boldsymbol{E}(\pm\mu\delta_{\nu,t})\boldsymbol{\delta\Phi}_0 \sum_{\pm\rho} \boldsymbol{\delta\Phi}^{\dagger}_{\hat{\rho}} \boldsymbol{E}(\pm\mu\delta_{\rho,t})\boldsymbol{\delta\Phi}_0 \right\rangle_{S_{\text{ext}}} \\ &= 0 + \frac{1}{2}\boldsymbol{\delta\Phi}^{\dagger}_0 \boldsymbol{\Delta} \boldsymbol{\delta\Phi}_0. \end{aligned} \tag{3.14}$$

The first term is zero because $\langle \boldsymbol{\delta\Phi}_{\hat{\nu}} \rangle_{S_{\text{ext}}} = 0$ by definition and $\boldsymbol{\Delta}$ is an unknown real, symmetric matrix which is related to the second term and will be determined self-consistently. $\boldsymbol{\Delta}$ is given by a sum of real bosonic propagators and is therefore real. It is symmetric since the

fields commute, i.e. $\langle \varphi_i \varphi_j \rangle = \langle \varphi_j \varphi_i \rangle$. In our case we can parametrize $\mathbf{\Delta}$ as

$$\mathbf{\Delta} = \begin{pmatrix} \Delta_{11} & \Delta_{12} \\ \Delta_{12} & \Delta_{11} \end{pmatrix}. \tag{3.15}$$

We truncate the cumulant expansion at quadratic order in $\delta\mathbf{\Phi}$ for simplicity. In principle, keeping-higher order terms provides a way to systematically improve the approximation but it may be hard to find suitable self-consistency conditions for the higher-order couplings. Inserting the truncated expansion in eq. (3.13) and using $\delta\mathbf{\Phi}_0 = \mathbf{\Phi}_0 - \bar{\phi}$ yields an effective one-site action

$$\begin{aligned} S_{\text{EMFT}} = &\frac{1}{2}\mathbf{\Phi}^\dagger \left(\eta \text{Id}_2 - \mathbf{\Delta}\right) \mathbf{\Phi} + \frac{\lambda}{4}|\mathbf{\Phi}|^4 \\ &- 2\phi \text{Re}[\varphi](2(d - 1 + \cosh(\mu)) - \Delta_{11} - \Delta_{12}). \end{aligned} \tag{3.16}$$

Since the EMFT action is real, 0-dimensional and bounded from below, the partition function and all observables can easily be calculated via a numerical integration scheme over two variables.

Like the full Green's function above, the EMFT Green's function can be expressed as a free part and a self-energy,

$$\boldsymbol{G}^{-1}_{\text{EMFT}} = \eta \text{Id}_2 - \mathbf{\Delta} - \mathbf{\Sigma}_{\text{EMFT}}. \tag{3.17}$$

Replacing the full self-energy in eq. (3.11) by the EMFT self-energy completes the mapping. It should now be noted that since the effective EMFT model is a single site model, we can only expect it to correctly reproduce local observables. If we had taken the entire cumulant expansion in eq. (3.14) then the effective action would exactly correspond to the full theory and would generate all local observables. Substituting $\mathbf{\Sigma}_{\text{EMFT}}$ into eq. (3.11) yields

$$\widetilde{\boldsymbol{G}}^{-1}(k) \approx \boldsymbol{G}^{-1}_{\text{EMFT}} + \mathbf{\Delta} - 2\sum_{\nu=1}^{d} \cos\left(k_\nu - i\mu\delta_{\nu,t}\right) \text{Id}_2. \tag{3.18}$$

Notice that we here have neglected that the imaginary part of the two diagonal elements in $\widetilde{\boldsymbol{G}}$ differ. On the one hand this is justified since after integrating over all k the result will be real. On the other hand it allows us to easily invert the propagator and one can show that the neglected terms in $\widetilde{\boldsymbol{G}}(k)$ are regular as k_t goes to zero whereas the propagator itself diverges at the critical point, so this approximation will at most change the UV behavior of the theory.

In order to fix $\boldsymbol{\Delta}$ we need to identify the local full lattice Green's function with the EMFT Green's function, which together with the self-consistency for ϕ yields a set of three coupled self-consistency equations,

$$\phi = \langle \varphi \rangle_{S_{\text{EMFT}}}, \tag{3.19}$$

$$\int \frac{\mathrm{d}^d k}{(2\pi)^d} \widetilde{\boldsymbol{G}}(k) \equiv \boldsymbol{G}_{xx} = \boldsymbol{G}_{\text{EMFT}}, \tag{3.20}$$

where the matrix eq. (3.20) yields two independent equations, one for the diagonal element and one for the off-diagonal element. These equations are satisfied at stationary points of the (approximate) local free energy functional [84].

In order not to be hampered by high dimensionality and/or many components in the field it is important to evaluate the k integral in an efficient way. By diagonalizing $\widetilde{\boldsymbol{G}}^{-1}(k)$ we can transform the d-dimensional integral into a 1-dimensional one, which gives

$$\boldsymbol{G}^{\pm}_{xx} = \frac{1}{2} \int_0^\infty \mathrm{d}\tau \left(e^{-\tau\left(\frac{1}{2\langle(\mathrm{Re}\varphi)^2\rangle} + \Delta_{11} + \Delta_{12}\right)} \pm e^{-\tau\left(\frac{1}{2\langle(\mathrm{Im}\varphi)^2\rangle} + \Delta_{11} - \Delta_{12}\right)} \right) \left(I_0(2\tau)\right)^d, \tag{3.21}$$

where $\boldsymbol{G}^{+}_{xx}$ is the diagonal element, $\boldsymbol{G}^{-}_{xx}$ the off-diagonal element and $I_0(x)$ is the zeroth modified Bessel function of the first kind. More details on the transformation of the integral can be found in section 2.4.1.

3.4.2 *Finite lattices*

Because the self-consistency eq. (3.20) involves a k sum, the results will depend on how we define our lattice model. For example, we can treat nonzero temperature simply by summing over a finite number of time-like momenta, k_t. We can equally well consider a finite sized spatial box. In fact, we can easily study the model on any hypercubic lattice with $(N_x, N_y, N_z, N_t) \in \{2, \ldots, \infty\}$.

3.4.3 *Observables*

Through the self-consistency equations we have direct access to the expectation value of the field and the local Green's function. Another

interesting and nontrivial observable is the density, n, which is defined as the partial derivative of the free energy, or logarithm of the partition function, with respect to the chemical potential. By recasting the nearest neighbor interaction of the original action, eq. (3.4), in Fourier space one finds that the density can be expressed as

$$n = 2\sinh\mu\,\langle\varphi\rangle^2 + 2\left(\sinh\mu\int\frac{\mathrm{d}^d k}{(2\pi)^d}\mathrm{Re}[\langle\varphi^*(k)\varphi(k)\rangle_c]\cos(k_t)\right. \\ \left. -\cosh\mu\int\frac{\mathrm{d}^d k}{(2\pi)^d}\mathrm{Im}[\langle\varphi^*(k)\varphi(k)\rangle_c]\sin(k_t)\right). \tag{3.22}$$

The correlator $\langle\varphi^*(k)\varphi(k)\rangle_c$ is nothing else than the connected Green's function, which in our local approximation is given by the diagonal elements of $\widetilde{\boldsymbol{G}}(k)$. Below, we show that the two weighted integrals cancel at zero temperature and exhibit a weak μ dependence at nonzero temperatures. This is exactly the (pseudo) Silver Blaze behavior [37].

To show that the the two integrals cancel, we assume here that $\mu \geq 0$ but note that the density is odd in μ. We have to deal with the two integrals

$$I_R \equiv \sinh\mu\int\frac{\mathrm{d}^d k}{(2\pi)^d}\mathrm{Re}[\langle\varphi^*(k)\varphi(k)\rangle_c]\cos(k_t), \tag{3.23}$$

$$I_I \equiv \cosh\mu\int\frac{\mathrm{d}^d k}{(2\pi)^d}\mathrm{Im}[\langle\varphi^*(k)\varphi(k)\rangle_c]\sin(k_t), \tag{3.24}$$

where the correlator is the diagonal element of $\widetilde{\boldsymbol{G}}(k)$. To decouple k_t from the other momenta we use the same trick as in section 2.4.1. Considering only the integral over k_t we have

$$I_R \propto \sinh\mu\int\frac{\mathrm{d}k_t}{2\pi}\mathrm{Re}\left[\exp\left(2\tau\cos(k_t - i\mu)\right)\right]\cos(k_t), \tag{3.25}$$

$$I_I \propto \cosh\mu\int\frac{\mathrm{d}k_t}{2\pi}\mathrm{Im}\left[\exp\left(2\tau\cos(k_t - i\mu)\right)\right]\sin(k_t), \tag{3.26}$$

where τ is an auxiliary integration variable. Noting that everything not depending on k_t is the same for the two terms we find after some algebra that the difference

$$I_R - I_I \propto \mathrm{Re}\left[\int\frac{\mathrm{d}k_t}{2\pi}\exp(2\tau\cos(k_t - i\mu))\left(\exp(i(k_t - i\mu))\right.\right. \\ \left.\left. -\exp(-i(k_t - i\mu))\right)\right]. \tag{3.27}$$

This expression can be further simplified using the modified Bessel function identity

$$\exp(z\cos(w)) = \sum_{l=-\infty}^{\infty} I_l(z)\exp(iwl). \tag{3.28}$$

The integrand is just a sum of weighted exponentials, $\exp(ik_t n)$ for integer n, and the k_t integral is non-vanishing only when $n = 0$. This selects $I_{-1}(2\tau)$ and $I_1(2\tau)$, which are identical for real arguments, hence the difference vanishes. If we consider a nonzero temperature the momentum can only take discrete values, $k_t = \frac{2\pi}{N_t} n$, $n \in \{0, \ldots, N_t - 1\}$, and the sum over n yields a nonzero contribution when $l + 1 = \pm m N_t$. Combining the two we find

$$\begin{aligned} I_R - I_I &\propto \sum_{l=1}^{\infty} \left(I_{N_t l - 1}(2\tau) - I_{N_t l + 1}(2\tau)\right) \sinh(\mu N_t l) \\ &= \frac{N_t}{\tau} \sum_{l=1}^{\infty} l I_{N_t l}(2\tau) \sinh(\mu N_t l), \end{aligned} \tag{3.29}$$

which is positive and goes to zero as $N_t \to \infty$.

3.4.4 *Extra constraints*

We have demonstrated that EMFT produces an approximation of the full Green's function. It is therefore tempting to extract observables from it, the prime example being the masses of $\varphi_{1,2}$, $m_i^2 = \boldsymbol{G}_{ii}^{-1}(0)$. This is also fine as long as one keeps in mind that the resulting masses are only approximate. In particular one may obtain a nonzero mass for φ_2 although the Nambu-Goldstone theorem tells us it must be zero. That this may happen can be quite easily demonstrated. Consider the (exact) local propagator,

$$\begin{aligned} G_{xx} &= \int \mathrm{d}k \, (\widetilde{G}_0(k)^{-1} - \widetilde{\Sigma}(k))^{-1} \\ &\equiv Z^{-1} \int \mathrm{d}k \, (M^2_{\text{exact}} + \hat{k}^2 - \widehat{\widetilde{\Sigma}}(k))^{-1}, \end{aligned} \tag{3.30}$$

where $\hat{k}$ is the lattice momentum, $\widehat{\widetilde{\Sigma}}(k)$ only contains terms higher than quadratic in k, and Z is the wave function renormalization. This

is matched to the EMFT local propagator through the self-consistency eq. (3.20),

$$G_{\mathrm{EMFT}} = \int \mathrm{d}k\, (\widetilde{G}_0(k)^{-1} - \Sigma_{\mathrm{EMFT}})^{-1} \equiv \int \mathrm{d}k\, (M^2_{\mathrm{EMFT}} + \hat{k}^2)^{-1}. \quad (3.31)$$

Comparing the two equations above we see that M^2_{exact} and M^2_{EMFT} do not have to coincide for the local Green's functions to be equal. Thus, whilst ZM^2_{exact} is the curvature of the effective potential and has a zero eigenvalue, the same need not apply to M^2_{EMFT}. This argument is independent of whether we truncate the cumulant expansion or not. We can of course explicitly calculate the effective potential, which by construction respects the $U(1)$ symmetry and correctly has a flat direction at its minimum. Another option is to slightly modify the EMFT equations to force the Goldstone mode to be massless by introducing an extra constraint.

To do so we first extract the mass matrix $\boldsymbol{M}^2$ from eq. (3.18):

$$\begin{aligned}\widetilde{\boldsymbol{G}}^{-1}(\vec{0}, k_t) &\propto \boldsymbol{M}^2 + k_t^2 \mathrm{Id}_2 \quad (3.32)\\ &= \frac{\boldsymbol{G}^{-1}_{\mathrm{EMFT}} + \boldsymbol{\Delta}}{\cosh\mu} - \frac{2(d + \cosh\mu - 1)}{\cosh\mu}\mathrm{Id}_2 + \mathrm{k}_\mathrm{t}^2 \mathrm{Id}_2.\end{aligned}$$

As we have seen above, there is no guarantee that there will be massless mass eigenstates at the self-consistent fixed point. We will enforce this by hand with an additional parameter. It is a fact that the momentum dependence of the interacting Green's function differs from that of the free Green's function so it is natural to introduce the new parameter in such a way that the momentum dependence is changed. Consider the substitution,

$$\boldsymbol{\Sigma}(k) \to \boldsymbol{\Sigma}_{\mathrm{EMFT}}, \quad (3.33)$$

that we made in eq. (3.11) to obtain eq. (3.18) via eq. (3.17). We now propose the alternative substitution

$$\boldsymbol{\Sigma}(k) \to \boldsymbol{\Sigma}_{\mathrm{EMFT}} + 2(Z-1)\sum_{\nu=1}^{d} \cos(k_\nu - i\mu\delta_{\nu,t})\mathrm{Id}_2 \quad (3.34)$$

which leads to

$$\widetilde{\boldsymbol{G}}^{-1}(k) \approx \boldsymbol{G}^{-1}_{\mathrm{EMFT}} + \boldsymbol{\Delta} - 2Z\sum_{\nu=1}^{d} \cos\left(k_\nu - i\mu\delta_{\nu,t}\right)\mathrm{Id}_2 \quad (3.35)$$

Table 3.1: Comparison of the critical chemical potential, $\mu_c(T=0)$ of four-dimensional complex φ^4-theory at $\lambda = 1$ obtained by MF theory, EMFT, Monte Carlo [50] and complex Langevin [2].

η	9.00	7.44
Mean field theory	1.12908	-
EMFT	1.14582	0.17202
Monte Carlo	1.146(1)	0.170(1)
Complex Langevin	≈ 1.15	-

and the mass matrix

$$M^2 = \frac{G_{\mathrm{EMFT}}^{-1} + \Delta}{Z \cosh \mu} - \frac{2(d + \cosh \mu - 1)}{\cosh \mu} \mathrm{Id}_2. \tag{3.36}$$

The wave function renormalization Z is fixed by the condition that the Goldstone boson is massless. The implementation of this change in the algorithm is straightforward. Although theoretically cleaner, we find that the introduction of the parameter Z has a negligible impact on the numerical solution: In the vicinity of the phase transition $(Z-1)$ is smaller than 10^{-4}. This is because the Goldstone boson is almost massless already and only a very small correction is needed.

3.5 RESULTS

Just as in the real φ^4 theory [10] we find that EMFT predicts the location of the phase transition, in this case the critical chemical potential μ_c, with high accuracy. In table 3.1 we summarize μ_c at zero temperature for two values of η at $\lambda = 1$ for MF theory, EMFT, Monte Carlo [50] and complex Langevin [2].

We ultimately want to apply EMFT to models with nonzero temperature, but as a first test we will study the finite volume behavior since it is more predictable. Let us vary the spatial extent of the lattice and consider the finite volume corrections to μ_c. These arise since the particles interact with their mirror images on the periodically continued lattice. Because the interaction is repulsive the mass will get a positive correction at finite volume, $m(L) > m(\infty)$. The interaction is through

particle exchange and hence the potential is of the Yukawa type. The potential in four dimensions is given by

$$V(r) \propto \frac{1}{r^2}(mr)K_1(mr), \tag{3.37}$$

where $K_1(x)$ is a modified Bessel function which decays exponentially for large arguments. The distance between two mirror particles is $L = aN_s$. The decay is thus governed by $mL = (am_R)N_s$ which allows us to measure am_R by considering lattices of different sizes. Unless mL is rather large it is important to consider particles which wind around the periodic dimensions more than once. At criticality the correlation length diverges, i.e. the inverse propagator vanishes at $k = 0$. From the general form of the propagator (eq. (3.10)),

$$G^{-1}(k) = Z\left((am_R)^2 + 4\sum_\nu \sin\left(\frac{ak_\nu - ia\mu\delta_{\nu,t}}{2}\right)^2\right), \tag{3.38}$$

we obtain $am_R = 2\sinh(a\mu_c/2)$, which reduces to $m_R = \mu_c$ in the continuum limit. In fig. 3.1 we plot $(\mu_c(L) - \mu_c(\infty))/\mu_c(\infty)$ as a function of $\mu_c(\infty)L$ for two different values of η together with the expected behavior, eq. (3.37), with the mass m_R fixed to its infinite volume value $m(\infty)$. The results are largely independent of η, i.e. the finite lattice spacing effects are negligible, and the mass in eq. (3.37) is clearly given by $\mu_c(\infty)$. We also see that at small volumes the mirror images at distances larger than L start to play a role, but since we will work directly in the thermodynamic limit in the following, this is of no concern to us.

3.5.1 *Finite temperature*

One major advantage of EMFT over standard MF theory is the access to finite temperature effects. To turn on temperature we simply truncate the sum over k_t in eq. (3.20) at some finite value of N_t. This lets us define a temperature in lattice units, $aT = N_t^{-1}$, or in units of the chemical potential, $T/\mu = ((a\mu)N_t)^{-1}$. By solving the self-consistency equations at different values of N_t we can obtain all observables as a function of the temperature at fixed lattice spacing. Our main result is the $(T/\mu_c, \mu/\mu_c)$ phase diagram which is shown in fig. 3.2. We have determined it for two lattice spacings, $\eta = 9$ and $\eta = 7.44$, to allow for a direct comparison with Monte Carlo results obtained by Gattringer

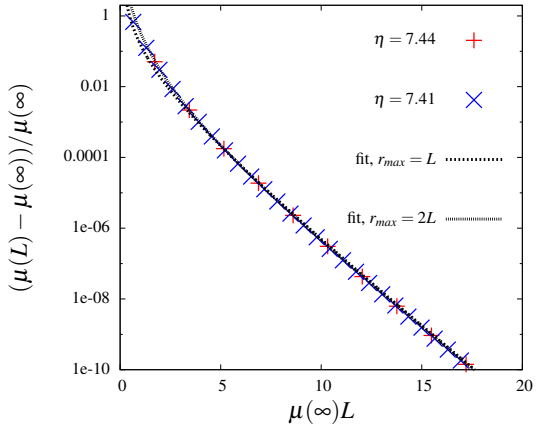

Figure 3.1: The relative deviation of the critical chemical potential μ_c due to finite size effects as a function of the spatial extent of the lattice, L, on an $L^3 \times \infty$ lattice. We fit the amplitude of a sum of Yukawa potentials, eq. (3.37), taking mirror particles up to the distance $r_{\max}$ into account. In both cases the common amplitude of the Yukawa potentials is the only free parameter. The mass is fixed to $\mu_c(\infty)$.

and Kloiber [50]. In Ref. [50] the authors used a world-line formulation of the partition function, which has no sign problem, and sampled the configuration space with a Monte Carlo algorithm. The agreement is excellent at all temperatures and for both values of η.

Also the EMFT estimate of the density as a function of μ at various temperatures agrees with the Monte Carlo results to high accuracy. Again we compare to the Monte Carlo simulations in [50] with $\lambda = 1$, $\eta = 9$ and $\lambda = 1$, $\eta = 7.44$. The result is shown in fig. 3.3. At $\eta = 9$ (*left panel*) the finite volume effects in the Monte Carlo data are small and the EMFT and Monte Carlo results agree almost perfectly. Since the nonzero temperature contribution to the density, eq. (3.22), is closely related to the Green's function at separation a, we conclude that EMFT is not restricted to predicting the local Green's function G_{xx}. At $\eta = 7.44$ (*right panel*), we are closer to the continuum limit, which means that the physical volume of the lattice is smaller in the Monte Carlo simulation. This manifests itself as a rounding of the phase transition. This rounding is absent in EMFT since the volume in these calculations

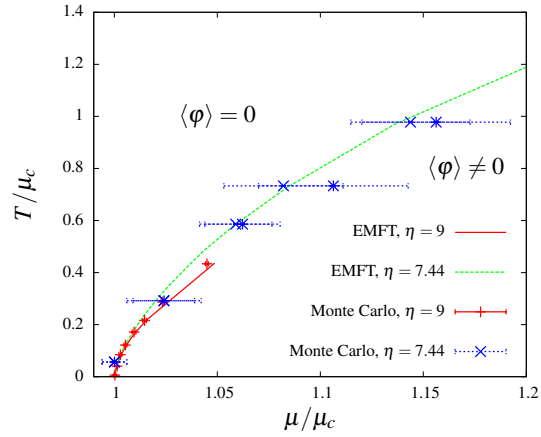

Figure 3.2: $(T/\mu_c(T=0), \mu/\mu_c(T=0))$ phase diagram of complex φ^4 theory at $\lambda = 1$ obtained by EMFT and world line Monte Carlo (Gattringer and Kloiber [50]). The two different blue symbols correspond to different observables used in determining the transition point, $\times$ for the variance of φ and $*$ for the density. We have used two values of η and the results agree very well for both.

is always infinite. Away from the transition the two methods agree very well also at the smaller value of η.

3.5.2 *Dimensional reduction*

At nonzero temperature the theory is expected to undergo a dimensional reduction near the phase transition. This is because the time extent of the lattice becomes much smaller than the correlation length. In a lattice simulation of the full model it might be hard to see this happening for three reasons. Firstly, it is expensive to increase the lattice volume, hence the time extent might not be a small enough fraction of the spatial extent. Secondly, due to the Ginzburg criterion, the correlation length must not be small compared to the time extent or the system will not realize dimensional reduction. Lastly, finite lattice spacing corrections are of the form a^2 and might conceal the true critical behavior when large. All this taken together provides a considerable challenge for Monte Carlo simulations.

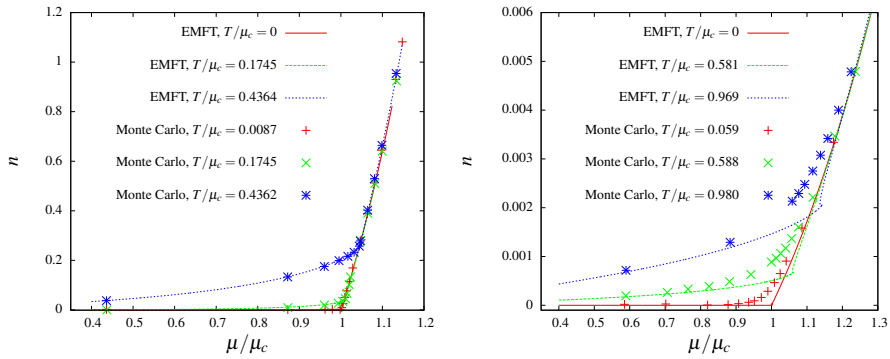

Figure 3.3: The density n, eq. (3.22), as a function on μ for a few different temperatures, $T/\mu_c \equiv 1/(N_t \mu_c(T=0))$, at $\lambda = 1$, $\eta = 9$ (*left panel*) and $\lambda = 1$, $\eta = 7.44$ (*right panel*). The Monte Carlo data [50] were obtained on a $N_s^3 \times N_t$ lattice with $N_s = 20$ for $\eta = 9$ and $N_s = 24$ for $\eta = 7.44$. The small temperature differences come from slightly different values of $\mu_c(T=0)$, see table 3.1. The EMFT results are obtained in the thermodynamic limit, i.e. $N_s = \infty$.

EMFT works best in the thermodynamic limit and does not suffer from critical slowing down close to the continuum limit and can thus overcome all these problems. EMFT is, in other words, well suited for an investigation of dimensional reduction. When $T > 0$ we expect that the critical exponents change from MF to those of the three-dimensional XY-model universality class. Two critical exponents easily accessible to us are β and ν. fig. 3.4 shows the expectation value of the field and the correlation length as a function of $\mu - \mu_c$ for zero and nonzero temperatures. At zero temperature we find $\beta = \nu = 0.50$. For finite temperature the power laws change to approximately $1/3$ which is not the behavior expected for the $3d$ XY-model ($\beta \approx 0.33, \nu \approx 0.67$) but rather what is expected close to a genuine first-order transition in three dimensions.

3.5.3 *First-order transition*

We have seen that the four-dimensional model dimensionally reduces as temperature is turned on, but the EMFT incorrectly predicts a first order transition in this case. The strength of this first-order transition is

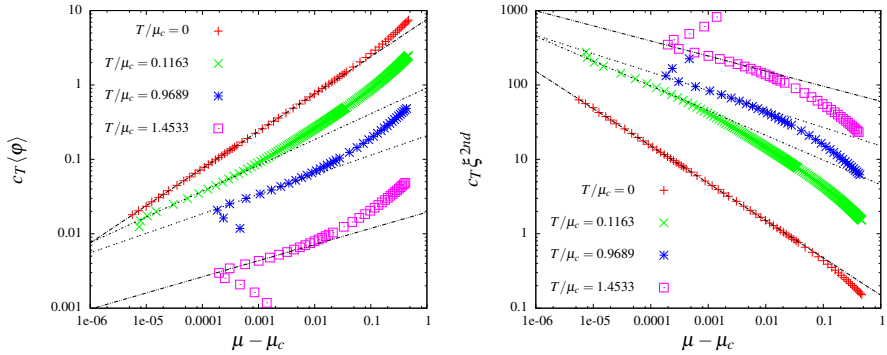

Figure 3.4: The expectation value of the field, $\langle \mathrm{Re}\varphi \rangle$ (*left panel*), and the correlation length, ξ (*right panel*), as a function of the distance to the critical chemical potential for a few different temperatures at $\lambda = 1$ and $\eta = 7.44$ on a log-log scale. We see how the power law changes from 0.5 at zero temperature to approximately $1/3$ at finite temperature for both observables. To increase readability the curves have been multiplied by $c_T = 15, 5, 1$ and 0.1, going from top to bottom.

however quite weak, which can be seen from the value of the correlation length in fig. 3.4 (notice the shift of the curves). Although EMFT still produces quantitatively good predictions of various observables such as the critical chemical potential and the density, this is of course an undesired feature. It is interesting to quantify the strength of the first-order transition, which can be done by determining how the jump in the expectation value depends on the temperature. We define $\langle \phi \rangle_J$ to be the value of $\langle \varphi \rangle$ at the chemical potential where $\partial \langle \varphi \rangle / \partial \mu = \infty$ (cf. left panel of fig. 3.4). In fig. 3.5 we plot $\langle \phi \rangle_J / \mu_c$ versus T/μ_c. $\langle \phi \rangle_J$ grows slightly less than linearly in T but seems to approach a linear behavior with a coefficient of about 0.14 as we approach the continuum limit.

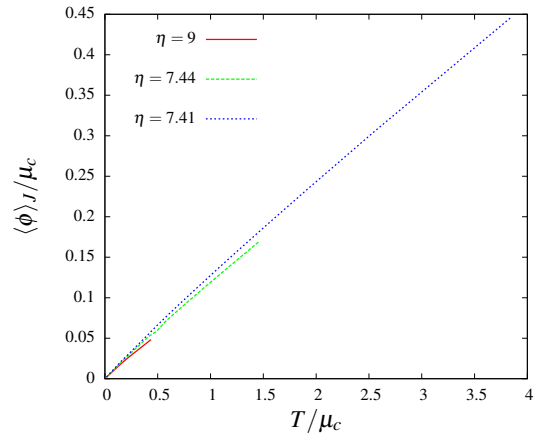

Figure 3.5: The expectation value of the field at the chemical potential where $\partial \langle\varphi\rangle / \partial\mu = \infty$ as a function of the temperature, both made dimensionless by division by $\mu_c(T = 0)$.

4

OSCILLATING PROPAGATORS IN HEAVY-DENSE QCD

4.1 INTRODUCTION

In this chapter we study the $\mathbb{Z}_3$ spin model with nonzero chemical potential μ in 1 and 3 dimensions and show that a complex mass spectrum can occur in both cases. The motivation for this investigation is two-fold. On the one hand, it can be shown analytically [71] that one-dimensional models with complex saddle points will sometimes have a complex mass spectrum and it has been conjectured [79] that this also holds in higher dimensions. From a purely conceptual point of view, it is thus interesting to confirm this conjecture via lattice simulations. On the other hand, oscillating propagators due to a complex mass spectrum can also have interesting phenomenological implications, in particular in the context of heavy-ion collisions [82]. EMFT can be used to quickly scan the parameter space of the model we want to study and thus find interesting regions which can be further investigated using Monte Carlo simulations.

The content of this chapter has been published in

- Oscar Akerlund, Philippe de Forcrand, and Tobias Rindlisbacher. „Oscillating propagators in heavy-dense QCD.“ in: (2016). Submitted to JHEP. arXiv: 1602.02925 [hep-lat].

4.2 MODEL

As mentioned in the introduction (chapter 1), it has been suggested [82] that the conditions in the fireball after a heavy-ion collision might be such that the baryon-number correlations have an oscillatory character. This conjecture is based on an effective flux-tube model introduced in [81, 83] which can be mapped into an XY-model with external magnetic fields which break charge symmetry, such that it falls in the same category of models discussed above. Another flux-tube model, which can be mapped into a three-state Potts model, is treated in [38].

In general, the Hamiltonian and partition function for such a flux-tube model are given by

$$H = \sigma \sum_{x,\nu} |l_{x,\nu}| + m \sum_x |q_x| + v \sum_x |j_x|, \quad Z = \sum_{\{l_{x,\nu}, q_x, j_x\}} e^{-\beta(H - \mu \sum_x q_x)}, \tag{4.1}$$

where $l_{x,\nu}$ denote flux tubes with string tension σ living on the links, q_x denote quarks with mass m and chemical potential μ living on the sites and j_x denote junctions with vertex energy v living on the sites. All occupation numbers are integer valued and, depending on their allowed range and on whether v is zero or nonzero, the model can be mapped to either an XY model or a Z_N spin model. The junctions j call for further explanation. In $SU(N)$, they are related to the invariant ϵ-tensor, i.e. N flux lines emanating from N (anti-)quarks join at a junction and form an $SU(N)$ singlet, and thus the (anti-)quarks together with the flux lines are identified with a (anti-)baryon.

The model we will be studying is the three-states Potts model with nonzero chemical potential or, more accurately, the $\mathbb{Z}_3$ spin model with complex external fields [1]. In d dimensions, it can be seen as the crudest approximation of $(d+1)$-dimensional QCD in the heavy-dense limit. The action is given by

$$S = -\beta \sum_{\langle i,j \rangle} \left(P_i P_j^\dagger + P_i^\dagger P_j \right) - 2 \sum_i \left(h_R \mathrm{Re} P_i + i h_I \mathrm{Im} P_i \right), \tag{4.2}$$

and the $\mathbb{Z}_3$ spins $P \in \{1, e^{i\frac{2\pi}{3}}, e^{-i\frac{2\pi}{3}}\}$ at each site represent the center of the Polyakov loops $\mathrm{Tr}_F\, L$. The usual interpretation of the external fields is $h_R = e^{-M/T} \cosh(\mu/T), h_I = e^{-M/T} \sinh(\mu/T)$, where M and μ are the mass and chemical potential of the quarks respectively [12], but one can consider also alternative mappings, for example to the flux-tube model described in [38] [2]. We will primarily use the first mapping but will evaluate the results also in the light of the second one.

In the formulation (4.2) the action is complex, and the model clearly suffers from a sign problem, but as long as $h_R, h_I \in \mathbb{R}$ and $h_R > |h_I|$, which corresponds to the physical case of $M, \mu \in \mathbb{R}$, there exists a sign-problem free representation [3] that can be sampled by a worm

1 It may be worth pointing out that this type of model is often called a 3-state Potts model. This is not entirely accurate since the $\mathbb{Z}_3$ spin model (4.2) is only equivalent to a 3-state Potts model if $h_I = 0$.

2 See especially eqs. (14-18) in that reference.

3 This is essentially going back to the representation in terms of flux-tube variables

algorithm. The model can however be interesting in its own right also in the unphysical region $h_I > h_R$. In one dimension the model can be solved for general external fields using a transfer-matrix method and we can use EMFT to obtain an approximate solution in any number of dimensions.

4.2.1 *Transfer matrix*

In $(0+1)$ dimensions the partition function of a chain of N $\mathbb{Z}_3$ spins with periodic boundary conditions is given by

$$Z = \operatorname{Tr} T^N, \quad T \propto \begin{pmatrix} e^{2\beta+2h_R} & e^{-\beta+\frac{h_R}{2}} e^{i\frac{\sqrt{3}h_I}{2}} & e^{-\beta+\frac{h_R}{2}} e^{-i\frac{\sqrt{3}h_I}{2}} \\ e^{-\beta+\frac{h_R}{2}} e^{i\frac{\sqrt{3}h_I}{2}} & e^{2\beta-h_R} e^{i\sqrt{3}h_I} & e^{-\beta-h_R} \\ e^{-\beta+\frac{h_R}{2}} e^{-i\frac{\sqrt{3}h_I}{2}} & e^{-\beta-h_R} & e^{2\beta-h_R} e^{-i\sqrt{3}h_I} \end{pmatrix} \tag{4.3}$$

where T is the transfer matrix. It is easy to verify that the characteristic polynomial of T is a cubic polynomial with real coefficients so there are either three real roots or one real root and a pair of complex conjugate roots, as claimed above. For a given β, it is now straightforward to determine the phase diagram which contains the three phases described in the introduction. The phase diagram at fixed $\beta = 0.08$ can be seen in fig. 4.1. The color coding and labels are as follows: I (blue) marks the region where all eigenvalues of T are real. In Ia they are all positive and the connected correlator is a pure sum of exponentials. In Ib two eigenvalues are negative (the product of all three, i.e. the determinant of T, is always positive) and the connected correlator is in general a sum of two oscillating functions with wavelength 2, due to factors $(-1)^t$. Depending on how the signs and magnitudes of the eigenvalues are distributed, this may or may not be detectable on a discrete lattice. II (green) denotes the region where the largest eigenvalue is real and the other two are a complex conjugate pair. The connected correlator is a cosine-modulated exponential, this is characteristic of a liquid. III (red) marks the region where the complex conjugate pair is larger in magnitude than the real eigenvalue and the connected correlator at long distance is a pure trigonometric function, this is the long-range order characteristic of a crystal. The two black lines bound the wedge where $h_R > |h_I|$ and mark the region where the flux-variables representation is sign-problem free and the worm algorithm can be used. It is evident

that the crystalline phase is out of reach of the worm algorithm but some parts of the liquid phase lie within the physical region $h_R > |h_I|$, so that the non-monotonic behavior of the connected correlator there can be reproduced by lattice simulations. Initially the transfer-matrix method is only defined for integer separations but it is straight forward to extend it to any real separation via the matrix power-function. In the liquid phase, the connected correlator is exactly given by

$$\langle f(P(0))f(P(t))^\dagger\rangle_c = a_f \left(\cosh\left(m_R\hat{t}\right)\cos\left(m_I\hat{t}\right)\cos\phi_f + \sinh\left(m_R\hat{t}\right)\sin\left(m_I\hat{t}\right)\sin\phi_f\right), \quad (4.4)$$

where $\hat{t} = t - N_t/2$ and $f(P)$ is either $P, \mathrm{Re}P$ or $\mathrm{Im}P$. The parameters a_f and ϕ_f can be calculated from the eigenvectors of T. These functions can be directly compared to the correlators obtained by the worm algorithm and will serve as a consistency check for the algorithm before going on to three dimensions where no exact results are available. Note that the correlator is even under time-reversal. This is different from the behavior seen in other models [51, 85] where the chemical potential is attached to time-like lattice links.

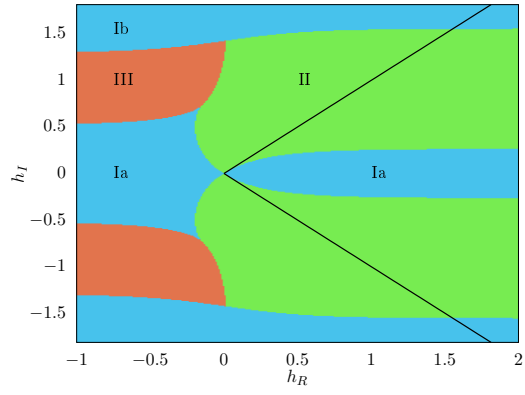

Figure 4.1: Phase diagram of the $1d$ $\mathbb{Z}_3$ spin model in the (h_R, h_I)-plane for fixed $\beta = 0.08$. The crystalline phase III is outside the region of parameter space where the worm algorithm can be applied but the liquid phase II is susceptible to lattice simulations. For a more detailed description of the phases see the text. The phase diagram is periodic in h_I with period $\pi/\sqrt{3}$

A comment about this "phase diagram" is in order. Actually, the different phases are not separated by phase transitions in the strict sense; there is no singularity in the free energy anywhere in the (h_R, h_I)-plane, since the zeros of the characteristic polynomial of T are smooth functions over the whole plane. Instead, the boundary of the different phases are *disorder lines*, which mark a smooth change in the characteristic of the correlator, for example from a non-oscillatory exponential decay to an oscillatory exponential decay. In general, however, it is not necessarily so that the change from non-oscillatory to oscillatory behavior take place at a disorder line, it can also occur at a first order transition, as is evident from for example the water-vapor transition.

4.2.2 *EMFT solution*

In more than one dimension, and especially in the physically interesting case of three dimensions, the transfer-matrix method is not practical anymore. It is reasonable to assume that the structure of the phase diagram will remain [79] but one is totally at a loss when it comes to the exact location of the disorder lines. In the light of the one-dimensional results, it is unlikely that the crystalline phase can be probed by lattice simulations, but one may hope to find evidence of a liquid phase. In this case the three largest eigenvalues of the transfer matrix will be given by (up to a trivial overall multiplicative, real constant) $\lambda_0 = 1, \lambda_1 = e^{-m_R - im_I}, \lambda_2 = e^{-m_R + im_I}$, where $m_R, m_I > 0$ are real numbers chosen to paramterize the eigenvalues. The decay of the spin-spin correlator will thus be governed by $\langle P(0)P^\dagger(r)\rangle \sim e^{-m_R r}\cos(m_I r)$. It becomes clear that our prospects for detecting this characteristic behavior of the correlator depend rather sensitively on m_R and m_I; we require a point in phase space where m_R is not too large at the same time as m_I is not too small, so that the first maximum in the correlator occurs before the signal is too damped. Much time and effort can be saved by quickly, albeit approximately, solving the model for extended regions of parameter space. Mean field theory is one candidate which falls short since it does not give access to the mass spectrum. EMFT, as we have already seen, does exactly that and is thus an apt choice.

Once again, it will be instructive to go through the derivation of the effective action and self-consistency equations in some detail. This is because we now expect the mass spectrum to be complex, whereas it has previously been real. It will be useful to consider the real part

$\mathrm{Re}P$ and the imaginary part $\mathrm{Im}P$ of the Potts spin P as independent variables here. Since the imaginary part of the action (4.2) is odd in $\mathrm{Im}P$, the expectation value of $i\mathrm{Im}P$ will be real and we have $\langle P\rangle = \langle \mathrm{Re}P\rangle + \langle i\mathrm{Im}P\rangle \neq \langle \mathrm{Re}P\rangle - \langle i\mathrm{Im}P\rangle = \langle P^\dagger\rangle$. The $\mathbb{Z}_3$ spin P is then decomposed into its mean value and fluctuations around the mean,

$$\begin{aligned} P &= \langle \mathrm{Re}P\rangle + \delta\mathrm{Re}P + \langle i\mathrm{Im}P\rangle + i\delta\mathrm{Im}P, \\ P^\dagger &= \langle \mathrm{Re}P\rangle + \delta\mathrm{Re}P - \langle i\mathrm{Im}P\rangle + -i\delta\mathrm{Im}P. \end{aligned} \tag{4.5}$$

We now formally integrate out all fields except the one at the origin and assume that this amounts to the introduction of effective couplings for the bilinears $\delta\mathrm{Re}P\delta\mathrm{Re}P$, $\delta\mathrm{Im}P\delta\mathrm{Im}P$ and $\delta\mathrm{Re}P\delta\mathrm{Im}P$ [9]. The effective EMFT action can then be written

$$\begin{aligned} S_{\mathrm{EMFT}} = &- (\mathrm{Re}P)^2 \Delta_1 - (\mathrm{Im}P)^2 \Delta_2 - 2i\mathrm{Re}P\mathrm{Im}P\Delta_3 \\ &- 2\mathrm{Re}P\left(h_R + \langle \mathrm{Re}P\rangle (2d\beta - \Delta_1) + \langle i\mathrm{Im}P\rangle \Delta_3\right) \\ &- 2i\mathrm{Im}P\left(h_I + \langle i\mathrm{Im}P\rangle (2d\beta - \Delta_2) - \langle \mathrm{Re}P\rangle \Delta_3\right). \end{aligned} \tag{4.6}$$

So far we have not assumed anything about the variables P so the effective action above is generally valid for any action of the form (4.2). For $P \in \mathbb{Z}_3$ the action can be simplified slightly by using $(\mathrm{Im}P)^2 = 1 - (\mathrm{Re}P)^2$ and $\mathrm{Re}P = -\frac{1}{2}$ whenever $\mathrm{Im}P \neq 0$. We then obtain

$$S_{\mathrm{EMFT}} = - (\mathrm{Re}P)^2 (\Delta_1 - \Delta_2) - 2\mathrm{Re}P\tilde{h}_R - \frac{2}{\sqrt{3}} i\mathrm{Im}P\tilde{h}_I, \tag{4.7}$$

$$\tilde{h}_R = h_R + \langle \mathrm{Re}P\rangle (2d\beta - \Delta_1) + \langle i\mathrm{Im}P\rangle \Delta_3, \tag{4.8}$$

$$\frac{\tilde{h}_I}{\sqrt{3}} = h_I + \langle i\mathrm{Im}P\rangle (2d\beta - \Delta_2) - \left(\langle \mathrm{Re}P\rangle + \frac{1}{2}\right)\Delta_3. \tag{4.9}$$

Defining $\log\gamma = -\frac{3}{4}(\Delta_1 - \Delta_2) - 3\tilde{h}_R$, it is straightforward to calculate all expectation values of the model

$$\langle \mathrm{Re}P\rangle = \frac{1 - \gamma\cos\tilde{h}_I}{1 + 2\gamma\cos\tilde{h}_I} \qquad \langle i\mathrm{Im}P\rangle = \frac{\sqrt{3}\gamma\sin\tilde{h}_I}{1 + 2\gamma\cos\tilde{h}_I} \tag{4.10}$$

$$\left\langle (\mathrm{Re}P)^2\right\rangle = \frac{1 + \frac{1}{2}\gamma\cos\tilde{h}_I}{1 + 2\gamma\cos\tilde{h}_I} \qquad \left\langle (\mathrm{Im}P)^2\right\rangle = -\frac{\frac{3}{2}\gamma\cos\tilde{h}_I}{1 + 2\gamma\cos\tilde{h}_I} \tag{4.11}$$

$$\langle i\mathrm{Im}P\mathrm{Re}P\rangle = \frac{-\frac{\sqrt{3}}{2}\gamma\sin\tilde{h}_I}{1 + 2\gamma\cos\tilde{h}_I}. \tag{4.12}$$

It is obvious how to self-consistently determine the linear expectation values, whereas the bilinears may need some more explanation. The details of their determination will reveal how a complex spectrum can arise. As usual in EMFT [9], we fix the effective quadratic couplings Δ_i by matching the bi-linear expectation values to an approximation to the point-to-point correlator of the full model,

$$\begin{aligned} G_{\mathrm{EMFT},c} &= \int \mathrm{d}^d k \, G_c(k) = \int \mathrm{d}^d k \, \left[G_{0,c}^{-1}(k) + \Sigma(k) \right]^{-1} \\ &\approx \int \mathrm{d}^d k \, \left[G_{0,c}^{-1}(k) + \Sigma_{\mathrm{EMFT}} \right]^{-1} . \end{aligned} \tag{4.13}$$

This is a matrix equation where $G_{0,c}(k)$ is the connected Green's function of the free theory. It is not immediately clear what the free theory of a spin model is, but the approximation above is in fact valid for any choice. A good choice will be close to the model we want to study and at the same time allow for an efficient numerical treatment. We have chosen the free model to have the same action as the original $\mathbb{Z}_3$ model, eq. (4.2), but with the variables P ranging freely over the complex plane. With this choice the free connected Green's function is given by $G_{0,c}^{-1} = -2\beta \mathrm{Id}_2 \sum_\nu \cos k_\nu$. The self-energy $\Sigma(k)$ in eq. (4.13) then arises due to the restriction of the field to take values in $\mathbb{Z}_3$. The EMFT self-energy Σ_{EMFT} is likewise identified as the difference between the variance of eq. (4.6) with $(\mathrm{Re}P, \mathrm{Im}P) \in \mathbb{R}^2$ and the variance when $P \in \mathbb{Z}_3$ and is given by $G_{\mathrm{EMFT},c}^{-1} + \Delta$, with

$$G_{\mathrm{EMFT},c} = 2 \begin{pmatrix} \left\langle (\mathrm{Re}P)^2 \right\rangle_c & -i \left\langle i\mathrm{Im}P\mathrm{Re}P \right\rangle_c \\ -i \left\langle i\mathrm{Im}P\mathrm{Re}P \right\rangle_c & \left\langle (\mathrm{Im}P)^2 \right\rangle_c \end{pmatrix}, \tag{4.14}$$

$$\Delta = \begin{pmatrix} \Delta_1 & i\Delta_3 \\ i\Delta_3 & \Delta_2 \end{pmatrix}, \tag{4.15}$$

with the central moments $\langle AB \rangle_c = \langle AB \rangle - \langle A \rangle \langle B \rangle$. Hence, the final self-consistency equation becomes

$$G_{\mathrm{EMFT},c} = \int \mathrm{d}^d k \, \left[G_{\mathrm{EMFT},c}^{-1} + \Delta - 2\beta \mathrm{Id}_2 \sum_\nu \cos k_\nu \right]^{-1} . \tag{4.16}$$

It is clear that $G_{\mathrm{EMFT},c}^{-1} + \Delta - 2\beta \mathrm{Id}_2 \equiv \beta M$ plays the role of a mass matrix and we should diagonalize it to obtain the mass spectrum. It

will also be vastly more efficient to integrate over the momenta when M is diagonal. The mass matrix can be parametrized as

$$M = \begin{pmatrix} a+b & ic \\ ic & a-b \end{pmatrix}, \tag{4.17}$$

where $a, b, c \in \mathbb{R}$. The eigenvalues are then given by $m_\pm = a \pm \sqrt{b^2 - c^2}$, such that if $|c| > |b|$ the spectrum will consist of a pair of complex conjugated masses $m_R \pm i m_I$ with $m_R = a$ and $m_I = \sqrt{c^2 - b^2}$. This implies cosine-modulated exponential fall-off in the correlators in the $(\mathrm{Re}P, \mathrm{Im}P)$ basis, as expected. By solving the model in the (h_R, h_I)-plane, a phase diagram analogous to what was obtained in one dimension with the transfer matrix, fig. 4.1, can be constructed by studying the behavior of the masses. In fig. 4.2 we show the results for fixed $\beta = 0.08$, with the most interesting features being the disorder lines (in red), where the masses are degenerate, and the blue dashed lines where the real part of the complex masses vanishes. Beyond these lines the momentum integral in the self-consistency equation no longer converges, since the integrand is no longer decaying at large distances. One may guess that with purely imaginary masses, the system would enter a crystalline phase with a purely trigonometric correlator but there is no way to verify that using EMFT. This phase diagram can then be compared both to the mapping $(h_R, h_I) \to (e^{-M/T}\cosh(\mu/T), e^{-M/T}\sinh(\mu/T))$ and to the alternative mapping in [38]. It is found that the second case covers a subspace of $M, \mu \in \mathbb{R}$ and there are indeed regions in parameter space where the mapping is valid and where one expects a complex spectrum. However, in that region h_R is substantially larger than h_I which means in the M, μ variables that both M and μ are rather small, which is presumably far away from the region where the model is expected to be a valid approximation of QCD.

Now that an approximate phase diagram has been obtained, we can select points in the liquid phase which are favorable in terms of m_R and m_I where full Monte Carlo simulations using the worm algorithm will be performed.

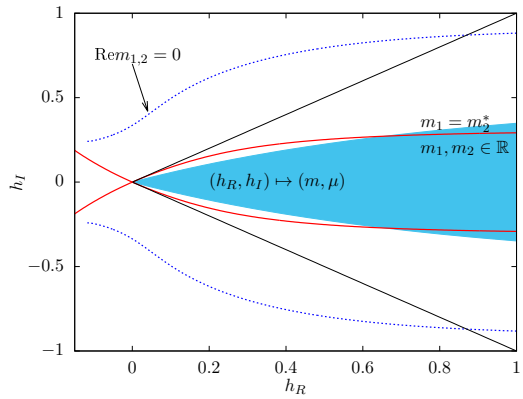

Figure 4.2: Phase diagram of the $3d$ three-states Potts model at fixed $\beta = 0.08$ obtained by EMFT. The thick red lines are disorder lines where the mass spectrum turns complex and on the dashed blue lines the real part of the mass vanishes. Those lines bound the region of convergence of EMFT. Inside the wedge bounded by the thin black lines the model (4.2) is sign-problem free and the blue region marks the image of the map from the standard $\mathbb{Z}_3$ model to the flux-tube model of [38].

4.3 RESULTS

For our lattice simulations we used the flux-variables representation described in [72],

$$Z \propto \sum_{\{l\}} \sum_{\{n\}} \prod_{x,\nu} L^{|l_{x,\nu}|} \prod_x S_{n_x} \prod_x \Delta \left(\sum_\nu (l_{x,\nu} - l_{x-\hat{\nu},\nu}) + n_s \right), \tag{4.18}$$

with quark occupation number $n_x \in \{-1, 0, 1\}$ on each site and flux occupation number $l_{x,\nu} \in \{-1, 0, 1\}$ on each link. In terms of the original parameters the link and site weights are given by

$$L = \frac{1 - e^{-3\beta}}{1 + 2e^{-3\beta}}, \tag{4.19}$$

$$S_n = 1 + 2e^{-3e^{-\frac{M}{T}} \cosh \frac{\mu}{T}} \cos \left(\sqrt{3} e^{-\frac{M}{T}} \sinh \frac{\mu}{T} - n \frac{2\pi}{3} \right). \tag{4.20}$$

Gauss' law requires that the flux at each site is a multiple of three and is encoded in $\Delta(n) = \delta_{n \mod 3,0}$. Allowed configurations consist of flux-tube networks with or without attached quarks. If there are no quarks attached the flux-network can be thought of as a glueball. There are also neutral networks with any number of quarks and an equal number of anti-quarks attached, for example networks connecting one quark with an anti-quark can be thought of as mesons. The third possibility is to have a surplus of $3n$ (anti-)quarks. This is equivalent to having the junctions of the network to sum up to n, we say that the network has junction charge n. These charged networks are associated with baryons.

The worm algorithm generates a Markov chain of allowed configurations by temporarily violating the constraint, something which can be exploited to obtain improved estimators for spin-spin correlation functions. In addition to the usual $\langle P(0)P^\dagger(x)\rangle$ we use a modification introduced in [85, 86], which allows us access to improved estimators of also $\langle \mathrm{Re}P(0)\mathrm{Re}P(x)\rangle$ and $\langle \mathrm{Im}P(0)\mathrm{Im}P(x)\rangle$. This is crucial because the best signal-to-noise ratio will be found in the correlator of the imaginary parts of the spins, since it has the smallest constant background. We first reproduced the results obtained by the transfer matrix method in one dimension in order to verify that the algorithm was properly implemented. A typical correlator in the liquid phase is shown in fig. 4.3 and there is perfect agreement with the analytic result for all three propagators. It should be noted that the real part of the mass m_R

is in general always large when the imaginary part m_I is of order one or larger, this makes it very difficult to resolve the first local maximum of the correlator.

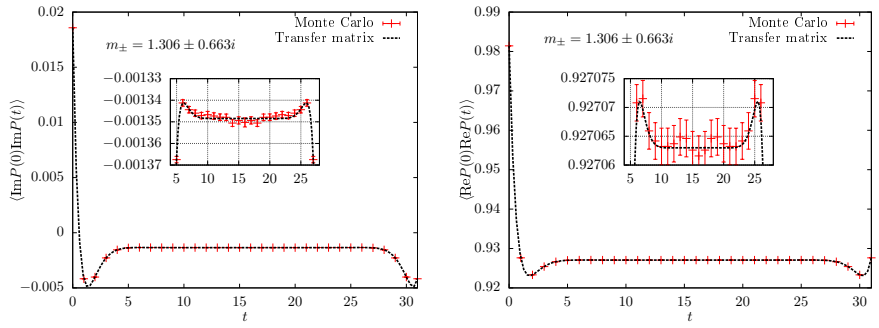

Figure 4.3: Two components of the spin-spin correlator in one dimension for $\beta = 0.5, e^{-M/T} = 0.02$ and $\mu/T = 3.689$. There is a clear oscillation in both correlators and the result agrees perfectly with the exact result obtained using the transfer matrix. The complex mass is given by $m_\pm \approx 1.306 \pm 0.663i$.

We also measured the junction-junction correlator on the configurations generated by the worm algorithm. The junction j_x takes the value n if $3n$, $n \in \mathbb{Z}$ units of flux flow into the site x. With the flux variables described above there are in general four types of junctions, depicted in fig. 4.4 but in one dimension only junction A with one quark and two in-going fluxes (or its reverse) attached to the site is possible. In fig. 4.5 we show the correlation between positive j_+ and negative j_- junctions for two different parameter values. Here the oscillation is even clearer due to a less noisy observable, although we do not have an improved estimator for this correlator. The dashed line is obtained by fitting the amplitude and phase in eq. (4.4) while keeping the masses fixed at the exact values obtained by the transfer matrix. The mass is the same as for the spin-spin correlator since the junction is a local object and there is only one (complex) mass in the one-dimensional case. It should be noted that these parameter values have been selected to give a maximally clear first maximum in the oscillation. For general parameter values in the liquid phase it is only possible to see the first minimum, while the first maximum is drowned in noise. This will be especially true in three dimensions where the real part of the mass is larger than in the one-dimensional case.

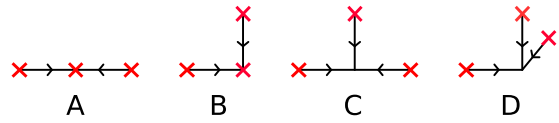

Figure 4.4: The different junctions allowed in the flux-variable representation of the $\mathbb{Z}_3$ model described in the text. The red crosses represent quarks and the lines represent the directed flux-tubes. The junction is located in the center of each network where the flux sums up to three. Note that the quarks bounding the network may also be replaced by arbitrary larger networks of charge one. In one dimension only junction A is possible. The three-dimensional junction D is only present in dimension three or higher.

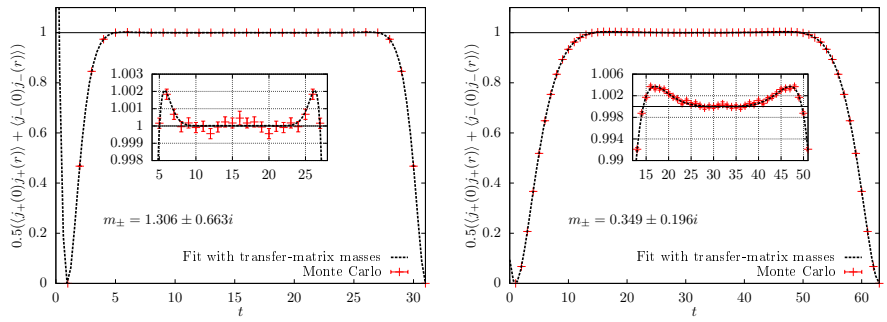

Figure 4.5: The junction-junction correlator in one dimension for $\beta = 0.5, e^{-M/T} = 0.02$ and $\mu/T = 3.689$ (*left panel*) and for $\beta = 1.2, e^{-M/T} = 0.0042$ and $\mu/T = 4$ (*right panel*). The signal of oscillation is even clearer than in the spin-spin correlator since this observable is less noisy, cf. fig. 4.3. The fits are given by eq. (4.4) with the mass fixed at the value obtained with the transfer matrix.

We then move to the physically interesting case of three dimensions, and guided by the phase diagram calculated by EMFT we select a few points assumed to be in the liquid phase and look for the corresponding signals in the correlators. Also here, however, the damping of the correlator is always strong, as is illustrated in fig. 4.6. In the left panel m_R and m_I, obtained by EMFT, are plotted as a function of $\tanh \mu/T$ for fixed M/T and β and in the right panel m_I is plotted as a function of m_R to emphasize the approximately linear growth relation. Both masses increase with μ/T. As a consequence, it is typically only possible to

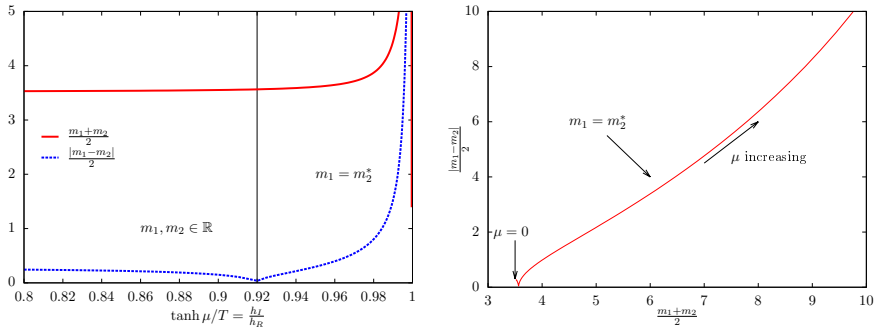

Figure 4.6: *Left*: the masses obtained by EMFT as a function of $\tanh \mu/T = h_I/h_R$ for fixed $\beta = 0.08$ and $e^{-M/T} = 0.05$. *Right*: imaginary part versus real part of the complex mass, for the same parameters as in the left panel. The feature that the real part rises approximatively linearly with the imaginary part is generic, as is the fairly large value of the real part at $\mu = 0$. In the part of the curve to the left of the cusp, both masses are real and their half-difference is shown as a function of their half-sum.

resolve the first minimum of the oscillating correlator. In fig. 4.7 we show correlators of ImP, as a function of the Euclidean distance $r = \sqrt{x^2 + y^2 + z^2}$, obtained by our worm simulations for three different values of the chemical potential $\mu/T \in \{2.0, 2.5, 3.3\}$ at fixed $\beta = 0.08$ and $e^{-M/T} = 0.05$. For all μ there is a clear minimum whose position moves toward zero and whose width decreases as the chemical potential increases. This suggests that the imaginary part of the mass increases with μ, as it does in one dimension and as EMFT predicts. However, there is a clear staggered component in the correlators, which makes it very hard to fit the data to a simple ansatz. The staggered nature of the

correlators most likely stems from the size and shape of the junctions, shown in fig. 4.4. Also, in neither of these correlators is it possible to see a maximum. This is not very surprising, but a discernible maximum would be indisputable evidence of a complex spectrum.

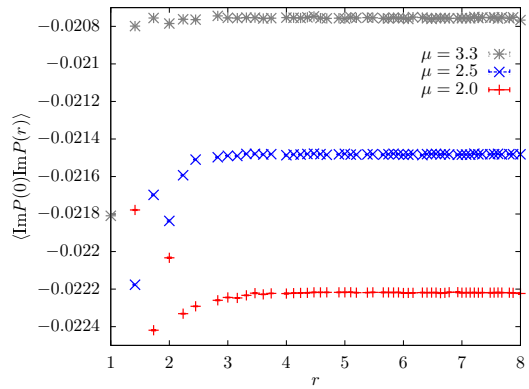

Figure 4.7: The correlator of the imaginary part of the spins for three different chemical potentials μ at fixed $\beta = 0.08$ and $e^{-M/T} = 0.05$. The minimum of the correlator moves towards zero and its width decreases as μ increases, suggesting that the imaginary part of the mass increases with μ, as expected. The significant staggered contribution to the correlator makes a fit to the data difficult. The data sets are shifted vertically for clarity and the data points at $r \leq 1$ are far above the shown data points, i.e. we have zoomed in on the minimum of the correlators.

If the mass spectrum is complex and the system behaves like a liquid then the junction-junction correlator should also show the characteristic, oscillatory behavior seen in the $1d$ model. Since the junction-junction correlator is less noisy than the spin-spin one, one may even hope that a maximum of the oscillating correlator can be resolved, thus establishing the complex spectrum without doubt. In fig. 4.8 we show two junction-junction correlators for $\beta = 0.08, e^{-M/T}$ and $\mu/T = 3.3$. In the left panel we show the correlator of the absolute values of the junctions whereas in the right panel the sign of the junctions is also taken into account. The difference of scales of the two correlators comes from the fact that they are both normalized to one at large distances and that $\langle |j| \rangle \sim 3 \langle j \rangle$. To emphasize the staggered component of the

correlators we plot the correlators on the two different sub-lattices with different colors. Inspecting first the charge-insensitive correlator (*left panel*) we see that there is indeed a depletion in the density of junctions of any type within distance $[1, 2.5]$ of a junction but it is not possible to tell if this minimum is followed by a maximum. In the charge-sensitive correlator (*right panel*) there is a clear maximum in the correlator in roughly the same interval, but only in one of the sub-lattices. This strong staggered dependence is of course a lattice artifact. It should however be noted that for smaller values of μ/T (and thus longer wavelength oscillations, cf. fig. 4.7) there is a clear, broader, minimum in both correlators and on both sub-lattices, which indicates that the effect is not merely a staggered effect, although the maximum which is predicted to follow is completely damped away. All in all, the behavior of the different correlators strongly suggests that there is a complex mass spectrum at the investigated parameter values, and that the prediction in [79] that the phase structure observed in one-dimension has an analogue also in three dimensions is correct.

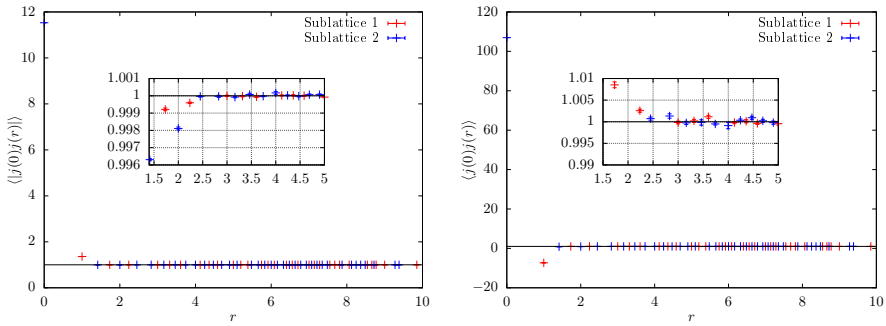

Figure 4.8: The correlator of the absolute value of the junction number (*left panel*) and the correlator of the junction number (*right panel*) for $\beta = 0.08, e^{-M/T} = 0.05$ and $\mu/T = 3.3$ on a 12^3 lattice. The depletion in the left correlator and the enhancement in the right correlator around distance 2 support the proposition that the system behaves as a liquid. However, the strong staggered character still leaves some doubt. In the right panel, the data point at $\sqrt{2}$ and 2 are far below 0.99 and are omitted such that it can be clearly seen that the points at $\sqrt{3}$ and $\sqrt{5}$ are above 1.

For comparison we also measured the junction correlators in two dimensions and also here there is a strong staggered effect, as can be seen in fig. 4.9. In this case the junction-junction correlator in the right panel of fig. 4.9 seems to display a local maximum on both sublattices, but there is a large phase difference between the two, which may be the reason why it is so difficult to observe the local maximum in three dimensions.

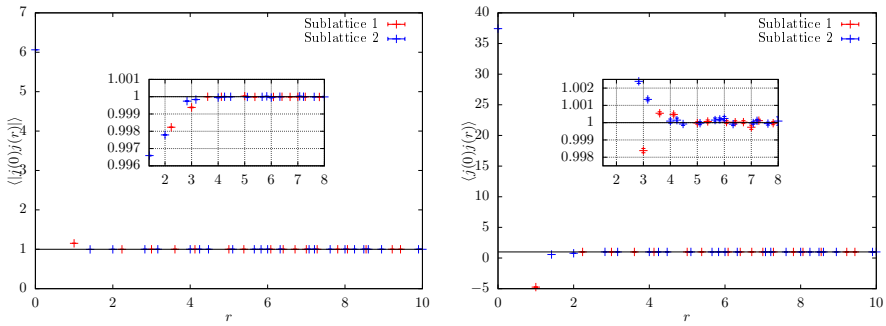

Figure 4.9: The correlator of the absolute value of the junction number (*left panel*) and the correlator of the junction number (*right panel*) for $\beta = 0.26, e^{-M/T} = 0.04$ and $\mu/T = 3$ on a 16^2 lattice. The depletion in the left correlator and the enhancement in the right correlator around distance 2 is similar to what is seen in three dimensions, see fig. 4.8. In this case the correlators on both sublattices shows a maximum in the right panel, but there is a rather large phase difference between the two components.

Finally, we measured some statistics of the flux-tube networks and the junctions. Using the labeling of fig. 4.4 we find that the ratio of C to D junctions is very close to 3/2 and the ratio of B to A junctions is very close to 4, both in full agreement with entropic arguments. The ratio of pure-flux junctions (C&D) to flux-quark junction (A&B) depends on the parameters but for the parameter values we used the flux-quark junctions typically outnumber the pure-flux junctions by a factor 10, reflecting the energy cost of the additional flux tube. In fig. 4.10 we show the histograms of the distribution of the flux-network size, the number of junctions in a network and the network charge for $\beta = 0.08, e^{-M/T} = 0.05$ and $\mu = 2.0$ on a 12^3 lattice.

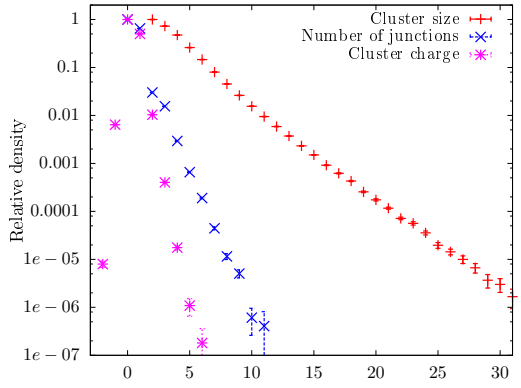

Figure 4.10: Histograms of the distribution of flux-network size, the number of junctions in a network and the network charge for $\beta = 0.08, e^{-M/T} = 0.05$ and $\mu = 2.0$ on a 12^3 lattice.

5

THE HIGGS-YUKAWA MODEL WITH HIGHER DIMENSION OPERATORS VIA EMFT

5.1 INTRODUCTION

In this chapter we exclusively rely on EMFT to study the Higgs and fermion sector of the SM, which is an example of a Higgs-Yukawa model. We will in particular be interested in the EWFT phase transition and how it is affected by higher-dimension operators. The order of this phase transition is crucial for the viability of EW baryogenesis, which demands out-of-equilibrium conditions[1], which can only be satisfied of the transition is first order. The reason EMFT is useful here is because of the substantial cost of simulating the full model with dynamical quarks, which can not even be done at physical parameter values without encountering a sign problem. At the same time the large Yukawa coupling of the top quark and the finite temperature call for a non-perturbative approach.

The content of this chapter has been published in

- Oscar Akerlund and Philippe de Forcrand. „Higgs-Yukawa model with higher dimension operators via extended mean field theory." In: *Phys. Rev. D* 93.3 (2016), p. 035015. arXiv: 1508.07959 [hep-lat].

5.2 HIGGS-YUKAWA MODEL

The Higgs-Yukawa model is a simplified version of the SM Higgs sector where the gauge degrees of freedom are neglected. The components of the model are the scalar complex doublet φ and the fermion doublets Ψ_f. These couple to φ via Yukawa couplings with coupling constants y_f, which also determine the tree level fermion masses $m_f = y_f v$ after symmetry breaking, via the Higgs field expectation value $\langle\varphi\rangle \equiv (0, v)^\intercal$. Since the top quark is orders of magnitude heavier than the other

1 This is only one of the three Sakharov conditions. The other two, Baryon-number and CP-symmetry violating interactions are both present in the SM.

fermions, it is common, and well justified, to restrict the fermion content to solely the top-bottom doublet $\Psi = (t, b)^\intercal = (t_L, t_R, b_L, b_R)^\intercal$. In these fields the Euclidean continuum action is given by

$$S^{\text{cont}}[\overline{\Psi}, \Psi, \varphi] = S_{\text{H}}[\varphi] + S_{\text{F}}[\overline{\Psi}, \Psi, \varphi], \tag{5.1}$$

with

$$S_{\text{H}}[\varphi] = \int \mathrm{d}^4x \, \left\{ \frac{1}{2}|\partial_\mu \varphi|^2 + \frac{1}{2} m_0^2 |\varphi|^2 + \hat{\lambda}|\varphi|^4 \right\}, \tag{5.2}$$

$$S_{\text{F}}[\overline{\Psi}, \Psi, \varphi] = \int \mathrm{d}^4x \, \left\{ \overline{\Psi} \partial\!\!\!/ \Psi + y_b \overline{\Psi}_L \varphi b_R + y_t \overline{\Psi}_L \widetilde{\varphi} t_R + \text{h.c.} \right\}, \tag{5.3}$$

where $\widetilde{\varphi} = i\tau_2 \varphi^\dagger$, τ_2 is the second Pauli matrix and $\Psi_{L/R} = (t_{L/R}, b_{L/R})^\intercal$. The other fermions (quarks and leptons) can, if desired, be added in a completely analogous way.

In this study we will mainly be interested in the broken-symmetry phase and for notational convenience we will exploit the global $SU(2)$ symmetry to make the expectation value of φ real and sit entirely in the lower component of φ, i.e. we parametrize

$$\varphi(x) = \begin{pmatrix} g_2(x) + i g_1(x) \\ v + h(x) - i g_3(x) \end{pmatrix}, \quad \langle \varphi \rangle = \begin{pmatrix} 0 \\ v \end{pmatrix}, \tag{5.4}$$

where $v + h(x)$ is the Higgs field and $g_i(x)$ are the three Nambu-Goldstone modes.

For the Higgs self-interaction we will consider higher dimension operators, in addition to the renormalizable ϕ^4 interaction. The simplest extension is to add a dimension six contact term with six Higgs fields, $(\varphi^\dagger \varphi)^3$, as studied by FRG in [44], but operators of any dimension could just as well be included. Let us for now simply group these higher order terms in a "new physics", or BSM, action [2]

$$S_{\text{NP}}[\varphi] = \sum_{d=6}^{d_{\max}} \sum_{i=1}^{n_d} C_{i,d} \frac{\mathcal{O}_d^i}{M_{\text{BSM}}^{d-4}}, \tag{5.5}$$

where $\mathcal{O}_d^i$ is an operator of mass dimension d, n_d is the number of operators with dimension d, $C_{i,d}$ are the Wilson coefficients and M_{BSM} is the energy scale of the new physics, typically the mass of the lightest mediator particle. Apart from φ^6 there is a second operator of dimension six,

2 We consider here only operators in the pure Higgs sector, for a complete list of dimension 6 operators see [58]

$\mathcal{O}_6^2 = |\partial_\mu \varphi^\dagger \varphi|^2$, but it can be neglected if one assumes an approximate custodial symmetry [89]. Also, if included, the zero-temperature phase transition will always be first order in the EMFT approximation. Naturally (naively), at low energy E, the effects of the higher-dimension operators are suppressed by factors $(E/M_{\text{BSM}})^{d-4}$.

5.3 DIAGONALIZING THE OVERLAP OPERATOR FOR ARBITRARY CONSTANT HIGGS FIELD

To efficiently, albeit approximately, integrate out the fermions we consider the Higgs field to be very slowly varying in space-time. Since we are primarily interested in the infrared properties of the model this assumption is reasonable. We thus assume that the fermions see a constant Higgs field, therefore the fermionic interaction can be diagonalized by going to Fourier space and the fermion determinant can be calculated without much effort.

Due to the global $SU(2)$ invariance, the fermion determinant can only depend on the magnitude of the Higgs field, $|\varphi|^2 = (v+h)^2 + g_1^2 + g_2^2 + g_3^2$. Note that it depends on all the fields in φ and not only on the expectation value. To simplify the derivation we apply an $SU(2)$ transformation such that $\varphi = (0, |\varphi|)^\intercal$. Then, the different fermion flavors decouple and we have

$$S_{\text{F}} = \sum_f N_{c,f} \int \mathrm{d}^4x \, \bar{f} M_f f, \quad M_f \equiv \partial\!\!\!/ + y_f |\varphi| \boldsymbol{I}_4, \tag{5.6}$$

where $N_{c,f}$ is the number of colors for each fermion f, i.e. one for the leptons and three for the quarks. Unless otherwise specified, we will include all SM fermions except the neutrinos with their Yukawa couplings set via the tree level relation $y_f = m_f/v$.

For the model to be a realistic approximation of the SM Higgs sector it is important that the fermions be chiral. This is ensured by implementing the Neuberger overlap operator [77] when putting the fermions on the lattice. The overlap operator $D^{(\text{ov})}$ satisfies an exact lattice chiral symmetry which approaches the usual chiral symmetry in the continuum limit $a \to 0$, a being the lattice spacing. Since we work with an effective model with a finite cut-off, this term will never completely go

away, but as long as the cut-off is well above the top mass the effects should be small. The overlap operator is given by

$$D^{(\mathrm{ov})} = \frac{\rho}{a}\left(\boldsymbol{I}_4 + \frac{A}{\sqrt{A^\dagger A}}\right),\ A = D^{(\mathrm{W})} - \frac{\rho}{a},\ 0 < \rho \leq 2r, \tag{5.7}$$

where $D^{(\mathrm{W})}$ is the usual Wilson operator with negative bare mass M_0 and Wilson parameter r, and ρ is a dimension-less parameter. In our calculations we will adopt the common choices of $r = 1/2$, $\rho = 1$. The lattice action is constructed by the following replacements:

$$\not{\partial} \to D^{(\mathrm{ov})},\ \bar{f}_{L,R} f_{R,L} = \bar{f} P_{R,L} \hat{P}_{R,L} f, \tag{5.8}$$

$$\hat{P}_{R,L} = \frac{\boldsymbol{I}_4 \pm \gamma_5(\boldsymbol{I}_4 - \rho^{-1} D^{(\mathrm{ov})})}{2} = P_{R,L} \mp \frac{\gamma_5}{2\rho} D^{(\mathrm{ov})}, \tag{5.9}$$

after which the fermion operator, eq. (5.6), becomes

$$M_f^{(\mathrm{ov})} = D^{(\mathrm{ov})} + y_f|\varphi|\left(\boldsymbol{I}_4 - \frac{1}{2\rho} D^{(\mathrm{ov})}\right). \tag{5.10}$$

In order to determine the fermion contribution to the action we will have to calculate the determinant, or equivalently the trace log, of this operator. This is most convenient in Fourier space where $D^{(\mathrm{ov})}$ is diagonal. For a given 4-momentum p, its four eigenvalues come as complex conjugate pairs $\nu(p), \nu^\dagger(p)$, each with multiplicity two, where

$$\nu(p) = \rho\left(1 + \frac{i\sqrt{\tilde{p}^2} + \frac{r}{2}\hat{p}^2 - \rho}{\sqrt{\tilde{p}^2 + \left(\frac{r}{2}\hat{p}^2 - \rho\right)^2}}\right), \tag{5.11}$$

$$\tilde{p}^2 = \sum_\mu \sin^2(p_\mu),\ \hat{p}^2 = 4\sum_\mu \sin^2\left(\frac{p_\mu}{2}\right). \tag{5.12}$$

Since the "mass term" $y_f|\varphi|$ is real, the determinant of $M_f^{(\mathrm{ov})}$ is real as well and the trace log takes the form of a real integral

$$\mathrm{TrLog}\left(M_f^{(\mathrm{ov})}\right) = 2\int \frac{\mathrm{d}^4 p}{(2\pi)^4} \log|\nu(p) + y_f|\varphi|\left(1 - \frac{\nu(p)}{2\rho}\right)|^2, \tag{5.13}$$

which can be calculated quite efficiently. Actually, since it only depends on one variable, $y_f|\varphi|$, and will have to be evaluated very often, it will prove advantageous to precalculate it on a discrete set of values and interpolate to intermediate points. In summary, to a first approximation

the effect of the fermions is the addition of an $SU(2)$ symmetric contact term to the Higgs potential.

It should be noted that the determinant is only positive for generic Yukawa couplings in the approximation that the Higgs field is constant. Otherwise the Higgs field will fluctuate in the complex plane and introduce a sign problem, unless the fermions in each doublet have degenerate Yukawa couplings.

5.4 THE EFFECTIVE ACTION AND EMFT SOLUTION

For definiteness we will consider only the $|\phi|^6$ term in S_{NP}, eq. (5.5). Since we have no handle on the Wilson coefficient $C_{1,6}$ of this term we will set it to 1 and introduce $\lambda_6 \equiv (aM_{\text{BSM}})^{-2}$ where a is the lattice spacing. With the approximate treatment of the fermions above, we end up with the lattice action

$$S[\varphi] = \sum_x \Bigg\{ -\kappa \sum_\mu \varphi_x^\dagger \varphi_{x+\hat{\mu}} + \text{h.c.} + |\varphi_x|^2 + \hat{\lambda}\left(|\varphi_x|^2 - 1\right)^2 + \sum_f N_{c,f} \text{TrLog}\left(M_f(y_f\sqrt{2\kappa}|\varphi_0|)\right) + \hat{\lambda}_6 |\phi|^6 \Bigg\}, \quad (5.14)$$

in terms of the conventional φ^4 parameters

$$a\varphi(x) = \sqrt{2\kappa}\varphi_x, \;\; (am_0)^2 = \frac{1-2\hat{\lambda}}{\kappa} - 8 \qquad \hat{\lambda} = 4\kappa^2\lambda, \;\; \hat{\lambda}_6 = 8\kappa^3\lambda_6. \quad (5.15)$$

This action is quite similar to the complex φ^4 model in chapter 3 and we can adopt the vector notation used there,

$$\mathbf{\Phi}_x^\intercal = (h_x, g_{1,x}, g_{2,x}, g_{3,x})^\intercal + (\hat{v}, 0, 0, 0)^\intercal \equiv \boldsymbol{\delta\Phi}_x^\intercal + \langle \mathbf{\Phi} \rangle^\intercal, \quad (5.16)$$

with $\hat{v} = av/\sqrt{2\kappa}$, to derive the EMFT equations in an analogous fashion. Concentrating on the field at the origin, $\mathbf{\Phi}_0$, the hopping part of the action can be expressed as

$$\Delta S = -2\kappa \sum_{\pm\mu} \boldsymbol{\delta\Phi}_0^\intercal \boldsymbol{\delta\Phi}_{\hat{\mu}} - 4d\kappa\hat{v}h_0. \quad (5.17)$$

The lattice without the origin is considered an external bath and will be self-consistently integrated out. This is equivalent to replacing the

nearest-neighbor interaction term in eq. (5.17) by its cumulant expansion with respect to the external bath. Truncating the expansion at second order we obtain the following effective action:

$$\begin{aligned} S_{\text{EMFT}} = \boldsymbol{\Phi}^{\intercal}(\boldsymbol{I}-\boldsymbol{\Delta})\boldsymbol{\Phi} + \hat{\lambda}\left(\|\boldsymbol{\Phi}\|^2-1\right)^2 \\ + \sum_f N_{c,f}\,\text{TrLog}\left(M_f^{(\text{ov})}\left(y_f\sqrt{2\kappa}\|\boldsymbol{\Phi}\|\right)\right) \\ - 2\hat{v}(\hat{v}+h)(2d\kappa-\Delta_1) + \hat{\lambda}_6\|\boldsymbol{\Phi}\|^3, \end{aligned} \tag{5.18}$$

where $\boldsymbol{\Delta}$ emulates propagation in the external bath. A closer inspection of the cumulant expansion reveals

$$\begin{aligned} \boldsymbol{\Delta} &= 2\kappa^2 \sum_{\pm\mu,\rho} \left\langle \delta\boldsymbol{\Phi}_\mu \delta\boldsymbol{\Phi}_\rho^{\intercal}\right\rangle_{\text{ext}} \\ &= 2\kappa^2 \sum_{\pm\mu,\rho} \text{diag}\left\langle \left(h_\mu h_\rho, g_{1,\mu}g_{1,\rho}, g_{2,\mu}g_{2,\rho}, g_{3,\mu}g_{3,\rho}\right)\right\rangle_{\text{ext}} \\ &\equiv \text{diag}(\Delta_1,\Delta_2,\Delta_2,\Delta_2), \end{aligned} \tag{5.19}$$

where the diagonal form follows from the symmetries of the action. Since the action is still symmetric with respect to $O(3)$ rotations of g_1, g_2, g_3 it is practical to rewrite the action in terms of two variables

$$(\hat{v}+h_0) = \phi_h, \tag{5.20}$$

$$\sqrt{g_{1,0}^2+g_{2,0}^2+g_{3,0}^2} = \phi_g, \tag{5.21}$$

in which $\Delta = \text{diag}(\Delta_1,\Delta_2)$ and $\left\langle g_{i,0}^2\right\rangle = \left\langle \phi_g^2\right\rangle/3$. The EMFT action is then given by

$$\begin{aligned} S_{\text{EMFT}} = (1-\Delta_1)\phi_h^2 + (1-\Delta_2)\phi_g^2 + \hat{\lambda}\left(\phi_h^2+\phi_g^2-1\right)^2 \\ + \sum_f N_{c,f}\,\text{TrLog}\left(M_f^{(\text{ov})}\left(y_f\sqrt{2\kappa}\sqrt{\phi_h^2+\phi_g^2}\right)\right) \\ - 2\hat{v}\phi_h(2d\kappa-\Delta_1) + \hat{\lambda_6}\left(\phi_h^2+\phi_g^2\right)^3, \end{aligned} \tag{5.22}$$

and the partition function becomes

$$Z_{\text{EMFT}} = \mathcal{N}\int \mathrm{d}\phi_h \mathrm{d}\phi_g\, \phi_g^2 \exp\left(-S_{\text{EMFT}}\right), \tag{5.23}$$

where $\mathcal{N}$ is an irrelevant normalization constant. The unknown parameters v and $\mathbf{\Delta}$ can then self-consistently be determined via the three self-consistency equations

$$\langle \phi_h \rangle = \hat{v}, \tag{5.24}$$

$$2\left\langle \phi_h^2 \right\rangle_c = \int \frac{\mathrm{d}^4 p}{(2\pi)^4} \frac{1}{\frac{1}{2\left\langle \phi_h^2 \right\rangle_c} + \Delta_1 - 2\kappa Z_h \sum_\mu \cos(p_\mu)}, \tag{5.25}$$

$$\frac{2\left\langle \phi_g^2 \right\rangle}{3} = \int \frac{\mathrm{d}^4 p}{(2\pi)^4} \frac{1}{\frac{3}{2\left\langle \phi_g^2 \right\rangle} + \Delta_2 - 2\kappa Z_h \sum_\mu \cos(p_\mu)}, \tag{5.26}$$

where $\left\langle \phi_h^2 \right\rangle_c = \left\langle \phi_h^2 \right\rangle - \langle \phi_h \rangle^2$ and the wave function renormalization Z_h is chosen such that the Nambu-Goldstone bosons are exactly massless, see section 3.4.4. The last two equations enforce that the connected 2-point function, from the origin to the origin, is equal to its momentum-space expression. The four- (or d-) dimensional integrals can be transformed into one-dimensional integrals by using the identity

$$\int \frac{\mathrm{d}^d p}{(2\pi)^d} \frac{1}{a - \sum_\mu \cos(p_\mu)} = \int_0^\infty \mathrm{d}\tau e^{-a\tau} \left(I_0(\tau)\right)^d, \tag{5.27}$$

where $I_0(x)$ is a modified Bessel function of the first kind. See section 2.4.1 for more details.

5.4.1 *Scale setting and observables*

In order to examine the effect of different cut-offs and possible higher dimension operators on the Higgs boson mass we need to set the scale of the lattice calculations. This is most naturally done by fixing the Higgs field expectation value v to its phenomenological value. In terms of lattice variables we have

$$v = \frac{\sqrt{2\kappa}\hat{v}}{a} = 246\,\mathrm{GeV}, \tag{5.28}$$

which, given $\hat{v}$, determines the value of the cut-off $\Lambda = 1/a$. Furthermore, we want to use physical quark masses, so we fix the Yukawa couplings using the tree level relation $m_f = y_f v$. We can now determine the Higgs boson mass M_h in GeV as a function of the parameters

of the Higgs potential by evaluating the inverse propagator at zero momentum:

$$\begin{aligned} G_h^{-1}(p) &= \frac{1}{2\left\langle \phi_h^2 \right\rangle_c} + \Delta_1 - 2\kappa Z_h \sum_\mu \cos(p_\mu) \\ &\underset{p\to 0}{\to} \kappa Z_h((aM_h)^2 + (ap)^2), \\ \Rightarrow M_h^2 &= \left(\frac{1}{2\left\langle \phi_h^2 \right\rangle_c} + \Delta_1 - 8\kappa Z_h \right) \frac{\Lambda^2}{\kappa Z_h}. \end{aligned} \tag{5.29}$$

5.5 RESULTS

In order to assess how well our EMFT method works in the presence of fermions, we compare it to already existing full Monte Carlo results and results obtained using an analytic, approximate method, the Contraint Effective Potential (CEP) [36]. In fig. 5.1 we show the Higgs expectation value in lattice units $\hat{v}$ as a function of the hopping parameter κ at two different values of the new coupling, $\lambda_6 = 0.1$ in the upper panel and $\lambda_6 = 1.0$ in the lower one. Each color represents a different value of the quartic coupling λ. In this comparison only the top and bottom quarks are included with degenerate Yukawa couplings $y_b = y_t = 175/246$ and color factors $N_{c,b} = N_{c,t} = 1$. It is clear that EMFT (solid lines) is a very good approximation and gives results close to the Monte Carlo results (symbols) in all cases, in contrast to CEP (dotted lines) which works acceptably well for small values of λ_6 only. This is not surprising since the CEP calculations in [60] are perturbative, whereas EMFT is fully non-perturbative.

It is quite remarkable that EMFT reproduces the expectation value to such a high accuracy. This was of course observed already in chapter 3, where the complex ϕ^4 theory was studied. The main reason for the success is probably the way EMFT deals with the mass renormalization and the fact that close to a Gaussian fixed point, a mass renormalization is in principle all that is needed to accurately describe the model. However, EMFT works well also in an extended region away from the fixed point, even where there is a strong first order transition, as can be seen in fig. 5.1.

For our actual results we will adopt a slightly different point of view on the model than the authors of [36]. Indeed, consider the origin of the higher dimension operators. Generically they stem from UV completion

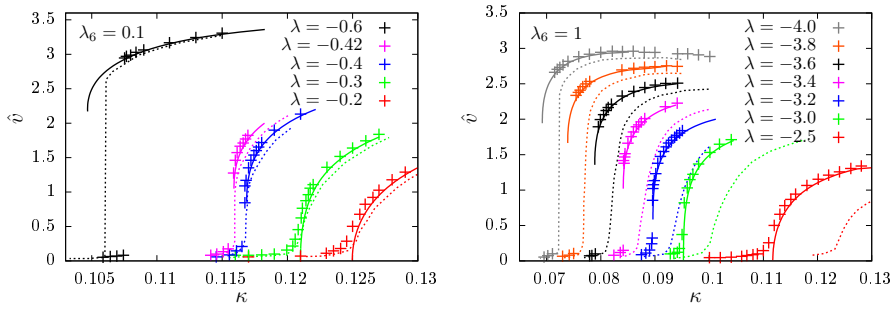

Figure 5.1: The Higgs vacuum expectation value in lattice units as a function of the coupling κ at various λ, for $\lambda_6 = 0.1$ (*left panel*) and $\lambda_6 = 1$ (*right panel*). The solid lines are EMFT calculations from this work and the pluses and dashed lines are full Monte Carlo simulations and CEP calculations respectively, both taken from [60]. The EMFT results follow the Monte Carlo data closely for both values of λ_6, whereas the CEP calculation gives reasonably accurate results for the upper, perturbative value only.

of the SM and are thus associated with an energy scale which is typically the mass of the lightest of the "new" particles which couple to the Higgs field. Let us call this energy scale M_{BSM}. It is natural to assume that the coupling of this particle to the Higgs field is of order one, such that the coefficient in front of the $|\phi|^6$ operator will be M_{BSM}^{-2} with the corresponding dimensionless coupling $\lambda_6 = (aM_{\text{BSM}})^{-2}$. Notice, moreover, that $\Lambda = a^{-1}$, not M_{BSM}, is the cutoff of the effective model, since it is directly related to the maximum energy scale probed by the lattice action. In order to justify the effective treatment of particles heavier than M_{BSM} the cutoff Λ has to be sufficiently small. This leads to a hierarchy of scales condition, $aM_h \ll 1 \lesssim aM_{\text{BSM}}$, which in turn means $\lambda_6 \lesssim 1$ in the broken symmetry phase. As (aM_{BSM}) is decreased towards 1, more and more terms in the effective action would have to be taken into account in order to maintain a good approximation of the underlying model.

It is quite challenging to preserve a good separation of scales while at the same time keeping the physical volume large, and hence any lattice simulation is susceptible to large finite size effects. This is particularly true in a theory with massless modes, like the one we

study here. In EMFT one generally works directly in the thermodynamic limit but in order to demonstrate the power law corrections coming from the Nambu-Goldstone modes, we have solved the self-consistency equations in a finite volume. In fig. 5.2 we show the relative error on the Higgs mass as a function of the box size. The scale separation factor is $aM_{\mathrm{BSM}} = \sqrt{10}$ ($\lambda_6 = 0.1$) for all values of a and we have marked both where the size of the correction is 50% of the mass itself and where an $N_s = 32$ lattice would be for two different lattice spacings. This demonstrates the need for very big lattices before one can even see the asymptotic power law scaling.

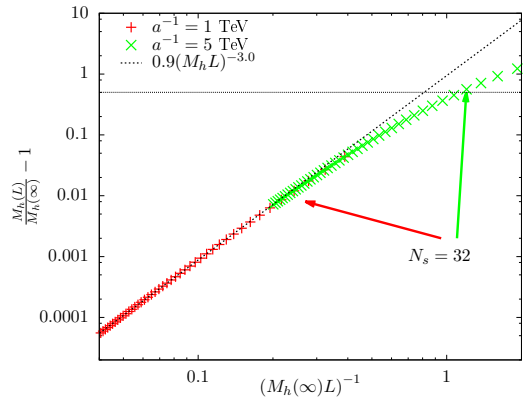

Figure 5.2: Finite volume relative correction to the Higgs mass for two different lattice spacings calculated with EMFT with $\lambda_6 = 1/10$ and $M_h = \xi^{-1} = 125$ GeV. The horizontal line corresponds to a 50% correction. In order to see the asymptotic $(\xi/L)^3$ corrections due to the massless Nambu-Goldstone modes, rather large lattices are needed, which poses a challenge to full Monte Carlo simulations. In EMFT one can avoid the problem of thermodynamic extrapolation entirely by working directly in the thermodynamic limit.

5.5.1 *The zero-temperature phase diagram*

It is most convenient to present the phase diagram in the (unphysical) bare parameters κ, λ and λ_6. One can then pass to physical units via the Higgs expectation value in the broken phase. In fig. 5.1 one can see that the transition turns from second- to first-order as λ is made more

negative and in fig. 5.3 we show how the tricritical point depends on λ_6. For λ below the line the κ-driven transition is first order and above it is second order [3]. Next, we fix λ_6 and look at the transition in the (λ, κ)-plane. An example, where $\lambda_6 = 1/4$, can be seen in fig. 5.4. The color of the line denotes the order of the transition, blue for second order and red for first order. The star marks the tricritical point and the arrow denotes how it moves as the number of lattice sites in the temporal direction N_t is decreased (see below for more details). The location of the tricritical point is obtained by fitting the critical vev on the first-order side with a power law $\langle \phi \rangle_c (\lambda) = c\,(\lambda_c - \lambda)^b$. There is a region close to the second-order line where one can perform calculations at a small lattice spacing a and since it is not possible to take the continuum limit of this effective theory anyway, it may also be viable to stay close to the transition on the first-order side. In fact, it turns out that a first order finite temperature transition will be found only there, denoted by the gray shaded area in the figure.

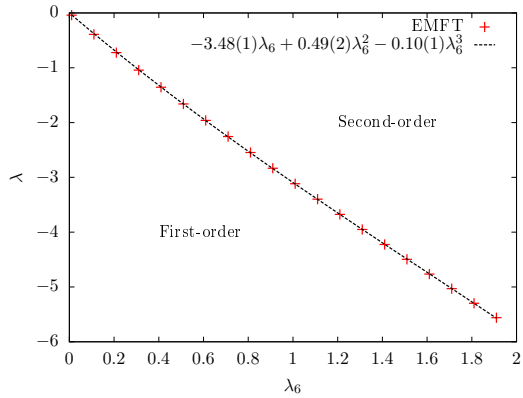

Figure 5.3: The tricritical point at zero temperature. For λ below the line the transition is first order and above it is second order.

5.5.2 *Higgs mass lower bound*

Given a specific form of the Higgs potential, the lower bound on the Higgs mass is simply given by the minimal mass obtainable in the given

3 In the absence of gauge fields there is always a symmetric phase and a broken phase separated by a phase transition, never a crossover

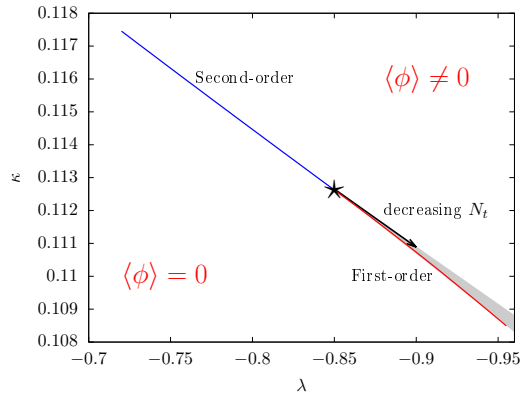

Figure 5.4: Zero- and finite-temperature transition in the (λ, κ)-plane at fixed $\lambda_6 = 1/4$. The transition turns from second to first order at the first-order endpoint marked by the star. The color of the line denotes the order of the transition, blue for second order and red for first order. As the lattice size is reduced in the temporal direction the endpoint moves along the arrow, and thus the gray shaded area marks the region in the plane where the finite temperature transition is first order.

parameter space of the potential [4]. For a pure φ^4 potential it is found that the Higgs mass decreases when λ decreases and the lower bound is thus obtained at vanishing quartic coupling. In the Higgs-Yukawa model, this lower bound turns out to be just above 40 GeV and a positive λ is needed to bring the Higgs mass up to 125 GeV. A negative coupling is obviously prohibited by the requirement of a bounded action. By introducing higher dimension operators, we can have a stable vacuum even at negative quartic coupling, and it is plausible that this could lead to an even lower Higgs mass. This was first demonstrated in [55], using the FRG on a chiral $\mathbb{Z}_2$ Higgs-Yukawa model. Analogous results were also obtained using the Higgs-Yukawa model described above at physical values of the top and bottom masses in [56] and using the chiral $\mathbb{Z}_2$ Higgs-Yukawa model plus an $SU(3)$ gauge sector in [44]. Later, the authors of [36] came to similar conclusions using nonperturbative Monte Carlo simulations and perturbative CEP calculations of the above described Higgs-Yukawa model with mass-degenerate top and bottom masses. Common to all these studies is that they add a ϕ^6 operator to the Higgs potential and when its coupling constant λ_6 is positive, the Higgs mass can be further reduced by making the quartic coupling λ more and more negative. At some point, in the lattice regularized models, the phase transition between the symmetric and broken phases turns first order (see fig. 5.3) and there is a hard lower bound on the lattice spacing a. Since the model is only effective this is in itself not a problem, but, since one wants $aM_h \ll 1$, it bounds the region in parameter space where simulations are useful.

Typically one finds that the Higgs mass goes to zero as one approaches the tricritical point from the second-order side although before zero is obtained one runs into subtle issues regarding new local minima of the effective action [5]. This means that the Higgs mass can in general be lowered by a large if not arbitrary amount, from its lower bound in the $\lambda_6 = 0$ case. This is demonstrated in fig. 5.5, where the Higgs mass M_h is plotted as a function of aM_h for a few different values of aM_{BSM} and λ, together with the SM lower bound obtained at $\lambda = 0$. As λ is made more negative one approaches the regime of first-order transition

4 Note that the effective potential can feature local minima, which may have a smaller curvature than the global one. We are not interested in those.

5 This scenario is however quite tricky to study in an effective model setup since the higher field value at the new minimum reduces the separation of the dynamical and the cut-off scales which might make the effective model less precise

and the Higgs mass decreases and can take values well below the SM lower bound.

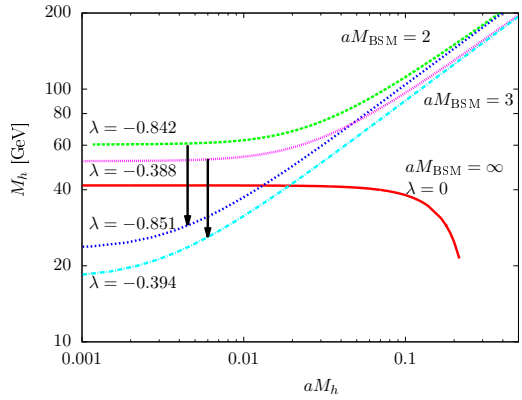

Figure 5.5: The Higgs mass M_h as a function of aM_h for various combinations of $aM_{\rm BSM}$ and λ, together with the SM lower bound on the Higgs mass obtained at $M_{\rm BSM} = \infty$ and $\lambda = 0$. In the presence of a ϕ^6 operator a negative value of λ is allowed and the Higgs mass can be lowered well below the SM bound, as indicated by the arrows.

All in all it is clear that in the presence of higher dimension operators the lower bound on the Higgs mass loses its meaning. In fact, one may argue that this is a null statement since the lower bound was calculated under the assumption that there is only the SM, and clearly new operators will change the running of the couplings.

5.5.3 *Finite temperature*

Let us now turn to the $M_{\rm BSM}$ dependence of the finite temperature transition. In gauge-Higgs systems it has been demonstrated that introducing a φ^6 operator makes the phase transition stronger [57, 91, 92], which in turn means that the critical mass, up to which the transition is first order, increases. If it would increase past the observed Higgs boson mass, electroweak baryogenesis might become possible again. Here, we present our findings using EMFT. Still in the infinite volume limit, we can introduce a non-zero temperature $T = 1/(aN_t)$ by using a finite number N_t of lattice points in the temporal direction. This gives us control over the temperature in discrete steps (for a fixed

lattice spacing), so in order to get a good resolution one would need to work with rather fine lattices. However, this limits the range of available M_{BSM} because of the condition of scale separation $aM_{\text{BSM}} \gtrsim 1$. To overcome this problem we will determine the linear response of the system and then extrapolate to the desired temperature. Alternatively, to continuously vary the temperature, one could use a lattice action with anisotropic couplings.

The observables of main interest are the critical Higgs mass for which the transition turns first order and the critical temperature. Another interesting observable is the Higgs mass for which the vev at the transition is of the same order as the critical temperature, which is the actual condition for a viable EW baryogenesis. All observables depend on both M_{BSM} and the lattice spacing a so we need to calculate them in a two dimensional parameter space. The starting point for determining this dependence is to obtain the phase diagram as in fig. 5.4 for various aM_{BSM} and N_t values, and then to determine how the first-order endpoint moves as a function of N_t. This is illustrated by the star and the arrow in fig. 5.4. The finite temperature transition will be first order in the region between the $T = 0$ first-order line and the trajectory of the first-order endpoint, denoted by the shaded region in fig. 5.4. We find that the endpoint moves on a straight line in the (κ, λ)-plane, as can be seen in fig. 5.6 for $\lambda_6 = 1/4$. By determining the lattice spacing a and the Higgs mass M_h at zero temperature along this line we can obtain the critical Higgs mass as a function of the BSM scale, shown in fig. 5.7. In fig. 5.8 we show how the critical Higgs mass for $\lambda_6 = 1/4$ changes for different strengths of the first order transition, measured in terms of ϕ_c/T_c where ϕ_c is the critical Higgs expectation value at the phase transition. In both of these figures the color of the line gives the critical temperature T_c in GeV.

Since our model is an effective one, we do not expect that the resulting curve is independent of the lattice spacing. Indeed, in the range of $2 \leq aM_{\text{BSM}} \leq 4$ we find that the critical Higgs mass varies by about ten percent. This is in itself not a direct measure of the systematic uncertainties of the study since the choice of only including the φ^6 operator introduces uncertainties which are hard to quantify, especially at the lower end of the interval. Moreover, different implementations of a UV cutoff will give somewhat different results. With there caveats, the variation of the critical line in the (M_h, M_{BSM})-plane gives a measure of the uncertainties within the model itself. The final result is that

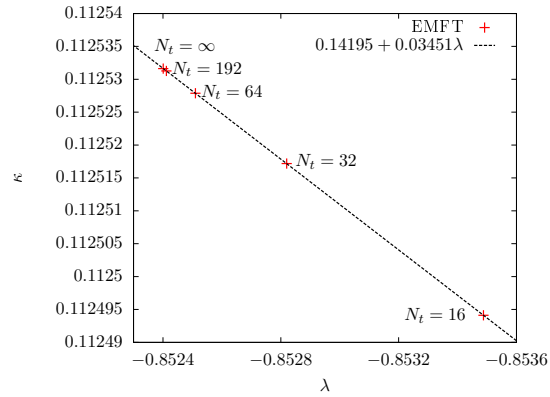

Figure 5.6: The N_t dependence of the tricritical point for $\lambda_6 = 1/4$. The trajectory is very well described by a straight line.

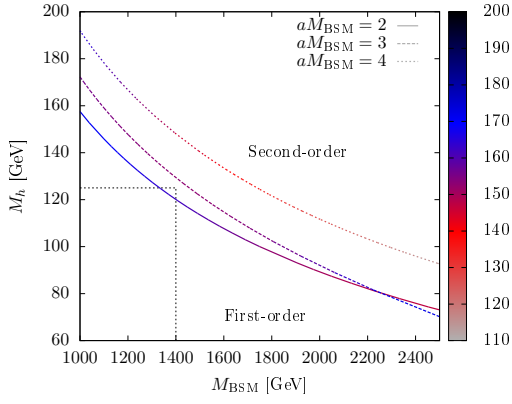

Figure 5.7: The critical Higgs mass below which the finite temperature transition is first order for various values of aM_{BSM}. The color coding gives the transition temperature in GeV. The 3 curves give a measure of the sensitivity of our effective theory to the cutoff. A higher cutoff makes the transition weaker.

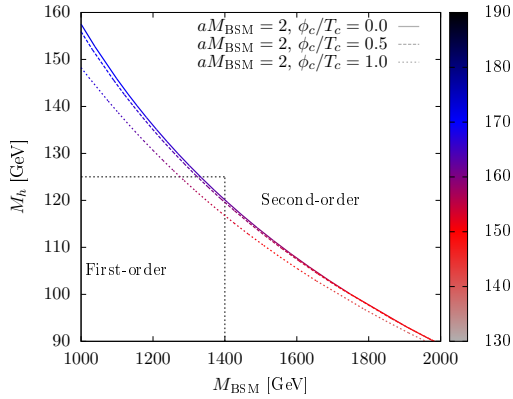

Figure 5.8: The critical Higgs mass below which the finite temperature transition is first order for $aM_{\rm BSM} = 2$ and different strengths of the transition measured in terms of ϕ_c/T_c where ϕ_c is the critical Higgs vev at the transition. The color coding gives the transition temperature in GeV.

for a Higgs mass of 125 GeV a BSM scale of around 1.5 TeV is needed to make the EW finite temperature phase transition first order, and this result changes only slightly even if we demand that the transition should be strongly first order with $\phi_c/T_c \gtrsim 1$. This result is interesting since in many supersymmetric extensions of the SM one expects to find the lightest superpartners around this mass scale. The final scale separations ($aM_h \ll 1 \ll aM_{\rm BSM}$) at the tricritical point for the different values of $aM_{\rm BSM}$ are listed in table 5.1 and it is evident that the validity of the effective model is somewhat strained, but not completely spoiled, due to the rather small separations.

Table 5.1: Separations of three scales in units of the inverse lattice spacing at the tricritical point for different values of $aM_{\rm BSM}$.

$M_{\rm BSM}$	a^{-1}	M_h
2	1	0.19
3	1	0.26
4	1	0.29

Finally, to quantify the influence of our nonperturbative treatment of the fermions we repeated the calculations considering just the Higgs sector and found that, after all, the fermions contribute only percent-

level corrections to the purely bosonic case, see fig. 5.9. Remarkably, the sign of the correction depends on the value of aM_{BSM}. We also note that the BSM scale of ≈ 1.5 TeV needed for a first-order finite-temperature transition is in good agreement with what one obtains in the gauge-Higgs model with a ϕ^6-term [91, 92]. This could be used as an argument for leaving out the SM fermions and gauge fields from the simulations while studying higher dimension operators in the context of EW baryogenesis, and for including them perturbatively only.

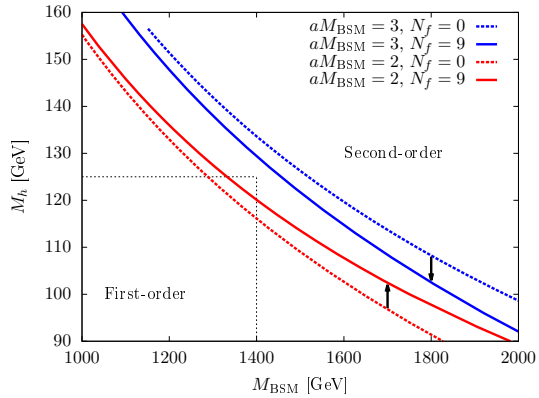

Figure 5.9: The critical Higgs mass below which the finite temperature transition is first order for various values of aM_{BSM} with and without the SM fermions. The correction due to the fermions (shown by the arrows) is small and of indefinite sign.

6

GAUGE-INVARIANT SIGNATURES OF SPONTANEOUS GAUGE-SYMMETRY BREAKING BY THE HOSOTANI MECHANISM

6.1 INTRODUCTION

In this chapter we study the possibility of spontaneous gauge-symmetry breaking and how to detect it in a reliable way. Although Elitzur's theorem forbids the spontaneous breaking of gauge symmetries, there are a few ways to circumvent it, one being the Higgs mechanism. Another related possibility arises if one or more dimensions are compact. Then, non-contractible loops of gauge fields *à la* Aharonov-Bohm can form and acquire nonzero expectation values, which in turn breaks the gauge symmetry. This leads to the concept of gauge-Higgs unification and the Hosotani mechanism [62, 63], where a component of the gauge field in a compact extra dimension plays the role of the Higgs field and thus mimics the Higgs mechanism. Here we investigate this possibility in the nonperturbative framework of the lattice and show how to detect this breaking, without fixing the gauge.

The content of this chapter has been published in

- Oscar Akerlund and Philippe de Forcrand. „Gauge-invariant signatures of spontaneous gauge symmetry breaking by the Hosotani mechanism." In: *PoS* LATTICE2014 (2015), p. 272. arXiv: 1503.00429 [hep-lat].

6.2 THE HOSOTANI MECHANISM

Hosotani originally considered an $SU(3)$ gauge theory with adjoint fermion fields in $(4+1)$ dimensions. The fifth dimension is taken to be compact and he showed that if the matter fields obey periodic boundary conditions in the extra dimension, then the minimum of the perturbative effective potential $V_{\text{eff}}(\operatorname{Tr} P_5)$ can be displaced from the trivial one (fig. 6.1 left) to one of the nontirvial ones depicted in fig. 6.1 middle and right. This is because the adjoint matter fields have an opposite

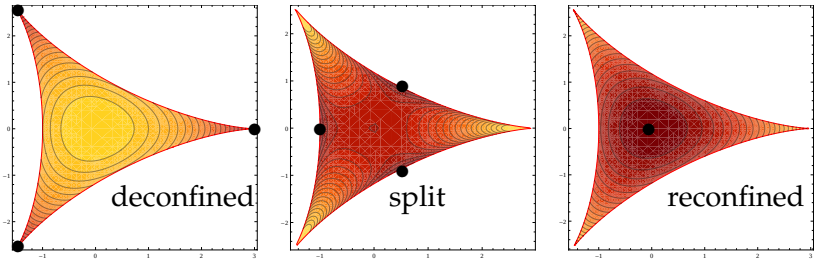

Figure 6.1: Contour lines of the effective potential $V_{\text{eff}}(\text{Tr}P_5)$ in the two independent angles of P_5, resulting from different matter contents and boundary conditions in the extra dimension. Black dots mark the minima in each case.

contribution to V_{eff} than the gauge fields. The three different cases have been dubbed "deconfined", "split" and "reconfined", respectively. The argument does not depend strongly on the number of dimensions and the three phases exist also in $(3+1)$ dimensions, as was found in [39], in a project aimed at understanding center symmetry breaking in QCD(Adj) as proposed by Unsal et al. [97, 68].

To understand the character at each of the minima, it is useful to consider the diagonal form of the $SU(3)$ matrix P_5 which minimizes the potential in the different cases. They are given by

$$\begin{pmatrix} +1 & 0 & 0 \\ 0 & +1 & 0 \\ 0 & 0 & +1 \end{pmatrix} \qquad \text{"deconfined"}, \tag{6.1}$$

$$\left(\begin{array}{cc|c} -1 & 0 & 0 \\ 0 & -1 & 0 \\ \hline 0 & 0 & +1 \end{array}\right) \qquad \text{"split"}, \tag{6.2}$$

$$\left(\begin{array}{cc|c} e^{+i\frac{2\pi}{3}} & 0 & 0 \\ 0 & e^{-i\frac{2\pi}{3}} & 0 \\ \hline 0 & 0 & 1 \end{array}\right) \qquad \text{"reconfined"}. \tag{6.3}$$

The symmetry-breaking pattern of the different minima is now evident. We just have to determine which gauge transformations $P_5 \leftarrow \Omega^\dagger P_5 \Omega$, $\Omega \in SU(3)$ take a minimizing P_5 to another minimizing element. The identity matrix of the "deconfined" phase is invariant under any gauge transformation, so the symmetry group is $SU(3)$. This

is not the case for the other two phases though. In the "split" case, P_5 is left unchanged only if $\Omega \in SU(2) \times U(1)$. In the "reconfined" case, P_5 is left unchanged only if $\Omega = \exp(i\theta_3\lambda_3 + i\theta_8\lambda_8)$, i.e. $\Omega \in U(1) \times U(1)$. So, even if the action is invariant under any $SU(3)$ gauge transformation, the split and reconfined vacua are not and thus it is justified to speak of gauge-symmetry breaking, even though the expectation $\langle A_5 \rangle$ is actually zero due to gauge transformations which permute the eigenvalues of P_5. However, this is analogous to the situation with the ordinary Higgs mechanism: one says that the gauge symmetry "breaks" when the Higgs field "develops an expectation value", although the action remains gauge-invariant and the expectation value $\langle \phi \rangle$ remains exactly zero (in the absence of gauge-fixing).

Nevertheless, the three phases certainly have different long-distance physics. In four dimensions the deconfined phase has eight gluons, the split phase has three gluons and one photon, whereas the reconfined phase has two photons. In the phases with photons, a Coulomb potential between corresponding probe charges will arise. However, the remnant gauge symmetry will "scramble" the corresponding $SU(2)$ and $U(1)$ subgroups differently at each lattice size, and the different physics will be hard to detect.

Take for example the "split" $SU(2) \times U(1)$ phase. Naively one would try to detect the Coulomb potential by looking for a perimeter law in the $SU(3)$ Wilson loops. However, in addition to the $U(1)$ factor, there is also an $SU(2)$ element associated to each link, and those will contribute an area law to the trace of such loops. It is therefore more difficult than naively anticipated to detect the above phenomena by looking at the IR properties of the effective $4d$ theory. One way around this may be to fix the gauge[1], with a gauge condition which minimizes the magnitude of the $SU(3)$ link elements which do not belong to $SU(2) \times U(1)$ or $U(1) \times U(1)$. The latter is the well-known Maximal Abelian gauge. Here, we want to study gauge-invariant observables, and follow a different route.

6.3 GAUGE SYMMETRY BREAKING SEEN IN A GAUGE-INVARIANT WAY

One possibility is to study the gauge-invariant eigenvalues of P_5, and in particular the quadratic fluctuations $m_k^{-2} = \langle (\bar{A_5}^k - \langle \bar{A_5}^k \rangle)^2 \rangle$ of the

1 No signal was found by Jim Hetrick, as presented in [61].

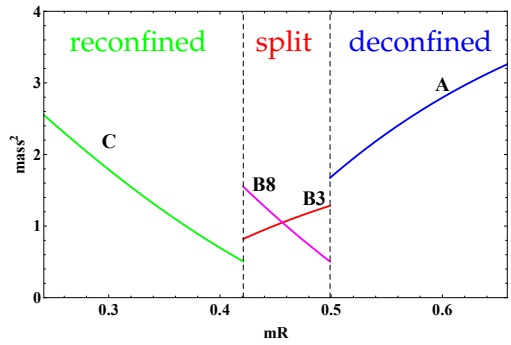

Figure 6.2: Mass squared of the Higgs field, as a function of the size of the extra dimension, for two adjoint fermions. In the split phase, the two Abelian components of the Higgs field have different masses. Perturbative calculation and figure from [40].

static mode $\bar{A}_5$ defined via $P_5 = \exp(igL_5\bar{A}_5{}^k\lambda_k)$. These fluctuations determine the Higgs mass squared. If the gauge symmetry is realized, the mass must must necessarily be the same for all k. Conversely, if there is a k-dependence in the masses, then the symmetry must be broken. The masses can be obtained from Monte Carlo simulations or from an expansion of the effective potential around the minimum of each phase. These analytic results are shown in fig. 6.2 [40]. The fluctuations about the deconfined vacuum is isotropic in color space as expected. The same is true in the reconfined phase, even though the symmetry is supposed to be broken here. The reason for this is that there is a locally enforced $\mathbb{Z}_3$ symmetry in P_5 which protects against a mass splitting. However, in the split phase a mass splitting is indeed observed, the fluctuations of $\bar{A}_5$ in the λ_3 and λ_8 directions are different and consequently $V_{\text{eff}}(\bar{A}_5)$ is elliptical, not spherical, in the split phase. However, this interesting phenomenon is of no relevance to long-distance $4d$ physics, because the Higgs mass is of order $1/L_5$.

6.3.1 *Abelian flux*

We propose to characterize the symmetry-breaking pattern by monitoring the stability of topological excitations which are stable with respect to one of the gauge subgroups, but unstable with respect to the whole

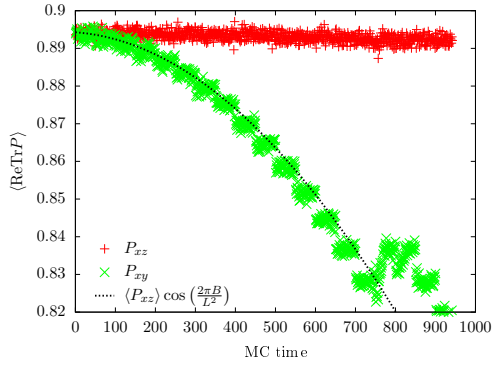

Figure 6.3: Average xy and xz plaquettes in a $U(1)$ system, under the introduction of one unit of xy magnetic flux every 50 sweeps. The dotted line is the leading prediction. Flux states are long-lived and cause a shift of the in-plane plaquette.

gauge group. The simplest example of such an excitation is an Abelian flux through some plane xy, which is only stable with respect to $U(1)$ due to $\Pi_1(U(1)) = \mathbb{Z}$, while $\Pi_1(SU(3)) = \Pi_1(SU(2)) = \mathbf{1}$. The presence of such a flux will affect the expectation value of the gauge-invariant plaquettes, so it is possible to detect the gauge-symmetry breaking without fixing the gauge. Another examples of such topological excitations are monopoles of different kinds.

Let us first give a detailed account of the situation with an xy Abelian flux. For simplicity we consider a $U(1)$ gauge theory on an $L_x \times L_y \times L_z \times L_t$ lattice. A configuration of B units of flux can be prepared by starting from a "cold" configuration $U_\mu(x) = \mathbf{1}\ \forall x, \mu$ and then arranging the links so that each xy plaquette P_{xy} is equal to $\exp(i\frac{2\pi B}{L_x L_y})$. One can then perform usual Monte Carlo updates and monitor the gauge-invariant flux action: $\Delta = \langle \mathrm{Tr} U_{P_{xz}} \rangle - \langle \mathrm{Tr} U_{P_{xy}} \rangle$, where the difference is taken to isolate the effect of the xy flux. Classically, $\Delta = 1 - \cos\frac{2\pi}{L_x L_y} \approx \frac{2\pi^2}{L_x^2 L_y^2}$. The leading effect of fluctuations is to modify P_{xy} and P_{xz} in the same way, so that $\Delta \sim \langle \mathrm{Tr} U_{P_{xz}} \rangle (1 - \cos\frac{2\pi}{L_x L_y} B)$ for B units of flux. This simple prediction is completely consistent with the numerical simulation of fig. 6.3, where B is incremented every 50 Monte Carlo sweeps. Flux states are extremely stable, since for their decay one xy plaquette in each plane must go through angle π. This only happens at the right edge of the figure.

The situation in the case of $SU(3)$ gauge-symmetry breaking is very similar to the above description. The starting "cold" configuration will be one that minimizes the total lattice action, which for the split and reconfined phases is different from the trivial configuration. Nevertheless, a xy flux can be introduced in some specific $U(1)$ subgroup in an analogous fashion and then ordinary updates of the full $SU(3)$ gauge links can be performed with respect to an action which is expected to induce gauge-symmetry breaking. A simpler and computationally much cheaper alternative to dynamical adjoint fermions is to apply an external potential $h_F \mathrm{ReTr} P_5 + h_A |\mathrm{Tr} P_5|^2$, as was originally done in [75].

As previously mentioned, under the action of the full $SU(3)$ symmetry, the subgroup in which the flux was introduced is locally scrambled and in order to unscramble it, one would be required to fix the gauge. However, it is actually not necessary to gauge-fix in order to ascertain whether the $U(1)$ flux is still there, it is sufficient to monitor the gauge-invariant excess action in the xy planes, namely $\Delta = \langle \mathrm{Tr} U_{P_{xz}} \rangle - \langle \mathrm{Tr} U_{P_{xy}} \rangle$, just like in the pure $U(1)$ case.

Figure 6.4 shows the results of such an experiment in the reconfined phase ($SU(3) \to U(1) \times U(1)$). On the y-axis, Δ has been normalized to its value in the pure $U(1)$ case. Interestingly, the excess action depends on the $U(1)$ subgroup where the flux is introduced. The reason is the following. In all cases, a $U(1)$ angle $\theta = \frac{2\pi}{L_x L_y}$ is introduced in each xy plaquette. The corresponding action is $1 - \mathrm{Tr}(e^{i\theta}) \approx \frac{1}{2}\theta^2$ in the pure $U(1)$ system. But in the $SU(3)$ system, if the flux is introduced in the λ_3 subgroup, the corresponding action is $1 - \frac{1}{3}\mathrm{Tr}\{\mathrm{diag}(e^{i\theta}, e^{-i\theta}, 1)\} \approx \frac{1}{3}\theta^2$. And if the flux is introduced in the λ_8 subgroup, the action is $1 - \frac{1}{3}\mathrm{Tr}\{\mathrm{diag}(e^{i\theta}, e^{i\theta}, e^{-2i\theta})\} \approx \theta^2$. Thus, a magnetic flux in the λ_3 or λ_8 subgroup incurs an action equal to $2/3$ or 2 times that in a $U(1)$ system, respectively. This is precisely what fig. 6.4 shows, with horizontal dotted lines corresponding to $2/3$ (subgroup λ_3), 2 (subgroup λ_8) or $14/3$ (2 units of flux in λ_3 plus 1 unit in λ_8). Note that these topological excitations are extremely stable: their sudden decay after 1000 Monte Carlo sweeps is due to our turning off the external potential which maintained the reconfined phase. Then, the full $SU(3)$ gauge symmetry is immediately restored, and the $U(1)$ fluxes can freely unwind.

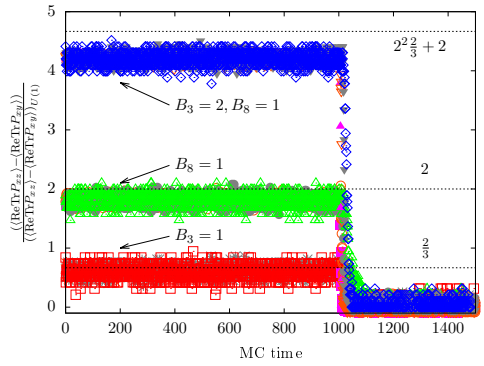

Figure 6.4: In an $SU(3)$ system in the reconfined phase ($U(1) \times U(1)$), magnetic flux is introduced in the xy plane. The corresponding shift in the xy plaquette, normalized to that in a pure $U(1)$ system, is shown for several flux combinations in the λ_3 and λ_8 subgroups. The dotted lines show the classical predictions. After 1000 sweeps, the gauge-symmetry breaking potential is turned off: the full gauge-symmetry is restored and the flux states decay immediately.

6.3.2 *Magnetic monopoles*

The next topological defect we have considered is a magnetic monopole, which is visible via its gauge-invariant $3d$ magnetic flux through the 6 faces of an elementary cube (see fig. 6.5 left). Actually, we are interested in a classical monopole, obtained by minimizing the action of a $3d$ $U(1)$ lattice of size L^3 containing one monopole. To enforce the presence of one monopole, we introduce a flux π through 3 of the faces of the lattice, and choose charge-conjugated periodic boundary conditions in each of the 3 directions, $U_\mu(x+L) = U_\mu^*(x)$. The resulting construction, fig. 6.5 right, is the analogue of the DeGrand-Toussaint monopole on the left, but on the scale L instead of a. It was already used in [98] to measure the monopole mass, but the numerical results presented there turn out to be incorrect.

Figure 6.6 left shows the minimum energy (measured by cooling) of a $U(1)$ magnetic monopole induced by the above boundary conditions, as a function of the size L of the cubic lattice. To understand its L-dependence, consider first a monopole of charge $Q_M = 2\pi/e$ in the continuum. The energy of the magnetic field inside a sphere of

radius R is $E(R) = 2\pi \int_0^R dr\ r^2\ B(r)^2$. It is UV-divergent, and the lattice spacing a will cutoff the integral and regularize the divergence. In the infrared, since $B(r) = Q_M/(4\pi r^2)$ as dictated by Gauss' law, one obtains $E(R=\infty) - E(R) = \frac{Q_M^2}{8\pi} \int_R^\infty dr 1/r^2 = \frac{1}{e^2}\frac{\pi}{2R}$. This calculation is slightly modified in a cubic box with C-periodic boundary conditions. The boundary conditions generate an infinite array of mirror charges, arranged in a cubic array of spacing L and alternating in sign, as in an Na^+Cl^- crystal. They interact via a $1/r$ potential, so that the energy of the array is proportional to $\alpha_3 = \sum'_{ijk} \frac{(-1)^{i+j+k}}{\sqrt{i^2+j^2+k^2}} = -1.74756..$, which is called Madelung's constant. The resulting monopole energy correction is $E(R=\infty) - E(R) = \frac{1}{e^2}\frac{\alpha_3}{2}\frac{\pi}{L} = \frac{2.745..}{L}$. This is precisely the $1/L$ dependence seen in fig. 6.6 left. Since its origin is infrared, this term is universal, i.e. independent of the lattice action considered. The leading term of course depends on the form of the ultraviolet cutoff, and thus is action-dependent. The additional, $1/L^3$, tiny corrections come from $(a/L)^2$ lattice corrections to the continuum Coulomb potential.

Now, as in the case of $U(1)$ fluxes, we can introduce a $U(1)$ monopole in a subgroup of an $SU(3)$ configuration. If the gauge symmetry is broken by the external Polyakov loop potential, the $U(1)$ monopole is stable, and we can measure its energy by cooling. The results are shown fig. 6.6 right. First, the monopole energy depends on the $U(1)$ subgroup chosen, just like for fluxes. This fact was first noticed in Ref. [34] which used Maximal Abelian gauge and Abelian projection to isolate the monopoles. Here, we obtain precise values for the monopole energies in the thermodynamic limit: contrary to the energies of flux states, the monopole energies are not obtained by applying a simple factor to the $U(1)$ case, because the UV-regularization of the monopole field differs in the different subgroups. Nevertheless, the coefficient of the $1/L$ correction, which comes from IR effects, varies as for flux states: it is $2/3$ and 2 times the $U(1)$ value for subgroups spanned by λ_3 and λ_8, respectively. Moreover, the $1/L^3$ coefficients scale in the same way, since they are all caused by the same lattice distortion of the Coulomb potential.

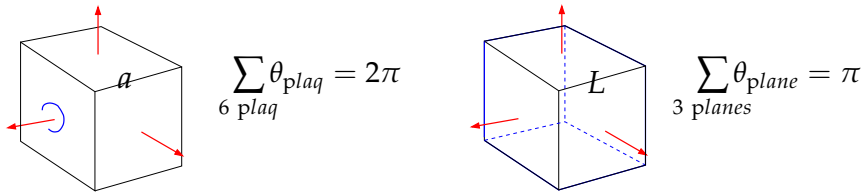

Figure 6.5: (*left*) DeGrand-Toussaint magnetic monopole in an elementary cube of size a. (*right*) The same construction on the scale L of the whole lattice ensures the presence of a magnetic monopole somewhere inside. Charge-conjugated boundary conditions are required to obtain non-zero fluxes at the boundary.

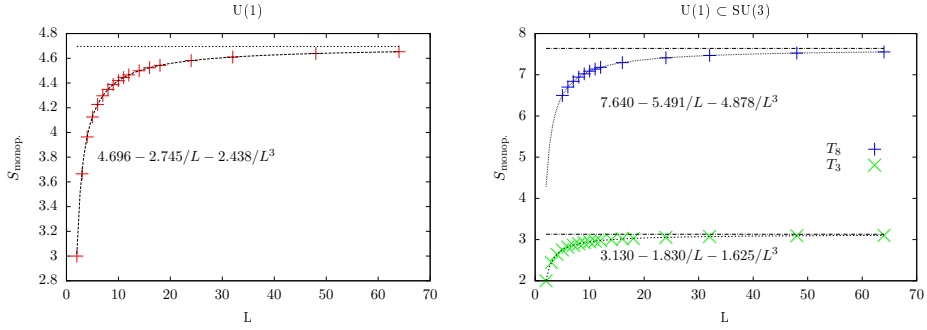

Figure 6.6: (*left*) Minimum action of a $U(1)$ magnetic monopole as a function of the size L of the cubic lattice. The $1/L$ correction is caused by the cubic array of image-charges with alternating signs, and its magnitude is exactly given by Madelung's constant. (*right*) Same, for a $U(1)$ magnetic monopole in the λ_3 or λ_8 sector of an $SU(3)$ system in the reconfined $(U(1) \times U(1))$ phase. The two types of monopoles have different masses. The $1/L$ correction is given by the correspondingly rescaled Madelung constant.

7

DEFORMATIONS OF INFRARED-CONFORMAL THEORIES IN TWO DIMENSIONS

7.1 INTRODUCTION

In this chapter we investigate another aspect of BSM physics, namely the notion that the Higgs boson could arise and be light due to a (nearly) scale-invariant extension of the SM. In order to evaluate the viability of such a theory on the lattice, it is important to be able to unambiguously determine whether a model is (nearly) conformal. This is no trivial matter since the lattice breaks conformal invariance explicitly, and a careful analysis has to be performed in order to disentangle the effects of the lattice from the true nature of the model, for example the weak breaking of scale invariance due to a small mass term.

The content of this chapter has been published in

- Oscar Akerlund and Philippe de Forcrand. „Deformations of infrared-conformal theories in two dimensions." In: *PoS* LATTICE2014 (2014), p. 243. arXiv: 1410.1178 [hep-lat].

7.2 DEFORMED CORRELATORS

To understand how a nonzero mass deforms a conformal model it is useful to look at the (Euclidean) two-point correlator of a conformal field with anomalous scaling dimension Δ, i.e. with a coordinate space two-point function $G(x) \propto (x^2)^{-\frac{d-2}{2}-\Delta}$, where d is the space-time dimension. Power counting tells us that the propagator in Fourier space is $\widetilde{G}(p) \propto (p^2)^{-1+\Delta}$ from which the free, massless case $\Delta = 0$ is evident. One can introduce a mass deformation in the usual sense by shifting the pole of the propagator from zero to im for which $\widetilde{G}(p) = (p^2 + m^2)^{-1+\Delta}$.

The zero spatial momentum euclidean time propagator is then given by a one-dimensional Fourier transform:

$$G(t,\vec{p}=0) \propto \int \mathrm{d}\omega\, \widetilde{G}\left(p=(\omega,\vec{0})\right) e^{-i\omega t} \tag{7.1}$$
$$= \int \mathrm{d}\omega\, (\omega^2+m^2)^{-1+\Delta} e^{-i\omega t} \propto \left(\frac{t}{m}\right)^{\frac{1}{2}-\Delta} K_{\frac{1}{2}-\Delta}(mt).$$

In the infrared ($mt \gg 1$) an expansion of the Bessel function reveals that the usual exponential decay due to the mass is modified by a power law in t:

$$G(t,\vec{p}=0) \propto \frac{e^{-mt}}{t^{\Delta}}. \tag{7.2}$$

This relation has been used in [65] as a method to extract anomalous scaling dimensions. However, it relies on a very strong assumption. Namely, the way to introduce a mass deformation is not unique. It has been pointed out [93] that a massless correlator with anomalous dimension Δ can be viewed as a field with a continuous mass distribution given by a power law with parameter $(\Delta-1)$, since

$$\left(p^2\right)^{-1+\Delta} = \frac{\sin \Delta\pi}{\pi} \int_0^{\infty} \mathrm{d}M^2\, \frac{\left(M^2\right)^{\Delta-1}}{p^2+M^2}. \tag{7.3}$$

Then, a finite mass deformation can be introduced by making the mass distribution $(M^2)^{\Delta-1}$ discrete with a finite mass spacing. The correlator will then change from a power law to an infinite sum of exponentials, which is conceptually different from a single exponential with a power correction. This second description offers a smooth transition from a scale invariant correlator to the familiar exponential correlator of a gapped system which is not present in the first. The second view will also be shown to be the correct one in the analysis of the critical Ising model below.

7.3 THE $2d$ CRITICAL ISING MODEL

The $2d$ critical Ising model is *the* textbook example of a conformal field theory. Everything about this model is known and the analytic expression for the two-point function on a torus is particularly useful for our purposes. However, first recall the form of the two-point function in $\mathbb{R}^2$:

$$\langle \sigma(0,0)\sigma(x,t)\rangle \propto \left(x^2+t^2\right)^{-\frac{1}{8}} \tag{7.4}$$

where the power law decay is governed by the scaling dimension $\Delta = \frac{1}{8}$ of the periodic spin field. On a torus of size $L_s \times L_t \equiv L \times (\tau L)$ the expression is slightly more complicated [66]

$$\langle \sigma(0,0)\sigma(x,t)\rangle = \frac{\sum_{\nu=1}^{4} |\vartheta_\nu(\frac{z}{2},q)|\,|\frac{2\pi\eta(i\tau)^3}{\vartheta_1(z,q)}|^{\frac{1}{4}}}{\sum_{\nu=2}^{4}|\vartheta_\nu(0,q)|}, \qquad (7.5)$$
$$z = \frac{\pi}{L}(x+it), \quad q = e^{-\pi\tau},$$

but the scaling dimension is still present in the exponent $\frac{1}{4} = 2\Delta$. $\vartheta_\nu(z,q)$ are the Jacobi theta functions which are quasi-doubly periodic in z and $\eta(z)$ is the Dedekind eta function. The nome q will often be referred to as a geometry factor since it depends on the aspect ratio τ. It is worth noting that although the size L explicitly breaks scale invariance, the correlation function is completely independent of L when expressed in the dimensionless variables $(\frac{x}{L}, \frac{t}{L})$ (see fig. 7.1). Actually, by taking a small z expansion of the two-point function on the torus, eq. (7.5), one obtains the $\mathbb{R}^2$-result, eq. (7.4). However, since a generic model can have distinct fixed points in the ultraviolet and the infrared it will be useful to study the infrared properties of eq. (7.5).

While eq. (7.5) is the exact solution it does not allow for an analytic summation over x, required to extract the zero spatial momentum temporal correlator. However, this is possible if we expand in powers of the geometry factor q (which is small even for a unit aspect ratio). The resulting correlator is given by

$$C(t_L,q,L) \propto \cosh\left(\tfrac{\pi}{4L}t_L\right) + \sum_{n=1}^{\infty}\Big\{c_n q^{2n}\cosh\left(m_n t_L\right) + \hat{c}_n q^{n+\frac{1}{4}}\cosh\left(\hat{m}_n t_L\right)\Big\}, \qquad (7.6)$$

where $t_L = t - \frac{\tau L}{2}$, $m_n = \frac{4\pi}{L}(n + \frac{1}{16})$, $\hat{m}_n = \frac{2\pi}{L}(n - \frac{1}{8})$ and, up to $\mathcal{O}(q^2)$,

$$c_n = \left(\frac{\Gamma(n+\frac{1}{8})}{n!\Gamma(\frac{1}{8})}\right)^2 + 2\Gamma(\tfrac{7}{8})^2 \sum_{m=0}^{\left\lfloor \frac{2n}{L} \right\rfloor} \frac{\Gamma(\frac{7}{8} - n + \frac{mL}{2})^{-1}\Gamma(1+n+\frac{mL}{2})^{-1}}{\Gamma(\frac{7}{8} - n - \frac{mL}{2})\Gamma(1+n-\frac{mL}{2})} \tag{7.7}$$

$$\begin{aligned}\hat{c}_n = &\sum_{m=0}^{n} \sum_{r=\max(0,2m-n)}^{m} \sum_{p=0}^{n+r-2m} (-1)^r \binom{-\frac{1}{8}}{m} \binom{\frac{1}{2}}{n+r+p-2m} \\ &\times \binom{n+r+p-2m}{2p} \binom{m}{r} \\ &\times \sum_{k=0}^{r} \binom{r}{k} \left(\binom{2p}{p+r-2k} + 2 \sum_{q=1}^{\left\lfloor \frac{r+p}{L} \right\rfloor} \binom{2p}{p+r-2k+qL} \right).\end{aligned} \tag{7.8}$$

We now see clearly that $\frac{4\pi}{L}(\frac{2\pi}{L})$ plays the role of a mass spacing in $m_n(\hat{m}_n)$and that we obtain a continuous distribution of masses in the $L \to \infty$ limit. This is even clearer if we consider the $\tau = \infty$, i.e. cylindrical geometry, and $L \gg 1$ limit of the correlator:

$$C(t,0,L) \propto \sum_{n=0}^{\infty} \left(\frac{\Gamma(n+\frac{1}{8})}{n!\Gamma(\frac{1}{8})}\right)^2 e^{-\frac{4\pi}{L}(n+\frac{1}{16})t}, \tag{7.9}$$

$$\frac{\Gamma(n+\frac{1}{8})}{n!} = n^{-\frac{7}{8}}\left(1 + \mathcal{O}(1/n)\right). \tag{7.10}$$

Going back to Fourier space with the $L \to \infty$ limit in mind one gets

$$\begin{aligned} C(\omega,0,L\to\infty) &\propto \frac{1}{L}\sum_{n=0}^{\infty} \left(\frac{L^2}{n^2}\right)^{\frac{7}{8}} \frac{8\pi\frac{n}{L}}{\left(4\pi\frac{n}{L}\right)^2 + \omega^2} \\ &\approx \int_0^\infty \mathrm{d}M\, 2M \frac{(M^2)^{-\frac{7}{8}}}{M^2+\omega^2} = \int_0^\infty \mathrm{d}M^2 \frac{(M^2)^{\frac{1}{8}-1}}{M^2+\omega^2}, \end{aligned} \tag{7.11}$$

which is exactly the relation eq. (7.3) for a conformal propagator. This shows how to obtain a massless correlator with an anomalous scaling dimension as the limit of a model with a scale. Also, this result casts doubt on the applicability to a cylindrical system of the description (7.2) where the pole of the anomalous propagator is shifted.

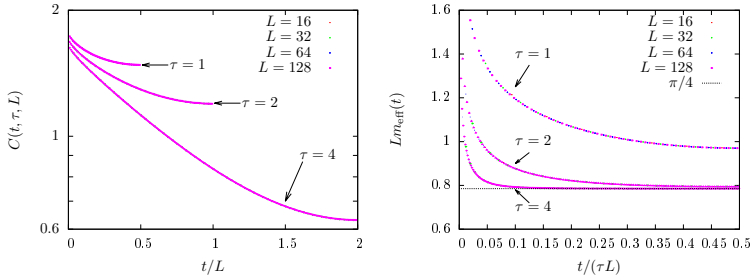

Figure 7.1: Zero-momentum correlators (*left*) and effective masses (*right*) of the critical $2d$ Ising model for various lattice sizes $L \times (\tau L)$. Note the false plateau of the effective mass far away from the lowest mass for $\tau = 1$.

At finite aspect ratio the second infinite sum in eq. (7.6) contributes more excited states with half the mass spacing. One finds that unless τ is larger than around four, these new states actually lead to a false mass plateau above $\pi/(4L)$ but the correlators still match after a rescaling of all dimensions which is consistent with the underlying conformal invariance. The effect of a small aspect ratio on the effective mass can be seen in fig. 7.1 (*right*).

Away from criticality, the solution of the $2d$ Ising model on a torus is not available. Therefore, we move to another model where a mass deformation can easily be introduced.

7.4 THE SOMMERFIELD MODEL

The Sommerfield model [90]

$$\mathcal{L} = \bar{\psi}(i\partial\!\!\!/ - eA\!\!\!/)\psi - \frac{1}{4}F^{\mu\nu}F_{\mu\nu} + \frac{m_0^2}{2}A^\mu A_\mu \tag{7.12}$$

is the Schwinger model with a mass term for the vector boson. The mass term breaks gauge invariance but makes it possible to construct a conserved axial current which protects the chiral symmetry. Since there is no chiral condensate, $\langle\bar{\psi}\psi\rangle$, the theory remains scale invariant for any value of the bi-fermion field anomalous scaling dimension between zero and minus one. This is in contrast to what happens in the one-flavor Schwinger model which stays scale-invariant due to the bi-fermion field having an anomalous scaling dimension of minus one which yields a

dimensionless condensate. In the Sommerfield model it turns out that the anomalous dimension can be tuned by changing the dimensionless ratio $\frac{\pi m_0^2}{e^2}$.

The model is solved [90, 54] by introducing a Hodge decomposition of the gauge field $A_\mu = \partial_\mu \mathcal{V} + \epsilon_{\mu\nu}\partial^\nu \mathcal{A}$ and a rotation of the fermion field $\Psi = e^{ie(\mathcal{V}+\mathcal{A}\gamma^5)}\psi$. In these new variables the Lagrangian is that of a free fermion and two scalar bosons:

$$\mathcal{L} = i\bar{\Psi}\partial\!\!\!/\Psi + \frac{m_0^2}{2}\partial_\mu \mathcal{V}\partial^\mu \mathcal{V} + \frac{1}{2}\mathcal{A}(\partial_\mu\partial^\mu)^2\mathcal{A} - \frac{m^2}{2}\partial_\mu \mathcal{A}\partial^\mu \mathcal{A}. \tag{7.13}$$

The shift in the mass $m^2 = m_0^2 + \frac{e^2}{\pi}$ comes from the change in the measure due to the $e^{ie\mathcal{A}\gamma_5}$ part of the fermion transformation, just as in the Schwinger model.

Since the "new" fermion Ψ is free it is easy to calculate its n-point functions which can then be dressed by the bosonic contribution to obtain the n-point functions of the original fermion fields ψ. We demonstrate the procedure by calculating the two-point function

$$\begin{aligned}\langle 0|\mathrm{T}\psi_\alpha(x)\psi^*_\beta(0)|0\rangle = \langle 0|\mathrm{T}e^{-ie(\mathcal{V}(x)+\mathcal{A}(x)\gamma^5)}e^{ie(\mathcal{V}(0)+\mathcal{A}(0)\gamma^5)}|0\rangle \\ \times \langle 0|\mathrm{T}\Psi_\alpha(x)\Psi^*_\beta(0)|0\rangle.\end{aligned} \tag{7.14}$$

Ψ_α, $\alpha \in \{1,2\}$ are the different chiralities of the fermion spinor and we have $\gamma_5\Psi_1 = \Psi_1$, $\gamma_5\Psi_2 = -\Psi_2$. Using the free bosonic propagators which can be read off from eq. (7.13),

$$\int \mathrm{d}^2x\, e^{ipx}\langle 0|\mathrm{T}\mathcal{V}(x)\mathcal{V}(0)|0\rangle = \frac{1}{m_0^2 p^2}, \tag{7.15}$$

$$\int \mathrm{d}^2x\, e^{ipx}\langle 0|\mathrm{T}\mathcal{A}(x)\mathcal{A}(0)|0\rangle = \frac{1}{m^2}\left(\frac{1}{p^2+m^2} - \frac{1}{p^2}\right), \tag{7.16}$$

we obtain

$$\langle 0|\mathrm{T}\psi_\alpha(x)\psi^*_\beta(0)|0\rangle = C_0(x)C(x)^{2\delta_{\alpha\beta}-1}S_0^{\alpha\beta}, \tag{7.17}$$

$$S_0^{\alpha\beta} \equiv \langle 0|\mathrm{T}\Psi_\alpha(x)\Psi^*_\beta(0)|0\rangle, \tag{7.18}$$

where

$$C(x) = \exp\left[\frac{e^2}{m^2}\left((D(x,m) - D(0,m)) - (D(x,0) - D(0,0))\right)\right], \tag{7.19}$$

$$C_0(x) = \exp\left[\frac{e^2}{m_0^2}\left(D(x,0) - D(0,0)\right)\right], \tag{7.20}$$

$$D(x,m) = \int \frac{\mathrm{d}^2 p}{(2\pi)^2} \frac{e^{-ipx}}{p^2 + m^2}. \tag{7.21}$$

The pseudo-scalar π_0 can be decomposed into the difference of two fermions bilinears,

$$\pi_0 \equiv \bar{\psi}\gamma_5\psi = \psi_2^*\psi_1 - \psi_1^*\psi_2 \equiv \mathcal{O} - \mathcal{O}^*, \tag{7.22}$$

$$\langle \pi_0 \pi_0^* \rangle = 2\langle \mathcal{O}\mathcal{O}^* \rangle - 2\mathrm{Re}\left[\langle \mathcal{O}\mathcal{O} \rangle\right]. \tag{7.23}$$

The "unparticle" operator $\mathcal{O}$ is composite and related to the product of two fermion operators

$$\psi_2^*(x_2)\psi_1(x_1) = c(x_1 - x_2)\mathcal{O}(x) + \cdots \tag{7.24}$$

through an operator product expansion. In correlators $\langle \mathcal{O}(t)\mathcal{O}(0) \rangle$ where $t \gg |x_1 - x_2|$ the coefficient $c(x_1 - x_2)$ can safely be dropped and $\mathcal{O}(t)$ can be considered a local operator. The resulting two-point functions can be obtained from the corresponding fermionic four-point functions and are found to be

$$\langle 0|\mathrm{T}\mathcal{O}(x)\mathcal{O}(0)^*|0\rangle = C(x)^4 |S_0^{12}(x)|^2, \tag{7.25}$$

$$\langle 0|\mathrm{T}\mathcal{O}(x)\mathcal{O}(0)|0\rangle = C(x)^{-4} S_0^{12}(x)^2. \tag{7.26}$$

The asymptotic behavior of the bosonic correction is

$$C(x) \propto \begin{cases} 1, & xm \ll 1 \\ (x^2)^{-\gamma_\mathcal{O}/4}, & xm \gg 1 \end{cases}, \quad \gamma_\mathcal{O} = -\frac{e^2}{\pi m^2} = -\frac{1}{1 + \frac{m_0^2 \pi}{e^2}}, \tag{7.27}$$

which makes it clear that $\gamma_\mathcal{O}$ is the anomalous dimension of $\mathcal{O}$ in the infrared. It can be varied between 0 for the free case, $e = 0$, and -1 for the Schwinger case, $m_0 = 0$. Since $\langle 0|\mathrm{T}\mathcal{O}(x)\mathcal{O}(0)|0\rangle$ decays faster than $\langle 0|\mathrm{T}\mathcal{O}(x)\mathcal{O}(0)^*|0\rangle$ by a factor of $(x^2)^{2\gamma_\mathcal{O}}$ (even exponentially on a finite lattice) the pseudo-scalar correlator will be dominated by the latter and we will focus on it from now on.

7.4.1 *On the lattice*

To study the Sommerfield model on a lattice of size $L_s \times L_t = (aN_s) \times (aN_t)$ we substitute the continuous momentum p with its lattice counterpart

$$a\tilde{p}_{s,t} = \sin\frac{2\pi}{N_{s,t}}(n + q_{s,t}), \quad a\hat{p}_{s,t} = 2\sin\frac{\pi n}{N_{s,t}}, \qquad (7.28)$$
$$n \in \{0, 1, 2, \ldots N-1\}, \quad q_{s,t} \in \{0, \tfrac{1}{2}\},$$

for fermions and bosons respectively, and all integrals with finite sums. The value of $q_{s,t}$ determines the boundary conditions of the fermions. In the spatial direction they can be either periodic (pbc, $q_s = 0$) or anti-periodic (apbc, $q_s = \frac{1}{2}$) whereas in the temporal direction only apbc, i.e. $q_t = \frac{1}{2}$, is allowed. The main effect of the spatial boundary conditions concerns the lower bound on the spatial momentum, $|\tilde{p}_s| \geq 2\pi q_s / L_s$ which, in the case of apbc, leads to a nonzero mass gap as that seen in the Ising model.

7.4.2 *Results*

If a fermion mass term is added to the Sommerfield Lagrangian chiral symmetry is explicitly broken but the method of solution remains the same, one just has to replace the massless fermion propagators by their massive counterparts. With this observation we can measure the "unparticle" mass as a function of the mass deformation. First, the mass is shifted from zero to $2\pi\gamma_{\mathcal{O}}$ (cf. Ising model with $\Delta = 1 + \gamma$). Furthermore, we can extract the anomalous mass dimension γ_m through the relation $Lm_{\mathcal{O}} \propto Lm_q^{1/y_m}$ where $y_m = 1 + \gamma_m$ is the total mass dimension. The results with $y_m = 1$ fixed at its exact value[1] are displayed in the upper left panel of fig. 7.2. Clearly, the data are not well described by the naive scaling ansatz. Our first attempt at improving the data collapse is to consider discretization errors of $m_{\mathcal{O}}$ (*upper right panel*). Another approach is to consider an N_s-dependent anomalous dimension which runs towards its fixed point value as $N_s \to \infty$ (*lower left panel*). Yet another approach is to consider corrections to scaling. In this case the naive scaling relation is changed to include also the first

1 This value can most easily be derived by considering the point-to-point correlator, esp. the condensate, and noticing that the m_q dependence is that of a free fermion model.

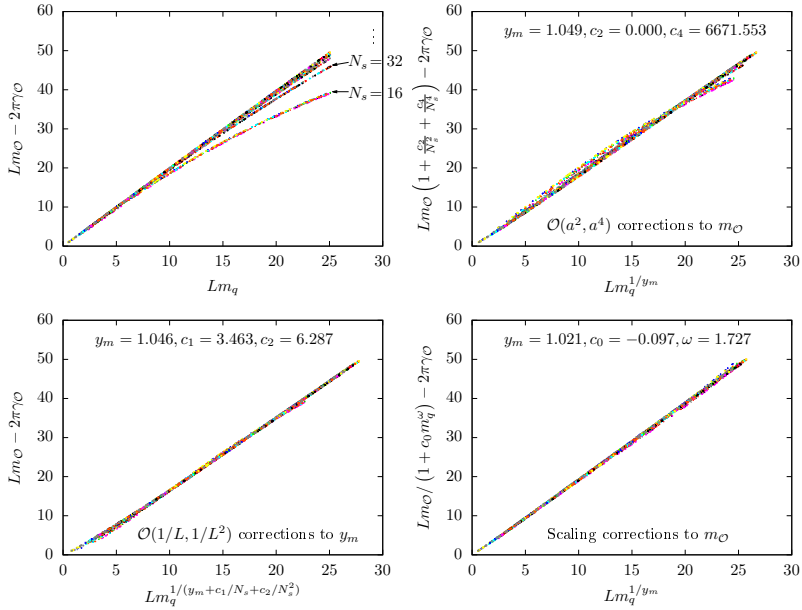

Figure 7.2: (Shifted) "unparticle" mass, $m_{\mathcal{O}}$, as a function of the bare mass deformation, m_q, and three different strategies to improve the data collapse. Note that the exact value of the anomalous mass dimension is $y_m = 1$. The results are obtained with periodic boundary conditions.

irrelevant operator and the result is displayed in the lower right panel of fig. 7.2. It is evident that all three methods greatly improve the data collapse and the resulting anomalous dimensions are close to the exact result. It is not obvious which method is the correct one but the issue could possibly be settled by calculating the next irrelevant operator and comparing its exponent with the fitted ω.

8

$U(1)$ LATTICE GAUGE THEORY WITH A TOPOLOGICAL ACTION

8.1 INTRODUCTION

In this chapter we use a non-standard, so-called topological, action to study compact $U(1)$ lattice gauge theory. The terminology comes from the fact that the action restricts the degrees of freedom to a subspace of the total phase space, on which the action is constant, such that it is invariant under smooth deformations of the degrees of freedom. An example of such an action is a spin model where each spin is restricted to be within some angle within each of its nearest neighbors. Since the action is constant, it does not allow for a derivative expansion, and thus no classical continuum limit exists. Nevertheless, it can be shown in some simple cases that such an action can reproduce the correct quantum continuum limit, and it is conjectured that this is the case also in more general cases. The motivation for considering such an action can be to improve the approach to the quantum continuum limit, as well as algorithmic advantages over conventional lattice actions. Apart from that, the very (non-)relation between the classical and quantum continuum limits is interesting to investigate on its own right.

The content of this chapter has been published in

- Oscar Akerlund and Philippe de Forcrand. „U(1) lattice gauge theory with a topological action." In: *JHEP* 06 (2015), p. 183. arXiv: 1505.02666 [hep-lat].

8.2 THE ACTION

In a gauge theory, the obvious analogue of restricting the angles between the neighboring spins of the spin model is to restrict the real part of the trace of each plaquette. The action then depends on one parameter α and is given by

$$e^{-S} = \begin{cases} 1 & \mathrm{ReTr} U_P > \alpha \quad \forall P \\ 0 & \text{else} \end{cases}, \tag{8.1}$$

where P denotes a plaquette. Note that this formulation is independent of the gauge group but that we from now on consider only $U(1)$ where $\mathrm{ReTr}U_P = \cos\theta_P$. We could thus equally well consider a restriction of the plaquette angle θ_P with $|\theta_P \mod 2\pi| < \delta_{\max} \equiv \arccos\alpha$. It is also important to note that the link angles, being gauge variant, are completely unrestricted. The most efficient way to generate configurations is to apply heatbath updates to the links one at a time under the constraint that no plaquette angle exceeds the allowed value. In principle this is realized by just uniformly sampling the interval $[0, 2\pi]$ until an acceptable angle has been found but in some cases it might be more efficient to explicitly construct the allowed range of values for the link to be updated. Note that a Metropolis update based on the old value may not be ergodic since the admissible region of link angles may not be connected. See fig. 8.1. However, there are some additional caveats to this kind of single link update which will become clear in the discussion of the magnetic monopoles.

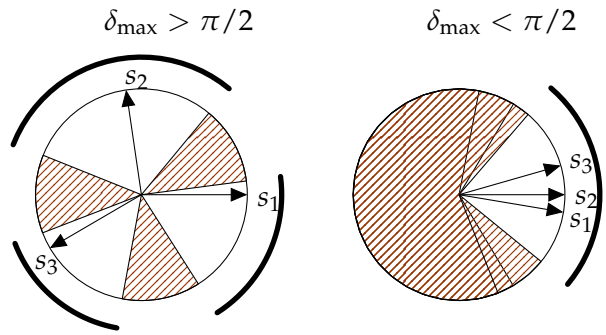

Figure 8.1: Forbidden regions (hatched areas) and allowed regions (black lines) for the angle of a link surrounded by three (the others are omitted for clarity) staples s_i. When the restriction angle $\delta_{\max} > \pi/2$ (*left panel*) the region can be disconnected whereas if it is smaller than $\pi/2$ (*right panel*) it will always be connected. $\delta_{\max}$ is the angle between an arrow and the edge of the hatched area opposite to it.

8.3 MAGNETIC MONOPOLES

An elementary cube on the lattice contains q magnetic monopoles if the outward oriented, physical ($\theta_P \in [-\pi, \pi[$) plaquette angles of its faces sum up to $2\pi q$ [42]. It is easy to check that $q \in \{0, \pm 1, \pm 2\}$ and that a cube with q monopoles must have at least one face with physical plaquette angle $|\theta_P| \geq |q|\pi/3$. This immediately tells us that for $\delta_{\max} < \pi/3$ there cannot be any monopoles and the topological action does not describe the same (lattice) physics as the Wilson action [1]. In fact, a change of variables from link to rescaled plaquette angles $\theta_P/\delta_{\max}$ can be used to see that all $\delta_{\max} < \pi/3$ are equivalent up to trivial rescalings. Let us therefore concentrate on angles larger than that.

One might think that if there is a deconfinement transition at some restriction angle $\delta_{\max}$ then it should be at $\delta_{\max} = \pi/3$ since this angle separates the region of no monopoles from a region with monopoles. This turns out to be wrong. In a sense this is analogous to the situation with the Wilson action. At the deconfinement transition the monopole density jumps down, but it does not jump to zero. The system can sustain a small density of monopoles without being confining. The same happens for the topological action with a deconfinement transition at a significantly larger restriction angle than $\pi/3$. Still, there is a non-analyticity in the monopole density at $\delta_{\max} = \pi/3$, which we investigate further in section 8.7 (see figs. 8.9 and 8.10).

8.3.1 *Creating monopoles*

To study how the monopoles depend on the cutoff angle $\delta_{\max}$ it is important to understand what the lowest monopole excitation is. It is well known that every monopole is connected to an anti-monopole via a Dirac string and that the monopole worldlines must form closed loops on the dual lattice. The shortest such loop has four vertices and Euclidean length $2\sqrt{2}a$ where a is the lattice spacing, and the smallest excitation is thus two monopoles and two anti-monopoles each located in one of the four cubes sharing a single plaquette. See fig. 8.2 for an illustration.

1 However, it should also be noted that the $U(1)$ monopole is a lattice artifact which disappears in the continuum limit also for the Wilson action.

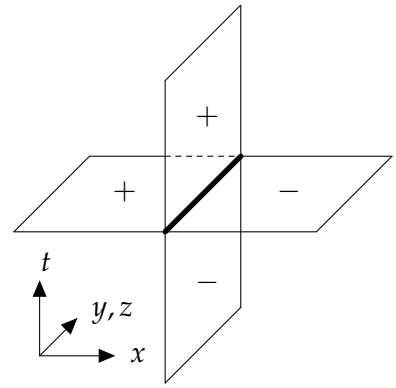

Figure 8.2: The smallest possible nontrivial loop of monopoles world lines which has Euclidean length $2\sqrt{2}a$. The y and z dimensions are collapsed into one so that each cube is represented by a plaquette and each plaquette by a link. The fat link represents the plaquette shared by all four cubes which contain a monopole. A $+(-)$ in a plaquette symbolizes a positively(negatively) charged monopole in the corresponding cube.

It is also important to consider how such a configuration is created from a configuration with zero monopoles. In order to create a monopole in a given cube we need to change its flux by 2π at the same time as we respect the constraints on the plaquette angles. It is therefore relevant to investigate the smallest constraint angle for which a change of 2π in the flux is possible. If we update a single edge of a cube we will change two of its six plaquettes. The sum of these changes must be 2π and the required angles can be minimized by letting the change be distributed equally over all involved plaquettes. Hence, the restriction on the plaquette angles gives $\delta_{\max} > \pi/2$ to create a monopole with a single link update. This means that for $\pi/2 > \delta_{\max} > \pi/3$ the single link update is not ergodic and cannot be used on its own. To have an ergodic algorithm we need to update at least three faces of a cube at the same time, which can only be done by updating more than one link at a time, as illustrated in fig. 8.3. The minimal update to achieve this is shown in the lower part of fig. 8.3 where two links of a given plaquette are updated together. This update changes three plaquettes in each of the four cubes sharing the plaquette common to the two updated

links, and we thus have a chance to create four monopoles down to $\delta_{\max} = \pi/3$ as required.

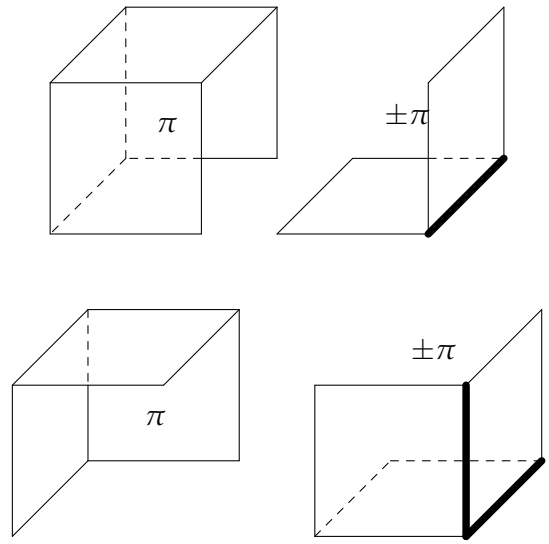

Figure 8.3: Monopole creation with a single link update (*upper panel*) and a multiple link update (*lower panel*). The fat links are the ones updated and the flux of π is spread over the plaquettes on the right which means that the single link update is ergodic down to $\delta_{max} = \pi/2$ and the two-link one to $\pi/3$.

8.4 THE HELICITY MODULUS

The helicity modulus was first introduced in the $2d$ XY-model [76] where it quantifies the response of the system to a twist in the boundary conditions. Because the twist is a boundary effect the helicity modulus is an order parameter for a system with one massive (finite correlation length) and one massless (infinite correlation length) phase. This is precisely the case of $4d$ lattice $U(1)$ gauge theory where the confining phase features massive photons whereas they are massless in the Coulomb phase. In the context of a gauge theory the twisted bound-

ary conditions can also be thought of as an external electromagnetic flux [98]. More precisely, we define the helicity modulus as

$$h \equiv \left. \frac{\partial^2 f(\phi)}{\partial \phi^2} \right|_{\phi=0}, \tag{8.2}$$

where f is the free energy density in the presence of the external flux ϕ. The flux is introduced by the replacement

$$\cos(\theta_P) \to \cos(\theta_P + \phi) \tag{8.3}$$

for all plaquettes in a given stack of plaquettes, i.e. all plaquettes in the set $\{P_{\mu\nu}(x) \mid \mu = \mu_0, \nu = \nu_0; x_\mu = x_0, x_\nu = y_0\}$. The orientation and position of the pierced stack is arbitrary and with a suitable change of variables the flux can also be spread out evenly over the (μ_0, ν_0)-planes. For the Wilson action h is a simple difference of expectation values

$$h = \beta \left(\langle \cos \theta_P \rangle - \beta \left\langle \left(\sum_{\text{stack}} \sin \theta_P \right)^2 \right\rangle \right), \tag{8.4}$$

where the sum in the second term is over all plaquettes in the stack defined above. For the topological action on the other hand, it is not possible to explicitly perform the derivatives. However, since the action for each configuration is the same, the free energy is given solely by the entropy, i.e. by the number of configurations with a given flux ϕ. This can be measured by promoting the flux to a dynamical variable, which is updated along with the link angles [23]. By measuring the probability distribution $p(\phi)$ (via a histogram method for example) of the visited fluxes one thus obtains the full 2π periodic free energy [98] and the helicity modulus

$$h = - \left. \frac{\partial^2 \log p(\phi)}{\partial \phi^2} \right|_{\phi=0}. \tag{8.5}$$

Alternatively, and more accurately, one can use all the global information from $p(\phi) = e^{-f(\phi)}$ and fit it to the classical ansatz [98]

$$f(\phi) = -\log \sum_k e^{-\frac{\beta_R}{2}(\phi - 2\pi k)^2} = -\log \vartheta_3 \left(\frac{\phi}{2}; e^{-\frac{1}{2\beta_R}} \right) - \frac{1}{2} \log 2\pi\beta_R, \tag{8.6}$$

where β_R plays the role of the renormalized coupling in the Coulomb phase and $\vartheta_3(z, q)$ is a Jacobi theta function. From this ansatz we can

extract the curvature at $\phi = 0$, i.e. h, analytically and we thus obtain both the helicity modulus and the renormalized coupling at the same time. We further note that they approach each other exponentially fast for large β_R. Together with eq. (8.4) we see that this means that $\beta_R \approx h \to \beta - 1/4$ as $\beta \to \infty$, which is to say that the coupling constant is not renormalized in the continuum limit which is of course common knowledge.

8.5 CONTINUUM LIMIT

It is important to dwell a little on the matter of a continuum limit for the topological action. Since all the plaquettes are forced to unity when $\delta_{\max} \to 0$ one expects that in this limit the correlation length diverges and thus that it defines a continuum limit. This point of view was examined more thoroughly by Budczies and Zirnbauer in [30]. These authors consider a general weight function $w_t(U_P)$, which is a function of a plaquette variable U_P and some parameter (coupling) t. Granted that there exists a t_c such that $w_{t_c}(U_P) = \delta(U_p - \mathrm{id})$ and that for $t \neq t_c$ the weight function is some smeared version of the δ-function, then the lattice gauge theory with partition function

$$Z_t = \int \mathrm{d}[U] \prod_P w_t(U_P) \tag{8.7}$$

has a continuum limit as $t \to t_c$. Furthermore, the authors claim that under "*favorable conditions*", the continuum theory will be Yang-Mills theory. It is not precisely defined what conditions are considered favorable, but close to the identity element, the plaquette variable is well approximated by $U_P = e^{ia^2 F_P} \approx 1 + ia^2 F_P - a^4 F_P^2$. Thus, in order for the continuum action to be $\propto \int \mathrm{Tr} F^2$ the weight function w_t certainly has to satisfy some conditions on the moments of the tangent vectors of the Lie group. At the very least the first moment must vanish and the second moment needs to exist and have the correct sign. The authors indeed give an example in [30] of a weight function, in two dimensions and for gauge group $U(N)$, which satisfies the δ-function condition but which has the wrong continuum limit. The problem is identified with the non-existence of the second moment for the considered weight function.

The topological action which we use clearly satisfies the δ-function constraint since the weight function has support only on a compact

region of width $\pm\delta_{\max}$ around the identity element and thus goes to $\delta(U_P - \mathrm{id})$ as $\delta_{\max} \to 0$. Because of the compact support and invariance under Hermitian conjugation we also conclude that the first moment vanishes and that the second is positive as it should. It is therefore probable that this action will have the correct quantum continuum limit and indeed all numerical evidence suggests that it does.

A simple check one can perform is to use for $w_t(U_P)$ a combination of angle restriction and Wilson plaquette term with negative β. By taking $\delta_{\max} \to 0$ the action still satisfies the δ-function constraint but the negative value of β will try to bend the distribution in the wrong direction to make the second moment of w_t negative. Clearly, for a fixed value of β the action will still be almost flat as long as $\delta_{\max}$ is small enough, so in order to change the continuum limit, β needs to be taken to $-\infty$ at the same time as $\delta_{\max} \to 0$. Then, if the magnitude of β is large enough we expect that the continuum limit is spoiled. This can also be observed in numerical simulations, and although it is somewhat of a pathological example it still gives some insight as to when one can expect to obtain the correct continuum limit.

8.6 FREE ENERGY

Here, we show how to evaluate the free energy, analytically in a $1d$ toy model, and numerically for more realistic cases.

8.6.1 $1d$ *XY model*

Consider a periodic chain of N spins $s_i \in O(2)$ with a topological action which restricts the angle of each link $\ell_i = s_i s_{i+1}^\dagger$ to be smaller than $\delta_{\max}$. Let $\ell_i = \exp(i\theta_i)$, $\theta_i \in [-\delta_{\max}, \delta_{\max}]$. The partition function of this model then takes a very simple form,

$$Z = \int_{-\delta_{\max}}^{\delta_{\max}} \prod_{i=1}^{N} \frac{\mathrm{d}\theta_i}{2\delta_{\max}} \delta\left(\exp\left(i \sum_{i=1}^{N} \theta_i\right) - 1\right) \tag{8.8}$$

and describes a collection of N non-interacting, constrained links with the only condition that the product of all links is one. The normalization of the angle integrals serves to keep Z finite as the number of links is taken to infinity and is just a subtraction of the ground state energy.

The total angle can take values $2\pi m$, $m \in \{-\left\lfloor \frac{N\delta_{\max}}{2\pi} \right\rfloor, \ldots, \left\lfloor \frac{N\delta_{\max}}{2\pi} \right\rfloor\}$ and thus m is the winding number or topological charge of the system. The partition function can be expressed solely in terms of the total angle by convoluting the uniform distributions of the individual links N times. The distribution of the sum of N i.i.d. uniform variables converges very rapidly to the normal distribution, in this case with zero mean and variance $N\delta_{\max}^2/3$. Anticipating the $N \to \infty$ limit we thus neglect the small deviations from the normal distribution and write

$$\begin{aligned} Z &= \sqrt{\frac{3}{2\pi N\delta_{\max}^2}} \int_{-N\delta_{\max}}^{N\delta_{\max}} \mathrm{d}\theta \, \exp\left(-\frac{3\theta^2}{2N\delta_{\max}^2}\right) \delta\left(\exp\left(i\theta\right) - 1\right) \\ &= \frac{\sqrt{3}}{(2\pi)^{3/2}\alpha} \sum_{m=-\left\lfloor \sqrt{N}\alpha \right\rfloor}^{\left\lfloor \sqrt{N}\alpha \right\rfloor} \exp\left(-\frac{3}{2}\left(\frac{m}{\alpha}\right)^2\right), \end{aligned} \tag{8.9}$$

where we have defined $\alpha \equiv \frac{\sqrt{N}\delta_{\max}}{2\pi}$. We can now take $N \to \infty$ whilst keeping α fixed to obtain

$$Z = \frac{\sqrt{3}}{(2\pi)^{3/2}\alpha} \sum_{m=-\infty}^{\infty} \exp\left(-\frac{3}{2}\left(\frac{m}{\alpha}\right)^2\right) = \frac{\sqrt{3}}{(2\pi)^{3/2}\alpha} \vartheta_3\left(\exp\left(-\frac{3}{2\alpha^2}\right)\right), \tag{8.10}$$

where $\vartheta_3(q) \equiv \vartheta_3(0, q)$ is the third Jacobi elliptic theta function. Since the sum in the partition function is over the winding number m it is straightforward to calculate $\langle m^2 \rangle$ and the topological susceptibility $\chi_t = \frac{1}{\beta}\langle m^2 \rangle$. In the limit $\beta = Na \propto \alpha^2 \to \infty$ (where a is the lattice spacing) one should find $\chi_t = \frac{1}{4\pi^2 I}$ where I is the moment of inertia of the quantum rotor which the model describes [22]. This allows us to determine α in terms of β and I and the result is $\alpha = \frac{\sqrt{3\beta/I}}{2\pi}$ which leads to

$$Z = \sqrt{\frac{I}{2\pi\beta}} \vartheta_3\left(\exp\left(-\frac{2\pi^2 I}{\beta}\right)\right). \tag{8.11}$$

With Poisson's summation formula we can go from the winding number representation to the energy representation in which

$$Z = \vartheta_3\left(\exp\left(-\frac{\beta}{2I}\right)\right) = \sum_{k=-\infty}^{\infty} \exp\left(-\frac{k^2\beta}{2I}\right). \tag{8.12}$$

It is now evident that the excited states are doubly degenerate and the energy differences are $E_k - E_0 = \frac{k^2}{2I}$ as is well known. The topological susceptibility is given in the two representations by

$$\begin{aligned}\chi_t &= \frac{\exp\left(-\frac{2\pi^2 I}{\beta}\right)\vartheta_3'\left(\exp\left(-\frac{2\pi^2 I}{\beta}\right)\right)}{\beta\vartheta_3\left(\exp\left(-\frac{2\pi^2 I}{\beta}\right)\right)} \\ &= \frac{1}{4\pi^2 I}\left(1-\beta\frac{\exp\left(-\frac{\beta}{2I}\right)\vartheta_3'\left(\exp\left(-\frac{\beta}{2I}\right)\right)}{\vartheta_3\left(\exp\left(-\frac{\beta}{2I}\right)\right)}\right). \end{aligned} \tag{8.13}$$

Since the elliptic function and its derivative are analytic functions $\forall\beta \in \mathbb{R}^+$ there is no phase transition but there are two distinct regimes with a rather abrupt crossover. In the low temperature regime, $\beta/I \gtrsim 10$, the partition function is almost independent of β and the topological susceptibility is very close to its zero temperature value $(4\pi^2 I)^{-1}$ whereas in the high temperature region, $\beta/I \lesssim 10$, the partition function is approximately $\sqrt{2\pi\beta}$ and χ_t rapidly drops to zero.

Note that, when $N\delta_{\max} < 2\pi$, topological excitations are forbidden and $\chi_t = 0$. However, the continuum limit is obtained while keeping $N\delta_{\max}^2$ fixed, so that the lattice spacing varies $\propto \delta_{\max}^2$. Therefore, in this $1d$ model the parameter region where $\chi_t = 0$ disappears in the continuum limit.

8.6.2 *Higher dimensions and gauge theories*

In higher dimensions, due to the lattice Bianchi identities, the integration over the constrained variables no longer factorizes and we can not calculate the partition function analytically anymore. However, in the small $\delta_{\max}$ regime where there are no topological defects the partition function must be

$$Z = (2\delta_{\max})^{n_{\text{d.o.f}}} \tag{8.14}$$

(or one, depending on the normalization), where $n_{\text{d.o.f}}$ is the number of independent degrees of freedom. As the topological defects are turned on, the functional dependence on $\delta_{\max}$ will change and there will be a high order and practically undetectable phase transition. As $\delta_{\max}$ is further increased the topological defects will start to play a more important role and eventually the *real* phase transition of the model will occur. If one would have access to the partition function, or free energy,

one could directly extract the properties of the transition. Fortunately, since the topological action is constant, the partition function is pure entropy and can thus be measured by Monte Carlo simulations by simply counting the number of configurations at a given value of $\delta_{\max}$. In fig. 8.4 we show the derivative of the free energy density $f = -V^{-1} \log Z$ with respect to $\delta_{\max}$ for the $2d$ XY-model (*left panel*) and the $4d$ $U(1)$ gauge theory (*right panel*) for various lattice volumes, obtained by Monte Carlo simulations. It is clear that the derivative is smooth in the XY-model where the transition is of infinite order (BKT) and that it is discontinuous in the $U(1)$ case where the transition is first order.

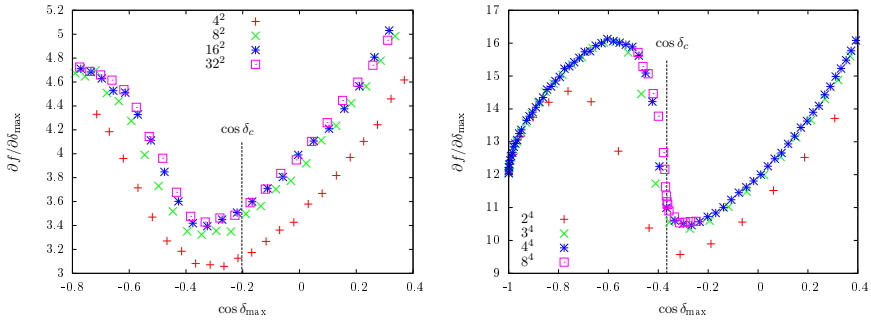

Figure 8.4: The derivative $\partial f/\partial\delta_{\max}$ of the free energy density $f = -V^{-1} \log Z$ for the $2d$ XY-model (*left panel*) and the $4d$ $U(1)$ gauge theory (*right panel*) as obtained from Monte Carlo simulations with a topological action. There is a clear distinction between the smooth derivative in the XY-model which has an infinite order phase transition and the discontinuous behavior, signaling a first order transition, in the $U(1)$ gauge theory. The vertical line marks the critical restriction $\cos\delta_c$. In the case of the XY-model it has been taken from [23] where it was extracted from a fit of the diverging correlation length.

8.7 RESULTS

Let us now turn to the numerical results. Primarily what we are interested in is the phase structure of the model and the order of the possible deconfinement transition. To this end we have measured

the monopole density and the helicity modulus as a function of the restriction $\cos\delta_{\max}$. We compare these results with the corresponding observables obtained with the Wilson action in figs. 8.5 and 8.6: it is obvious that the transition is even weaker than the weak first order transition seen with the Wilson action. We can try to quantify the strength of the transition by fitting the helicity modulus in the confining phase using a simple model of a first order transition [26, 98]

$$h(x) = \frac{h_+}{1 + X^{-1}\exp\left(-V\Delta f(x - x_c)\right)}, \tag{8.15}$$

where h_+ is the helicity modulus in the Coulomb phase (which is assumed to be constant), Δf is the latent heat, X is an anisotropy factor between the two phases and x is the coupling, either β or $\cos\delta_{\max}$. After taking finite size effects into account the best fit is shown as the lines in fig. 8.6. The data is well described by the ansatz and one finds that the fitted value of the latent heat for the topological action is about half of what it is using the Wilson action, which is consistent with the weaker transition seen in the monopole density.

To further establish that the transition really is first order we show histograms of the monopole density close to the transition for three different volumes in fig. 8.7. A double peak structure is formed and enhanced as the volume increases, which is a clear indication that the transition is first order. Also the Monte Carlo history shows clear tunneling events between two metastable states. Together with the discontinuity in the first derivative of the free energy with respect to the cutoff we conclude that the topological action has a first order transition at $\delta_{\max} \approx 1.95$.

To determine the characteristics of the two phases we look at how Wilson loops of different sizes behave. Naively, we expect an area law when $\delta_{\max}$ is close to π since the interaction between plaquettes will be very weak, as for the Wilson action where $\beta \ll 1$. This can be seen in the left panel of fig. 8.1. If the forbidden regions become very narrow then the individual links are hardly influenced by their neighbors and each plaquette angle is more or less uniformly distributed in the interval $[-\delta_{\max}, \delta_{\max}]$ which gives an average plaquette trace of $\sin(\delta_{\max})/\delta_{\max}$. For a loop with area A, this is raised to the A'th power. For restrictions $\delta_{\max}$ close to zero on the other hand, the links are heavily influenced by their neighbors (right panel of fig. 8.1) and the total angle of the

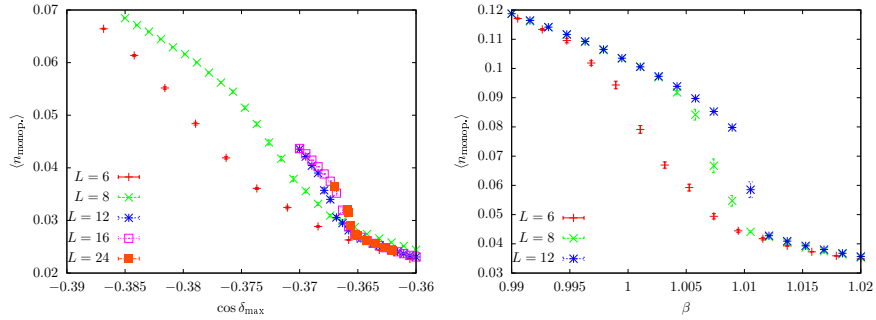

Figure 8.5: The monopole density n for the topological action (*left panel*) and the Wilson action (*right panel*). For the Wilson action the first order nature of the transition is rather evident even for a 12^4 lattice whereas for the topological action we have to go to much larger lattices to see a fairly distinct jump.

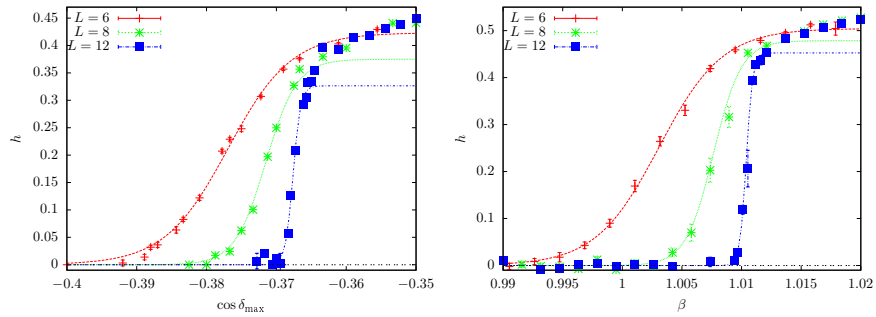

Figure 8.6: The helicity modulus h for the topological action (*left panel*) and the Wilson action (*right panel*). The lines are the best fit to eq. (8.15), which describes the data in the confining phase (the model assumes a constant h in the Coulomb phase) very well for both actions.

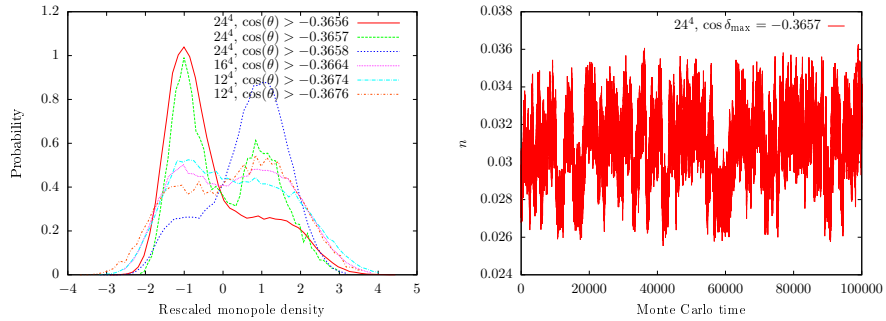

Figure 8.7: The probability distribution of the monopole density close to the transition for various volumes (*left panel*) and the corresponding Monte Carlo history for the 24^4 volume (*right panel*). The distributions are rescaled in such a way that one peak is at -1 and the other at $+1$. That way the separation of the peaks in relation to the widths can be directly compared between different volumes. It is evident that the two peaks become more distinct for larger volumes which indicates a first order transition. Also the obvious tunneling between two different states in the Monte Carlo history backs up this statement.

loop should depend on the perimeter rather than the area. This is demonstrated in fig. 8.8 where we show the Creutz ratios

$$\chi(R) = -\log \frac{\langle W(R,R)\rangle \langle W(R-1,R-1)\rangle}{\langle W(R,R-1)\rangle \langle W(R-1,R)\rangle}, \tag{8.16}$$

where $W(I,J)$ is a planar, rectangular Wilson loop with sides I and J. We have performed the $R \to \infty$ extrapolation under the assumption that the corrections are of the form e^{-R}. Note that this is not a precise measurement of the string tension but rather a characterization of the two phases. We have also checked that the magnitude of the Polyakov loop acquires a vacuum expectation value in the low monopole density phase.

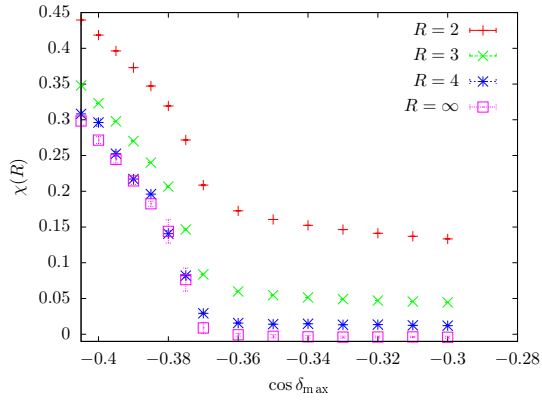

Figure 8.8: The Creutz ratios $\chi(R)$ given by eq. (8.16) as well as an $R \to \infty$ extrapolation assuming corrections of the form e^{-R} as a function of the restriction $\cos\delta_{\max}$ obtained on an 8^4 lattice. There is a clear transition between a confining phase with nonzero string tension and a deconfined phase with an perimeter law for the Wilson loops.

Another interesting thing to investigate is how the monopole density depends on the renormalized coupling. The monopole mass is proportional to $\beta_R = e_R^{-2}$ and the density decreases exponentially with the mass. This is a statement about physics so it gives us a direct way to compare the two actions. In fig. 8.9 we show the monopole density as a function of the renormalized coupling and we see a clear exponential decay as expected. For the topological action the decay is significantly faster, which could be interpreted as a reduction in the discretization

errors: for a given effective coupling, there are fewer lattice artifacts (monopoles) that disturb the order of the system. For $\delta_{\max} < \pi/3$ the density is even strictly zero and the model is completely insensitive (up to trivial rescalings) to further reduction of $\delta_{\max}$.

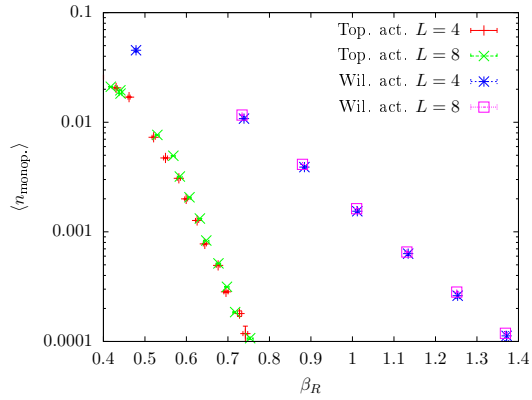

Figure 8.9: The monopole density in the Coulomb phase as a function of the renormalized coupling β_R, for the topological and the Wilson actions. The different rates of decay could be attributed to different lattice spacings for the two actions.

With a mix of single- and two-link updates we have been able to measure the monopole density down to densities around 10^{-8}. The exponential dependence on $\cos\delta_{\max}$ persists to $\delta_{\max} \approx 1.69$ after which the density smoothly changes into a power law in $(1/2 - \cos\delta_{\max})$ with an exponent which is fitted to be 11.70(6) as can be seen in fig. 8.10. We tentatively ascribe this change of functional behavior to the approach of a phase transition. A naive argument, which works well in the $2d$ XY-model, leads to a monopole density which is polynomial in the small deviation $(\delta_{\max} - \pi/3)$. The argument is based on convolutions of (near) uniform plaquette or link distributions. To create a single vortex in the spin model close to the threshold $\pi/2$ we need to convolve the link angle distribution four times, which makes the joint distribution $\propto (4\delta_{\max} - \theta)^3$ for the cumulative angle θ around a plaquette. This needs to be evaluated at $\theta = 2\pi$ (one vortex) which gives a vortex probability $\propto (\delta_{\max} - \pi/2)^3$. Vortices always come in pairs so we expect that the density is proportional to $(\delta_{\max} - \pi/2)^6$ which is in good agreement with what we have obtained from Monte Carlo simulations. By a similar argument one would expect a monopole density $\propto (\delta_{\max} - \pi/3)^{20}$ due

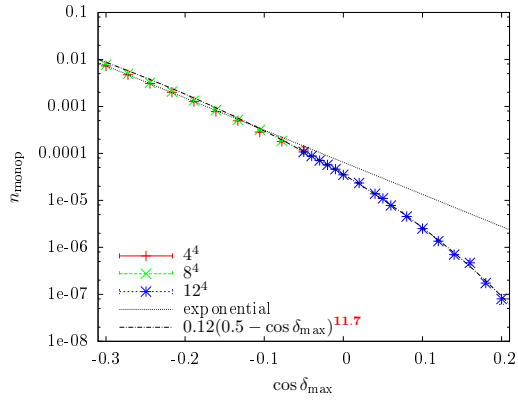

Figure 8.10: The monopole density for the topological action as a function of the restriction. There seems to be a smooth transition from an exponential decay to a power law at $\cos\delta_{\mathrm{max}} \approx -0.12$.

to six plaquettes in 4 cubes containing a monopole. The deviation in the power law from the predicted 20 to the observed ≈ 12 is rather large, but the argument does not take into account that the 4 monopoles are not independent of each other, so it is not so surprising that one finds a smaller exponent.

9

MEAN DISTRIBUTION APPROACH TO SPIN AND GAUGE THEORIES

9.1 INTRODUCTION

In this final chapter we introduce another generalization of MF theory, which not only determines the mean value of the variable in question, but a more general "mean distribution" over the values it can take. By doing so, a more realistic coupling of the field to its surrounding can be achieved, at the same time as more observables, even nonlocal ones like masses, become available. This new approach can be applied quite generally to a large number of models, but we will in particular study it in conjunction with a change of variables from the local, symmetry-variant variables to extended, symmetry-invariant variables, e.g. links instead of spins for a spin model or plaquettes instead of links in a gauge theory. The advantage of such a variable transformation is obvious in the case of a gauge theory, since the problem of determining the mean value of a gauge-dependent object, which would require gauge fixing, is circumvented.

The content of this chapter has been published in

- Oscar Akerlund and Philippe de Forcrand. „Mean Distribution Approach to Spin and Gauge Theories." In: *Nucl. Phys. B* 905 (2016), pp. 1–15. arXiv: 1601.01175 [hep-lat].

9.2 METHOD

9.2.1 *Mean Field Theory*

Let us for completeness give a very brief reminder of standard MF theory. Consider for definiteness a lattice model with a single type of

variables s which live on the lattice sites. The lattice action is assumed to be translation invariant and of the form

$$S = -\frac{1}{2}\sum_{i,j} J_{|i-j|} s_i^\dagger s_j + \sum_i V(s_i), \tag{9.1}$$

where i, j labels the lattice sites and $V(s)$ is some local potential. Let us now split the original lattice into a live domain D and an external bath D^c. The variables $\{s_i \mid i \in D^c\}$ all take a constant "mean" value $\bar{s}$. The MF action then becomes (up to a constant)

$$S_{\text{MF}} = -\frac{1}{2}\sum_{i,j\in D} J_{|i-j|} s_i^\dagger s_j + \sum_{i\in D}\left(V(s_i) - \sum_{j\in D^c} J_{|i-j|} s_i^\dagger \bar{s}\right), \tag{9.2}$$

where $\bar{s}$ is determined by the self-consistency condition that the average value of s in the domain D is equal to the average value in the external bath,

$$\langle s\rangle = \frac{\int \prod_{i\in D} \mathrm{d}s_i \, s_i e^{-S_{\text{MF}}}}{\int \prod_{i\in D} \mathrm{d}s_i \, e^{-S_{\text{MF}}}} \stackrel{!}{=} \bar{s}. \tag{9.3}$$

Once $\bar{s}$ has been determined the mean field action (9.2) can be used to measure other observables local to the domain D.

9.2.2 *Mean Distribution Theory*

To generalize the MF approach we relax the condition that the fields at the live sites interact only with the mean value of the external bath. Instead, the fields in the external bath are allowed to vary and take different values distributed according to a *mean distribution*. The self-consistency condition is thus that the distribution of the variables in the live domain equals the distribution in the bath.

Consider a real scalar theory for illustration purposes. Starting from the action

$$S = -2\kappa \sum_{\langle i,j\rangle} \phi_i\phi_j + \sum_i V(\phi_i), \tag{9.4}$$

with nearest neighbor coupling κ and a general on-site potential V, we expand the field $\phi \equiv \delta\phi + \bar{\phi}$ around its mean value $\bar{\phi}$ and integrate out all the fields except the field at the origin $\phi_0 = \bar{\phi} + \delta\phi_0$ and its nearest

neighbors, denoted ϕ_i, $i = 1, \ldots, z$, where z is the coordination number of the lattice. The partition function can then be written

$$Z = \int \mathrm{d}\phi_0 \, e^{-V(\phi_0)+2z\kappa\bar{\phi}\delta\phi_0} \int \prod_{i=1}^{z} \mathrm{d}\delta\phi_i \, p_J(\delta\phi_1, \ldots, \delta\phi_z) e^{2\kappa\delta\phi_0 \sum_{i=1}^{z} \delta\phi_i}, \quad (9.5)$$

where $p_J(\delta\phi_1, \ldots, \delta\phi_z)$ is a joint distribution function for the fields around the origin and absorbs everything not explicitly depending of $\delta\phi_0$ into its normalization. So far everything is exact and, given a way to compute p_J, we could obtain all local observables, for example $\langle \phi_0^n \rangle$. Now, p_J is in general not known, so we will have to make some ansatz and determine the best distribution compatible with this ansatz. In standard MF theory the ansatz is $p_J(\delta\phi_1, \ldots, \delta\phi_z) = \prod_{i=1}^{z} \delta(\delta\phi_i)$ and only $\bar{\phi}$ is left to be determined as explained above. In the mean distribution approach we will assume that the distribution is a *product* distribution $p_J(\delta\phi_1, \ldots, \delta\phi_z) = \prod_{i=1}^{z} p(\delta\phi_i)$ and determine p self-consistently to be equal to the distribution of $\delta\phi_0$, i.e.

$$p(\delta\phi_0) = \frac{1}{Z} e^{-V(\delta\phi_0+\bar{\phi})+2z\kappa\bar{\phi}\delta\phi_0} \left(\left\langle e^{2\kappa\delta\phi_0\delta\phi_i} \right\rangle_{p(\delta\phi_i)} \right)^z, \quad (9.6)$$

where $\langle f(\phi) \rangle_{p(\phi)} = \int \mathrm{d}\phi \, p(\phi) f(\phi)$. The mean value $\bar{\phi}$ has to be adjusted such that the distribution p has zero mean. After p and $\bar{\phi}$ have been determined any observable, even observables extending outside the live domain, can be extracted under the assumption that every plaquette is distributed according to p. Local observables are given by simple expectation values with respect to the distribution p.

This strategy can also be applied to spin and gauge models, taking as variables the links and plaquettes respectively, as discussed in the introduction. For a gauge theory, the starting point is the partition function in the plaquette formulation

$$Z = \int \prod_P \mathrm{d}U_P \prod_C \delta \left(\prod_{P \in \partial C} U_P - 1 \right) e^{-S[U_P]}, \quad (9.7)$$

where $S[U_p]$ is any action which is a sum over the individual plaquettes, for example the Wilson action $S[U_P] = \beta \sum_P (1 - \mathrm{ReTr} U_P)$, or a topological action as described in chapter 8, see also [22], where the action is constant but the traces of the plaquette variables are limited to a compact region around the identity.

The difference to the mean plaquette method is that it is not assumed that the external plaquettes take some average value, but rather that they are distributed according to a mean distribution. More specifically, we assume that there exists a mean distribution for the real part of the trace of the plaquettes and that the other degrees of freedom are uniformly distributed with respect to the Haar measure. Such a distribution must exist and it can be measured for example by Monte Carlo simulations. For definiteness let us consider compact $U(1)$ gauge theory with a single plaquette P_0 as the live domain. The plaquette variables $U_P = e^{i\theta_P} \in U(1)$ can be represented with a single real parameter $\theta_P \in [0, 2\pi]$ and the real part of the trace is $\cos\theta_P$. Our goal is to obtain an approximation to the distribution $p(\cos\theta_{P_0})$, or equivalently $p(\theta_{P_0}) = Z(\theta_{P_0})/Z$, where

$$Z(\theta_{P_0}) = e^{-S[U_{P_0}]} \int \prod_{P \neq P_0} \mathrm{d}U_P \, e^{-S[U_P]} \prod_C \delta\left(\prod_{P' \in \partial C} U'_P - 1 \right), \tag{9.8}$$

$$Z = \int \mathrm{d}U_{P_0} \, Z(\theta_{P_0}). \tag{9.9}$$

To obtain a finite number of integrals we now make the approximation that all plaquettes which do not share a cube with P_0 are independently distributed according to some distribution $p(\theta)$. Clearly this neglects some correlations among the plaquettes but this can be improved by taking a larger live domain. Again, let C denote an elementary cube with boundary ∂C and P denote a plaquette. We define

$$U_C \equiv \prod_{P \in \partial C} U_P, \tag{9.10}$$

$$\mathcal{C}_0 \equiv \{C \mid P_0 \in \partial C\}, \tag{9.11}$$

$$\mathcal{P}_\mathcal{C} \equiv \{P \mid \exists C \in \mathcal{C}_0 : \, P \in \partial C, \, P \neq P_0\}, \tag{9.12}$$

i.e. $\mathcal{C}_0$ is the set of all cubes containing P_0, and $\mathcal{P}_\mathcal{C}$ is the set of plaquettes, excluding P_0, making up $\mathcal{C}_0$. The sought distribution is then determined by the self-consistency equation

$$p(\theta_{P_0}) = \frac{e^{-S[U_{P_0}]} \int \prod_{P \in \mathcal{P}_\mathcal{C}} \mathrm{d}U_P \, p(\theta_P) \prod_{C \in \mathcal{C}_0} \delta(U_C - 1)}{\int \mathrm{d}U_{P_0} \, e^{-S[U_{P_0}]} \int \prod_{P \in \mathcal{P}_\mathcal{C}} \mathrm{d}U_P \, p(\theta_P) \prod_{C \in \mathcal{C}_0} \delta(U_C - 1)}. \tag{9.13}$$

This self-consistency equation is solved by iterative substitution: given an initial guess for the distribution $p^{(0)}(\theta_{P_0})$, it is a straightforward

task to integrate out the external plaquettes and obtain the next iterate $p^{(1)}(\theta_{P_0})$ from eq. (9.13), and to iterate the procedure until a fixed point is reached, i.e. $p^{(n+1)}(\theta_{P_0}) = p^{(n)}(\theta_{P_0})$. This is a functional equation, which is solved numerically by replacing the distribution p by a set of values on a fine grid in θ_P or by a truncated expansion in a functional basis. In this paper we have chosen to discretize the distribution on a grid. As mentioned above, this can be done in a completely analogous way also for spin models and for different types of actions. In Fig. 9.1 we compare the distributions of plaquettes in the $4d$ $U(1)$ lattice gauge theory with the Wilson action close to the critical coupling (*left panel*) and with the topological action at the critical restriction δ_c (*right panel*), obtained by Monte Carlo on an 8^4 lattice and by the mean distribution approach with the normalized action $e^{\beta\cos\theta_P}$. Below we give more details for a selection of models along with numerical results.

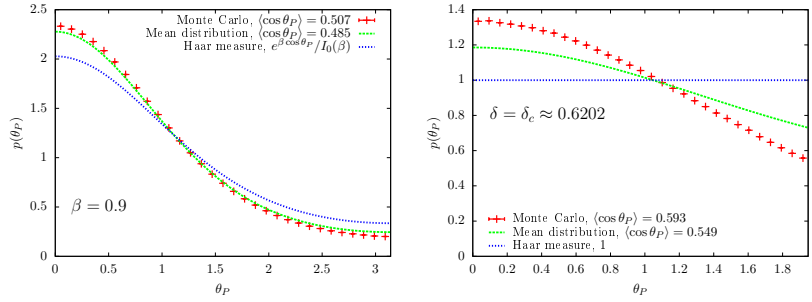

Figure 9.1: The distribution of plaquettes angles $p(\theta_P)$ in the $4d$ $U(1)$ lattice gauge theory with the Wilson action close to the critical coupling (*left panel*) and with the topological action at the critical restriction δ_c (*right panel*) obtained by Monte Carlo on an 8^4 lattice and by the mean distribution approach, together with the Haar measure.

9.3 SPIN MODELS

We will start by applying the method to a few spin models, namely $\mathbb{Z}_2$, $\mathbb{Z}_4$ and the U(1) symmetric XY-model and we will explain the procedure as we go along. Afterwards, only minor adjustments are needed in order to treat gauge theories. We will derive the self-consistency

equations in an unspecified number of dimensions although graphical illustrations will be given in two dimensions for obvious reasons.

Let us start with an Abelian spin model with a global $\mathbb{Z}_N$ symmetry. The partition function is given by

$$Z = \sum_{\{s\}} \exp\left(\beta \sum_{\langle i,j\rangle} \mathrm{Re}\, s_i s_j^\dagger\right), \tag{9.14}$$

where $s_i = e^{i\frac{2\pi}{N}n_i}$, $n_i \in \{1, \cdots, N\} (\in \mathbb{Z}_N)$. In the usual MF approach we would self-consistently determine the mean value of s_i by letting one or more live sites fluctuate in an external bath of mean valued spins. However, Batrouni [17, 19] noticed that by self-consistently determining the mean value of the *links*, or internal energy, $U_{ij} \equiv s_i s_j^\dagger$, much better estimates of for example the critical temperature could be obtained for a given live domain. Thus, we first change variables from spins to links. The Jacobian of this change of variables is a product of lattice Bianchi identities, $\delta(U_P - 1)$, one for each plaquette [1]. This can be verified by introducing the link variables U_{ij} via $\int \mathrm{d}U_{ij}\, \delta\left(U_{ij} s_j s_i^\dagger - 1\right)$ and integrating out the spins in a pedestrian manner. Since the Boltzmann weight factorizes over the link variables, all link interactions are induced by the Bianchi identities and hence the transformation trivially solves the one dimensional spin chain where there are no plaquettes [2].

As mentioned above, each δ-function can be represented by a sum over the characters of all the irreducible representations of the group. For $\mathbb{Z}_N$ this is merely a geometric series, $\delta(U_P - 1) = \frac{1}{N}\sum_{n=0}^{N-1} U_P^n$. Since only the real part enters in the action it is convenient to reshuffle the sum so that we sum only over real combinations of the variables,

$$\delta(U_P - 1) \propto 1 + U_P^{N/2}\delta^N_{\text{even}} + \sum_{n=1}^{\lfloor\frac{N-1}{2}\rfloor} \left(U_P^n + U_P^{-n}\right), \tag{9.15}$$

where δ^N_{even} is 1 if N is even and 0 otherwise.

The next step is to choose a domain of live links. In this step, imagination is the limiting factor; for a given number of live links there can be many different choices and it is not known to us if there is a way to decide which is the optimal one. The simplest choice is of course to keep only one link alive but in our $2d$ examples we will make

1 On a periodic lattice there are also global Bianchi identities but they play no role here.
2 Up to a global constraint in the case of periodic boundary conditions

use also of a nine-link domain [19] to see how the results improve with larger domains. These two domains are shown in the left (one link) and right (nine links) panels of Fig. 9.2. In the case of a single live link, there are $2(d-1)$ plaquettes and thus there are $2(d-1)$ δ-functions of the type in eq. (9.15).

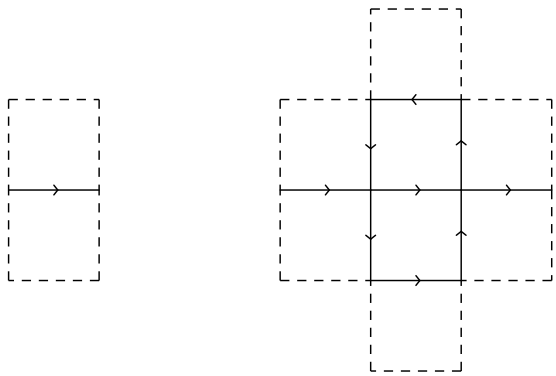

Figure 9.2: Two choices of domains of live links for $2d$ spin models. The live links are denoted by the solid lines, whereas the dashed lines denote links which are assumed to take mean values or to be distributed according to the mean distribution. The left panel shows the unique domain with one live link and the right panel shows one of many domains with nine live links.

9.3.1 *Mean link approach*

Let us for simplicity consider the case of one live link, denoted U_0. The external links, denoted U_k by some enumeration $ij \to k$, are fixed to the mean value by demanding that $U_k^n = U_k^{-n} = \langle U \rangle^n$, $\forall k \neq 0$. Each plaquette containing the live link also contains three external links, and the δ-function eq. (9.15) becomes

$$\delta\left(U_P - 1\right) \propto 1 + \langle U \rangle^{3N/2} (-1)^{n_0} \delta^N_{\text{even}} + 2 \sum_{n=1}^{\lfloor \frac{N-1}{2} \rfloor} \langle U \rangle^{3n} \cos \frac{2\pi n_0 n}{N}. \quad (9.16)$$

For large N it is best to perform the sum analytically to obtain (for $N = 2M$)

$$\delta\left(U_P - 1\right) \propto \frac{1 - (-1)^{n_0} \langle U \rangle^{3M}}{1 + \langle U \rangle^6 - 2 \langle U \rangle^3 \cos \frac{\pi n_0}{M}}. \quad (9.17)$$

For U(1) we define $\frac{\pi n_0}{M} = \theta_0$ as $M \to \infty$ and since $\langle U \rangle < 1$ we get

$$\delta\left(U_P - 1\right) \propto \left(1 + \langle U \rangle^6 - 2\langle U \rangle^3 \cos\theta_0\right)^{-1}, \tag{9.18}$$

which can efficiently be dealt with by numerical integration. The partition functions for the single live link for $\mathbb{Z}_2$, $\mathbb{Z}_4$ and $U(1)$ [3] spin models then become

$$Z_{\mathbb{Z}_2} \propto \sum_{U_0=\pm 1} e^{\beta U_0}\left(1 + \langle U \rangle^3 U_0\right)^{2(d-1)}, \tag{9.19}$$

$$Z_{\mathbb{Z}_4} \propto \sum_{n_0=0}^{3} e^{\beta\cos\frac{\pi n_0}{2}}\left(1 + \langle U \rangle^6 (-1)^{n_0} + 2\langle U \rangle^3 \cos\frac{\pi n_0}{2}\right)^{2(d-1)}, \tag{9.20}$$

$$Z_{U(1)} \propto \int_{-\delta}^{\delta} \mathrm{d}\theta\, e^{\beta\cos\theta}\left(1 + \langle U \rangle^6 - 2\langle U \rangle^3 \cos\theta\right)^{-2(d-1)}. \tag{9.21}$$

In the $U(1)$ case, eq. (9.21) applies both to the standard action ($\beta \geq 0, \delta = \pi$) and to the topological action ($\beta = 0, \delta \leq \pi$).

9.3.2 *Mean distribution approach*

In the mean distribution approach we sum over the external links assuming they each obey a mean distribution $p(U)$, for which a one-to-one mapping to the set of moments $\{\langle U^n \rangle\}$ exists. The difference between the two methods becomes apparent when expressed in terms of the moments, which are obtained by integrating the distributions of the external links against the δ-function given by the Bianchi constraint in eq. (9.15)

$$\sum_{\{U_1,U_2,U_3\}} p(U_1)p(U_2)p(U_3)\delta(U_P - 1) = 1 + \left\langle U^{N/2}\right\rangle^3 U_0^{N/2}\delta^N_{\text{even}} + 2\sum_{n=1}^{\lfloor \frac{N-1}{2} \rfloor} \langle U^n \rangle^3 \cos\frac{2\pi n_0 n}{N}. \tag{9.22}$$

Comparing to eq (9.16), we see that for $N \leq 3$ there is only one moment and the two methods are thus equivalent, but for larger N the mean link

3 The $U(1)$ Wilson action is defined by $\delta = \pi, \beta \neq 0$ and the topological action by $\delta < \pi, \beta = 0$.

approach makes the approximation $\langle U^n \rangle = \langle U \rangle^n$ whereas the mean distribution approach treats all moments correctly.

Thus, for small N we do not expect much difference between the two approaches, and this is indeed confirmed by explicit calculations. For $U(1)$, however, there are infinitely many moments which are treated incorrectly by the mean link approach and this renders the mean distribution approach conceptually more appealing.

By using the Bianchi identities, one link per plaquette can be integrated out, giving

$$Z_{U(1)} = \int_{-\delta}^{\delta} \mathrm{d}\theta \, e^{\beta \cos\theta} \left(\int_{-\delta}^{\delta} \mathrm{d}\theta_1 \mathrm{d}\theta_2 \, p(\theta_1) p(\theta_2) \sum_{n=-2}^{2} p(2\pi n - \theta - \theta_1 - \theta_2) \right)^{2(d-1)}. \tag{9.23}$$

It is often convenient not to work solely with distributions of single links, but also of multiple links, which are defined in the obvious way,

$$p_N(\Theta) \equiv \int \prod_{i=1}^{N} \mathrm{d}\theta_i \, p(\theta_i) \delta \left(\sum_{i=1}^{N} \theta_i - \Theta \right), \tag{9.24}$$

and can efficiently be calculated recursively. The above partition function then simplifies slightly to

$$Z_{\mathrm{U}(1)} = \int_{-\delta}^{\delta} \mathrm{d}\theta \, e^{\beta \cos\theta} \left(\int_{-2\delta}^{2\delta} \mathrm{d}\Theta \, p_2(\Theta) \sum_{n=-2}^{2} p(2\pi n - \theta - \Theta) \right)^{2(d-1)}. \tag{9.25}$$

In Figs. 9.3 and 9.4 we show results for $2d$ $\mathbb{Z}_2$, $\mathbb{Z}_4$ and $U(1)$ spin models, the latter for the Wilson action $S = \beta \sum_{\langle ij \rangle} \mathrm{Re}\, s_i s_j^\dagger$ and the topological action $e^S = \prod_{\langle ij \rangle} \Theta\left(\delta - |\theta_i - \theta_j|\right)$. Note the remarkable accuracy of the mean distribution approach in the latter case, even when there is only one live link.

9.4 GAUGE THEORIES

To extend the formalism from spin models to gauge theories, we merely have to change from links and plaquettes to plaquettes and cubes. The partition function for a $U(1)$ gauge theory analogous to eq.(9.21) becomes

$$Z_{\mathrm{U}(1)} = \int_{-\delta}^{\delta} \mathrm{d}\theta \, e^{\beta \cos\theta} \left(1 + \langle U \rangle^{10} - 2 \langle U \rangle^{5} \cos\theta \right)^{-2(d-2)} \tag{9.26}$$

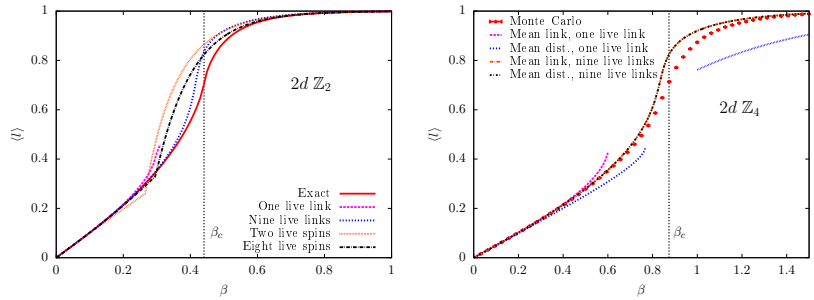

Figure 9.3: (*left*) Mean-field and mean-link approximation in the $2d$ Ising model for two choices of live domains. (*Right*) Mean-link and mean-distribution in the $2d$ $\mathbb{Z}_4$ model. In the Ising case, mean-link and mean-distribution are equivalent.

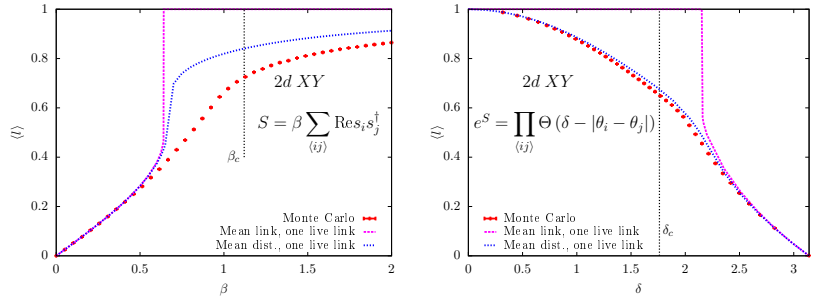

Figure 9.4: The mean link in the $2d$ XY spin model as a function of the Wilson coupling β (*left panel*) and of the restriction δ (*right panel*) from Monte Carlo, from the mean link and from the mean distribution methods.

in the mean plaquette approach and

$$Z_{\mathrm{U}(1)} = \int_{-\delta}^{\delta} \mathrm{d}\theta \, e^{\beta \cos\theta} \left(\int_{-4\delta}^{4\delta} \mathrm{d}\Theta \, p_4(\Theta) \sum_{n=-3}^{3} p(2\pi n - \theta - \Theta) \right)^{2(d-2)} \tag{9.27}$$

in the mean distribution approach. Results for $d = 4$ are shown in Fig. 9.5 for the Wilson action (*left panel*) and for the topological action (*right panel*).

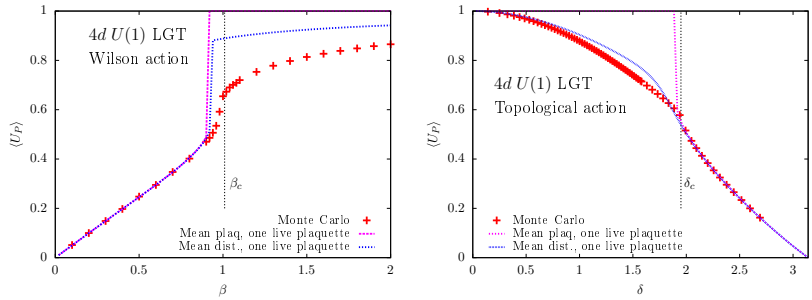

Figure 9.5: The mean plaquette in the $4d$ $U(1)$ gauge theory as a function of the Wilson coupling β (*left panel*) and the restriction δ (*right panel*) from Monte Carlo, and from the mean plaquette and the mean distribution methods.

Another nice feature of the mean distribution approach is that other observables become available, like for instance the monopole density in the $U(1)$ gauge theory, under the assumption that each plaquette is distributed according to the mean distribution p. A cube is said to contain q monopoles if the sum of its outward oriented plaquette angles sums up to $2\pi q$. Given the distribution $p(\theta)$ of plaquette angles the (unnormalized) probability p_q of finding q monopoles in a cube is given by

$$p_q = \int \prod_{i=1}^{6} \mathrm{d}\theta_i \, p(\theta_i) \delta \left(\sum_{i=1}^{6} \theta_i - 2q\pi \right), \; q \in \{-2, -1, 0, 1, 2\} \tag{9.28}$$

and the monopole density n_{monop} is given by

$$n_{\mathrm{monop}} = \frac{2p_1 + 4p_2}{p_0 + 2p_1 + 2p_2}. \tag{9.29}$$

In Fig. 9.6 we show the monopole densities for $4d$ $U(1)$ gauge theory as obtained by Monte Carlo simulations and by the mean distribution

approach. Note that the monopole extends outside of the domain of a single live plaquette, which was used to determine the mean distribution p. The left panel shows results for the Wilson action and in the right panel the topological action is used.

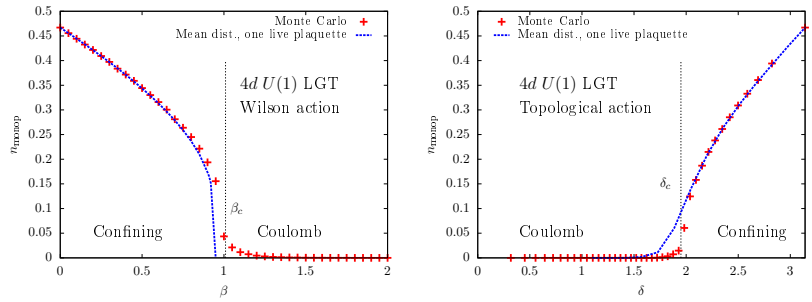

Figure 9.6: The monopole density in the $4d$ $U(1)$ gauge theory as a function of the Wilson coupling β (*left panel*) and the restriction δ (*right panel*) from Monte Carlo and the mean distribution method.

We can also treat $SU(2)$ Yang-Mills theory without much difficulty. For the mean plaquette approach we need the character expansion of the δ-function

$$\delta\left(U_C - 1\right) \propto \sum_{n=0}^{\infty} (n+1) \frac{\sin(n+1)\theta_C}{\sin\theta_C}, \tag{9.30}$$

where θ_C is related to the trace of the cube matrix U_C through $\mathrm{Tr} U_C = 2\cos\theta_C$.

In the mean plaquette approach we again make the substitution $U_C \to U_0 \langle U \rangle^5$ in the case of a single live plaquette. The above delta function then becomes

$$\begin{aligned} \delta\left(U_0 \langle U \rangle^5 - 1\right) &\propto \sum_{n=0}^{\infty} \langle U \rangle^{5n} (n+1) \frac{\sin(n+1)\theta_0}{\sin\theta_0} \\ &\propto \left(1 + \langle U \rangle^{10} - 2\cos\theta_0 \langle U \rangle^5\right)^{-2}. \end{aligned} \tag{9.31}$$

For $SU(2)$, the analogue of a restriction δ on the plaquette angle is a restriction on the trace of the plaquette matrix to the domain $[2\alpha, 2]$, where $-1 \leq \alpha < 1$. If we define $a_0 \equiv \frac{1}{2}\,\mathrm{Tr}\, U_0 = \cos\theta_0$ the approximate

$SU(2)$ partition function can be written [4] in a way very similar to the $U(1)$ partition function (9.26)

$$Z_{\mathrm{SU(2)}} = \int_{\alpha}^{1} \mathrm{d}a_0 \sqrt{1-a_0^2}\, e^{\beta a_0} \left(1 + \langle U\rangle^{10} - 2\langle U\rangle^{5} a_0\right)^{-4(d-2)}, \quad (9.32)$$

from which $\langle U\rangle$ can be easily obtained as a function of α and β.

The mean distribution approach works in a completely analogous way as for $U(1)$, but let us go through the details anyway, since there are now extra angular variables to be integrated out. The starting point is again an elementary cube on the lattice. Five of the cubes faces have their trace distributed according to the distribution $p(a_0)$ and we want to calculate the distribution of the sixth face compatible with the Bianchi identity $U_C = 1$. In other words, taking U_6 as the live plaquette, we want to evaluate

$$\tilde{p}(a_{0,6}) \propto \int \mathrm{d}\Omega_6 \int \prod_{i=1}^{5} \{\mathrm{d}U_i\, p\,(a_{0,i})\}\, \delta\left(\prod_{i=1}^{6} U_i - 1\right)\Bigg|_{\mathrm{Tr}U_6 = 2a_{0,6}}, \quad (9.33)$$

where we have decomposed $U_6 = \Omega_6 \hat{U}_6 \Omega_6^{\dagger}$ with $\hat{U}_6$ a diagonal $SU(2)$ matrix with trace $2a_{0,6}$, i.e. Ω_6 is the angular part of U_6. To facilitate the calculation we recursively combine the product of four of the plaquette matrices into one matrix, $U_1U_2U_3U_4 \to \tilde{U}$, by pairwise convolution of distributions (with $p_1(a_0) \equiv p(a_0)$)

$$\begin{aligned} p_{2i}(\tilde{a}_0) &\propto \frac{1}{\sqrt{1-\tilde{a}_0^2}} \int \mathrm{d}\tilde{\Omega}\mathrm{d}U_1\mathrm{d}U_2 p_i\,(a_{0,1})\, p_i\,(a_{0,2})\, \delta\left(U_1U_2\tilde{U}^{\dagger} - 1\right)\Big|_{\mathrm{Tr}\tilde{U} = 2\tilde{a}_0} \\ &\propto \frac{1}{\sqrt{1-\tilde{a}_0^2}} \int_{\alpha_i}^{1} \mathrm{d}a_{0,1}\sqrt{1-a_{0,1}^2}\mathrm{d}a_{0,2}\sqrt{1-a_{0,2}^2}\, p_i(a_{0,1}) p_i(a_{0,2}) \\ &\quad \times \int_{-1}^{1} \mathrm{d}\cos\theta_{12}\, \delta\left(\tilde{a}_0 - a_{0,1}a_{0,2} - \sqrt{1-a_{0,1}^2}\sqrt{1-a_{0,2}^2}\cos\theta_{12}\right) \\ &= \frac{1}{\sqrt{1-\tilde{a}_0^2}} \int_{\alpha_i}^{1} \mathrm{d}a_{0,1}\mathrm{d}a_{0,2}\, p_i\,(a_{0,1})\, p_i\,(a_{0,2})\, \chi_{|\tilde{a}_0 - a_{0,1}a_{0,2}| \le \sqrt{1-a_{0,1}^2}\sqrt{1-a_{0,2}^2}}, \end{aligned} \quad (9.34)$$

4 The $SU(2)$ Wilson action is defined by $\alpha = -1, \beta \neq 0$ and the topological action by $\alpha > -1, \beta = 0$.

where $\alpha_1 \equiv \alpha$, $\alpha_{2i} = \max(2\alpha_i - 1, -1)$ and χ_A is the characteristic function on the domain A. The domain of integration in the $(a_{0,1}, a_{0,2})$-plane is simply connected with parametrizable boundaries and comes from the condition that the argument of the delta function has a zero for some $\cos\theta_{12} \in [-1, 1]$. We then obtain for the sought distribution

$$\tilde{p}(a_{0,6}) \propto \int \mathrm{d}\Omega_6 \int \mathrm{d}U_5\, p\,(a_{0,5}) \int \mathrm{d}\tilde{U}\, p_4\,(\tilde{a}_0)\, \delta\left(\tilde{U}U_5U_6 - 1\right)\Big|_{\mathrm{Tr}U_6 = 2a_{0,6}}, \tag{9.35}$$

where it is now easy to integrate out $\tilde{U} = U_6^\dagger U_5^\dagger$. If we denote by θ_{56} the angle between U_5 and U_6, the angular integral over Ω_6 contributes just a multiplicative constant and we obtain

$$\begin{aligned}\tilde{p}(a_{0,6}) \propto & \int_\alpha^1 \mathrm{d}a_{0,5} \sqrt{1 - a_{0,5}^2} \\ & \times \int_{-1}^1 \mathrm{d}\cos\theta_{56}\, p(a_{0,5}) p_4 \left(a_{0,5}a_{0,6} - \sqrt{1 - a_{0,5}^2}\sqrt{1 - a_{0,6}^2}\cos\theta_{56}\right),\end{aligned} \tag{9.36}$$

which can be evaluated numerically in a straightforward manner. In the end, since there are $2(d-2)$ cubes sharing the plaquette P_0, and since the a priori probability for P_0 to have trace $2a_0$ is $\sqrt{1 - a_0^2}e^{\beta a_0}$, with respect to the uniform measure, we obtain for one live plaquette

$$\begin{aligned}Z_{SU(2)} &= \int_\alpha^1 \mathrm{d}a_0 \sqrt{1 - a_0^2} p(a_0) = \int_\alpha^1 \mathrm{d}a_0 \sqrt{1 - a_0^2} e^{\beta a_0} \tilde{p}(a_0)^{2(d-2)} \\ &= \int_\alpha^1 \mathrm{d}a_0 \sqrt{1 - a_0^2} e^{\beta a_0} \left(\int_\alpha^1 \mathrm{d}x \sqrt{1 - x^2} p(x) \right. \\ &\quad \left. \times \int_{-1}^1 \mathrm{d}\cos\theta\, p_4 \left(a_0 x - \sqrt{1 - a_0^2}\sqrt{1 - x^2}\cos\theta\right)\right)^{2(d-2)},\end{aligned} \tag{9.37}$$

which also defines the functional self-consistency equation for $p(a_0)$.

Results for the Wilson and topological actions can be seen in Fig. 9.7 in the left and right panels, respectively [5].

5 Our results for the mean plaquette approach differ a little from those of [17], because we imposed the Bianchi constraint exactly rather than truncating its character expansion. Surprisingly, truncation gives better results.

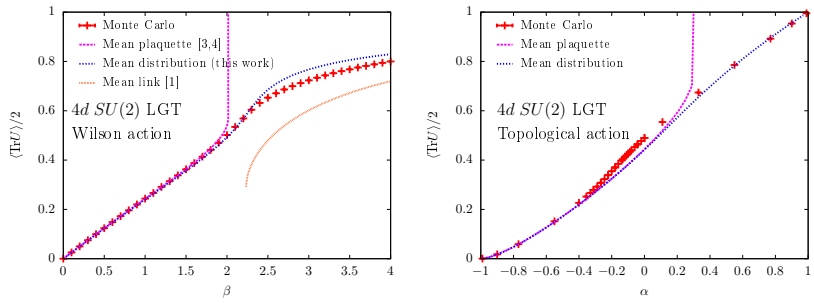

Figure 9.7: The average plaquette for the $SU(2)$ gauge theory as a function of the Wilson coupling β (*left panel*) and the restriction α (*right panel*) from Monte Carlo simulation, the mean plaquette method and the mean distribution method. For comparison the mean link result obtained with the formalism in [43] is also shown in the left panel.

For $SU(3)$ one can proceed in an analogous manner, only the angular integrals are now more involved and the trace of the plaquette depends on two diagonal generators so the resulting distribution function needs to be two dimensional.

10

DISCUSSION

In general, the quantum field theories that make up the SM of particle physics are not exactly solvable. In the strongly coupled sector of QCD one has to resort to numerical methods and if one wishes to study the system at finite density, then even the conventional numerical methods break down. That is one of the reasons why it is of interest to develop approximate methods, which aim at describing at least part of the physical properties of the model at hand. In fact, except for a few idealized situations, most physical systems appearing in nature are too complicated to solve exactly even in the numerical sense. However, as described in the main body of this thesis, we can still learn much by applying approximate methods, of which mean-field related approaches are an important sub-class. The main focus of this work has been EMFT, which can be thought of as a simplification of DMFT, a method which is widely used in condensed matter physics, a field of research which is particularly familiar with the intractability of exact solutions. This family of approximations has however, to our knowledge, not found its way into the particle physics community, although, as the content of this thesis shows, there are many situations where DMFT and in particular EMFT work excellently.

With the purpose of assessing the applicability of EMFT to QFTs we first studied the complex ϕ^4 theory, a model for which conventional Monte Carlo simulations suffer from a sign problem, but for which an exact, sign-problem free formulation can be found. It is thus possible to compare the EMFT approximation to numerically exact results in this case. We found that it works especially well in four dimensions at zero temperature where it correctly predicts a second-order phase transition with mean field exponents and a quantitatively very accurate value of the critical chemical potential. EMFT was also shown to be a computationally cheap method for probing the system at finite temperature. Although it incorrectly predicts a first-order transition due to dimensional reduction, the estimates of observables like the critical chemical potential and the density agree very well with state of the art Monte Carlo simulations [50]. These properties establish EMFT as a very

useful tool for the study of the existence and whereabouts of phase transitions, even though EMFT might have problems distinguishing a weak first-order transition from a second-order transition. Due to its simplicity and low computational cost, it can serve as a complement and guide to more sophisticated methods.

This last direction was then explored in a study of the $\mathbb{Z}_3$ spin model in three dimensions with charge-symmetry breaking external fields. The purpose of the study was to investigate the possibility that models with complex saddle points may have a complex mass spectrum and thus oscillating propagators, something which can be shown analytically in one dimension and has been conjectured to hold also in higher dimensions. The existence of these oscillating spatial correlators would have interesting implications for the phase diagram of QCD and possible experimental signatures in heavy-ion collisions.

Using unbiased Monte Carlo simulations at parameter values suggested by EMFT calculations, we have shown that the $\mathbb{Z}_3$ spin model has non-monotonic spatial correlators, both in the original spin variables and in the flux variables, for some regions in parameter space. This strongly suggests that the spectrum in these regions is complex and this claim is also backed up by EMFT calculations of the three-dimensional model. Of special interest is the oscillatory nature of the junction-junction correlator, which is the analogue of the baryon-baryon correlator in heavy-dense QCD, for some regions of parameter space. We have also shown that the worm algorithm works when the mass spectrum is complex by reproducing the exact 1-dimensional results. The phase diagram in one dimension contains regions where the system behaves like a liquid, with exponentially damped oscillations, and like a crystal with a purely oscillatory correlator. In general, it is expected [79] that these features carry over also to higher dimensions. For those regions of parameter space where the model has a sign-problem free representation we have only found evidence of the liquid phase with exponentially damped but oscillating correlations between spins, as well as between junctions. We have found no evidence of a crystalline phase and it is probable that it lies beyond the reach of the worm algorithm in three dimensions, as it does in one dimension. It should also be noted that even the liquid phase may lie in an unphysical region of parameter space. A complex mass spectrum can only be found in a parameter region where the mass M of the underlying heavy quark satisfies $M \ll T$, whereas the validity of the effective description of

QCD by a $\mathbb{Z}_3$ spin model requires $M \gg T$. This situation may change if the junctions are given a nonzero weight as in [82], but this possibility has not been investigated here. However, whatever the values of the other parameters, introducing a junction weight will further damp the signal we want to measure, making the search yet more difficult.

These findings support the claim that in general, it is plausible that models without charge-conjugation symmetry, but invariance under the combined action of charge conjugation and complex conjugation, will have regions with a complex mass spectrum in their phase diagram. However, more work is needed before precise statements can be made about whether or not this is a phenomenon which occurs under physical conditions. This first proof of principle should encourage the study of more realistic models, and the search for experimental signals in heavy-ion collisions as advocated in [82].

Next, we considered a model which contains also fermions, the Higgs-fermion sector of the SM, which is an example of a so called Higgs-Yukawa model. Since we were interested in the order of the Extended Mean Field Theory phase transition it was useful that there already exist some Monte Carlo simulations of this model [36], especially since it has been found that EMFT sometimes gets the order of the phase transition wrong. However, we found that EMFT agrees very well with the full Monte Carlo simulations, also in the region where the transition is strongly first order. Furthermore, we went beyond what is possible for Monte Carlo simulations by working directly in the thermodynamic limit and by lifting the mass degeneracy of the top and bottom quarks, something which would cause a sign problem in the Monte Carlo simulations, as well as including all other SM fermions. In the main part of the investigation we studied the EW finite temperature transition in the presence of a φ^6 term in the Higgs potential and thus obtained the critical Higgs mass for which this transition turns first order, something which has not been done non-perturbatively before. We found that with a BSM scale of about 1.5 TeV the transition turns first order for a Higgs mass of $M_h = 125$ GeV. At this point the effective model shows a separation of roughly a factor 3 between the relevant scales M_h, a^{-1} and M_{BSM}. The value of M_{BSM} decreases only slightly if we demand a strong first order transition with $\phi_c / T_c \gtrsim 1$. This scale is consistent with what is found in the gauge-Higgs model [91, 92], where the EW gauge fields are taken into account but the fermions are neglected, as well as in the perturbative study [57]. The scale is also only mildly dependent

on the exact value of the lattice cutoff $1/a$ within the window between M_h and M_{BSM}. It is however difficult to assess the effect of neglecting other higher order operators. We further showed that removing the fermions altogether shifts the critical Higgs mass by a few percent only, establishing that the Higgs sector itself is the dominating driving factor of the transition. To confirm that the gauge and fermion sectors always yield small contributions to the critical mass it would be interesting to study a model with different higher dimension operators, in particular one including both the Higgs field and the gauge fields.

On the topic of possible extensions of the SM there are of course a myriad of different suggestions. One of those is the concept of gauge-Higgs unification via the Hosotani mechanism, which requires a compact extra dimension. It has been shown using the perturbative effective potential that gauge loops winding around the extra dimension can acquire an expectation value *à la* Arahanov-Bohm and thus destabilize the classical vacuum and break the gauge symmetry. We have investigated the possibility of gauge-symmetry breaking non-perturbatively on the lattice as well as devised a procedure for diagnosing gauge-symmetry breaking to a $U(1)$ subgroup in a gauge invariant way. This is done by monitoring topological excitations, Abelian fluxes and monopoles in this case, which are stable in the $U(1)$ subgroup but decay in the full symmetry group. We found that the perturbative predictions are not spoiled by non-perturbative effects.

The general procedure is also applicable when the symmetry breaks to other subgroups, only the topological excitations to monitor changes. For example, to diagnose gauge-symmetry breaking to an $SU(2)$ subgroup, one should monitor the stability of a 't Hooft-Polyakov monopole. Finally, it is clear that our approach can be used without change to diagnose gauge-symmetry breaking in an ordinary gauge-Higgs system. Note that our construction is completely non-local, so that it does not contradict the Fradkin-Shenker argument against the existence of a local order parameter distinguishing the Higgs and the confining regimes.

Another possible extension of the SM is walking technicolor, which refers to technicolor models which show extremely slow running, hence *walking*, of the coupling due to the vicinity of a conformal fixed point. They also require large anomalous dimensions, which calls for non-perturbative methods, i.e. lattice simulations. Although a finite lattice explicitly breaks conformal invariance, some of the scale invariance is still encoded in the lattice correlator which is left invariant when

all dimensions are rescaled, i.e. all masses in the system are directly proportional to the lattice extent. We have also demonstrated how the full conformal correlator is obtained in the infinite volume limit from a continuous distribution of massive states. In the presence of a mass deformation we also found that the extraction of the mass anomalous dimension can be subject to some ambiguity when it comes to subleading effects.

In a slightly different direction, but in the same general spirit of supplementing or improving standard lattice simulations, we studied a so called "topological" action, which is constant but restricted in parameter space, and thus invariant under smooth deformations. We simulated the $U(1)$ lattice gauge theory using this type of action and found that it describes the same physics as the Wilson action, i.e. there is a confining strong coupling phase where magnetic monopoles condense and Wilson loops follow an area law, separated by a (weak) first order transition from a Coulomb phase with an exponentially suppressed monopole density and a perimeter law for the Wilson loops. We have, in this specific case, not found any concrete advantages which would motivate the choice of this action over the Wilson action although at a given value of the effective coupling in the Coulomb phase there are significantly fewer monopoles (lattice artifacts). This is in line with other known cases where a topological action reduces discretization errors [22, 21, 23]. Perhaps the most interesting approach is to search for optimized combinations of a standard action and constrained fields. For works in this direction, where the restriction is fixed to Lüscher's "admissibility condition", see [24, 49]. An interesting feature of the topological action is the direct access to the free energy itself.

One interesting open question is the nature of the extra transition at $\delta_{\max} = \pi/3$ where there is a non-analyticity in the monopole density as it goes from nonzero to strictly zero. A similar phenomenon occurs at $\delta_{\max} = \pi/2$ for an XY model, and when plaquettes become restricted by the "admissibility condition" in gauge theories. One may argue, however, in the $U(1)$ case at least, that this transition will have no impact on the physics because the monopole density close to the transition is extremely small anyway.

Finally, to come back to variations of the mean-field approximation we developed an approached dubbed the *mean distribution approach*, which self-consistently determines the whole distribution over allowed field values for a local quantity, and not only its mean value. In con-

junction, we also studied the effect of determining the mean value of different types of local variables. It has been shown before [19] that determining a self-consistent mean-link gives a much better approximation than the traditional mean-field. Furthermore, the symmetry-invariant mean link can be generalized to a mean plaquette in gauge theories [17]. Here, we have shown that the approximation can be further improved by determining the self-consistent mean distribution of links or plaquettes. The extension from a self-consistent determination of the symmetry invariant mean link or plaquette to a self-consistent determination of the entire distribution of links and plaquettes is shown to improve upon the results obtained by Batrouni in his seminal work [17, 18]. Especially appealing is the fact that the mean distribution approach yields a non-trivial result for the whole range of couplings and not just in the strong coupling regime, which is sometimes the case for the mean link/plaquette approach, or just in the weak coupling regime which is accessible to the mean field treatment of [43]. Indeed, the mean distribution approach gives a nearly correct answer when the correlation length is not too large, and by enlarging the live domain the exact result is approached systematically for any value of the coupling. As the domain of live variables is enlarged, the mean link/plaquette and the mean distribution results tend to approach each other but since determining the full mean distribution does not require much additional computer time it should always be desirable to do so.

Furthermore, another appealing feature of the mean distribution approach is that once the distribution has been self-consistently determined, other local observables, like the vortex or monopole densities become readily available. Finally, the whole approach applies to non-Abelian models as well.

10.1 OUTLOOK

One of the most interesting directions in which to further develop EMFT or DMFT is the inclusion of gauge fields such that the method can be applied to the gauge theories of the SM. Since the gauge fields interact via plaquettes a small cluster of live sites would be needed in the formulation. The concept of cluster DMFT is however already widely used in the condensed matter community, so no new knowledge is actually needed in that regard. However, it seems a non-trivial fact to construct the non-local effective action in terms of only gauge-invariant

objects. Furthermore, since the propagator enters explicitly in the self-consistency equations, one would ideally need an analytic expression for it in some limit of the theory. It is unclear what that would be. A simpler option may be to abandon the group-valued gauge links of lattice gauge theory and work directly with the Lie-algebra fields of the continuum formulation. The downside of this approach is that gauge fixing is needed in order to properly define the gauge propagators, and since the effective action will be approximate, it is not to be expected that the final result will be independent of the gauge-fixing parameter.

However, as discussed in the introduction there are yet many interesting models where EMFT can be applied, either as the principal method of investigation, or as a first probe before computationally more expensive methods are applied. The same can be said about the mean distribution approach. The main direction of improvement would be to also include matter fields into the self-consistency equations, so that physically more relevant models can be studied.

When it comes to the more concrete results presented in this thesis, the most interesting is probably the one about the Higgs-Yukawa model. It is clear that the model studied here is a crude simplification of the full SM plus a generic UV completion. There are gauge interactions missing as well as many other possible dimension six operators, and then of course all higher dimension operators. There is also some room to vary the exact value of the Wilson coefficients, but the general result that the mass scale needed to make the EWFT phase transition first order, and thus EW baryogenesis viable, can not be too high should be valid. If this scenario is actually realized in nature, then it should be detectable at the LHC, either by direct detection of the state responsible for the effective ϕ^6 operator, or as indirect deviations from SM predictions due to other higher dimension operators.

BIBLIOGRAPHY

[1] Gert Aarts. „Can stochastic quantization evade the sign problem? The relativistic Bose gas at finite chemical potential." In: *Phys. Rev. Lett.* 102 (2009), p. 131601. arXiv: 0810.2089 [hep-lat] (cit. on pp. 2, 43).

[2] Gert Aarts. „Complex Langevin dynamics at finite chemical potential: Mean field analysis in the relativistic Bose gas." In: *JHEP* 05 (2009), p. 052. arXiv: 0902.4686 [hep-lat] (cit. on pp. 43, 51).

[3] Gert Aarts, Lorenzo Bongiovanni, Erhard Seiler, Denes Sexty, and Ion-Olimpiu Stamatescu. „Controlling complex Langevin dynamics at finite density." In: *Eur. Phys. J. A* 49 (2013), p. 89. arXiv: 1303.6425 [hep-lat] (cit. on p. 2).

[4] Oscar Akerlund and Philippe de Forcrand. „Deformations of infrared-conformal theories in two dimensions." In: *PoS* LATTICE2014 (2014), p. 243. arXiv: 1410.1178 [hep-lat] (cit. on pp. vii, 105).

[5] Oscar Akerlund and Philippe de Forcrand. „Gauge-invariant signatures of spontaneous gauge symmetry breaking by the Hosotani mechanism." In: *PoS* LATTICE2014 (2015), p. 272. arXiv: 1503.00429 [hep-lat] (cit. on pp. vii, 95).

[6] Oscar Akerlund and Philippe de Forcrand. „Higgs-Yukawa model with higher dimension operators via extended mean field theory." In: *Phys. Rev. D* 93.3 (2016), p. 035015. arXiv: 1508.07959 [hep-lat] (cit. on pp. vii, 77).

[7] Oscar Akerlund and Philippe de Forcrand. „Mean Distribution Approach to Spin and Gauge Theories." In: *Nucl. Phys. B* 905 (2016), pp. 1–15. arXiv: 1601.01175 [hep-lat] (cit. on pp. vii, 133).

[8] Oscar Akerlund and Philippe de Forcrand. „U(1) lattice gauge theory with a topological action." In: *JHEP* 06 (2015), p. 183. arXiv: 1505.02666 [hep-lat] (cit. on pp. vii, 115).

[9] Oscar Akerlund, Philippe de Forcrand, Antione Georges, and Philipp Werner. „Extended Mean Field study of complex ϕ^4-theory at finite density and temperature." In: *Phys. Rev. D* 90 (6 Sept. 2014), p. 065008. arXiv: 1405.6613 [hep-lat]. URL: http://link.aps.org/doi/10.1103/PhysRevD.90.065008 (cit. on pp. vii, 41, 64, 65).

[10] Oscar Akerlund, Philippe de Forcrand, Antoine Georges, and Philipp Werner. „Dynamical Mean Field Approximation Applied to Quantum Field Theory." In: *Phys. Rev. D* 88 (2013), p. 125006. arXiv: 1305.7136 [hep-lat] (cit. on pp. vii, 2, 30, 36, 51).

[11] Oscar Akerlund, Philippe de Forcrand, and Tobias Rindlisbacher. „Oscillating propagators in heavy-dense QCD." In: (2016). Submitted to JHEP. arXiv: 1602.02925 [hep-lat] (cit. on pp. vii, 59).

[12] Mark G. Alford, S. Chandrasekharan, J. Cox, and U. J. Wiese. „Solution of the complex action problem in the Potts model for dense QCD." In: *Nucl. Phys. B* 602 (2001), pp. 61–86. arXiv: hep-lat/0101012 [hep-lat] (cit. on p. 60).

[13] Peter Anders, Emanuel Gull, Lode Pollet, Matthias Troyer, and Philipp Werner. „Dynamical Mean Field Solution of the Bose-Hubbard Model." In: *Phys. Rev. Lett.* 105 (9 Aug. 2010), p. 096402. URL: http://link.aps.org/doi/10.1103/PhysRevLett.105.096402 (cit. on p. 24).

[14] Peter Anders, Emanuel Gull, Lode Pollet, Matthias Troyer, and Philipp Werner. „Dynamical mean-field theory for bosons." In: *New Journal of Physics* 13.7 (2011), p. 075013. URL: http://stacks.iop.org/1367-2630/13/i=7/a=075013 (cit. on p. 24).

[15] Peter Anders, Philipp Werner, Matthias Troyer, Manfred Sigrist, and Lode Pollet. „From the Cooper Problem to Canted Supersolids in Bose-Fermi Mixtures." In: *Phys. Rev. Lett.* 109 (20 Nov. 2012), p. 206401. URL: http://link.aps.org/doi/10.1103/PhysRevLett.109.206401 (cit. on p. 24).

[16] Y. Aoki, F. Csikor, Z. Fodor, and A. Ukawa. „The Endpoint of the first order phase transition of the SU(2) gauge Higgs model on

a four-dimensional isotropic lattice.“ In: *Phys. Rev. D* 60 (1999), p. 013001. arXiv: hep-lat/9901021 [hep-lat] (cit. on p. 6).

[17] Ghassan G. Batrouni. „Gauge Invariant Mean Plaquette Method for Lattice Gauge Theories.“ In: *Nucl. Phys. B* 208 (1982), p. 12 (cit. on pp. 10, 138, 146, 154).

[18] Ghassan G. Batrouni. „Plaquette Formulation and the Bianchi Identity for Lattice Gauge Theories.“ In: *Nucl. Phys. B* 208 (1982), p. 467 (cit. on pp. 10, 11, 154).

[19] Ghassan George Batrouni, Elbio Dagotto, and Adriana Moreo. „Mean Link Analysis of Lattice Spin Models.“ In: *Phys. Lett. B* 155 (1985), p. 263 (cit. on pp. 138, 139, 154).

[20] Bernd A Berg. *Markov Chain Monte Carlo Simulations and Their Statistical Analysis*. World Scientific, Oct. 2004 (cit. on p. 18).

[21] W. Bietenholz, M. Bögli, F. Niedermayer, M. Pepe, F. G. Rejón-Barrera, and U.-J. Wiese. „Topological Lattice Actions for the 2d XY Model.“ In: *JHEP* 1303 (2013), p. 141. arXiv: 1212.0579 [hep-lat] (cit. on pp. 9, 153).

[22] W. Bietenholz, U. Gerber, M. Pepe, and U.-J. Wiese. „Topological Lattice Actions.“ In: *JHEP* 1012 (2010), p. 020. arXiv: 1009.2146 [hep-lat] (cit. on pp. 8, 9, 123, 135, 153).

[23] W. Bietenholz, U. Gerber, and F. G. Rejón-Barrera. „Berezinskii–Kosterlitz–Thouless transition with a constraint lattice action.“ In: *J. Stat. Mech.* 2013 (2013), P12009. arXiv: 1307.0485 [hep-lat] (cit. on pp. 9, 120, 125, 153).

[24] Wolfgang Bietenholz, K. Jansen, K.-I. Nagai, S. Necco, L. Scorzato, and S. Shcheredin. „Exploring topology conserving gauge actions for lattice QCD.“ In: *JHEP* 0603 (2006), p. 017. arXiv: hep-lat/0511016 [hep-lat] (cit. on p. 153).

[25] Jacques Bloch, Falk Bruckmann, and Tilo Wettig. „Subset method for one-dimensional QCD.“ In: *JHEP* 10 (2013), p. 140. arXiv: 1307.1416 [hep-lat] (cit. on p. 1).

[26] Christian Borgs and Roman Kotecky. „Finit size effects at asymmetric first order phase transitions.“ In: *Phys. Rev. Lett.* 68 (1992), pp. 1734–1737 (cit. on p. 126).

[27] V.G. Bornyakov, Michael Creutz, and V.K. Mitrjushkin. „Modified Wilson action and Z(2) artifacts in SU(2) lattice gauge theory.“ In: *Phys. Rev. D* 44 (1991), pp. 3918–3923 (cit. on p. 8).

[28] Vincenzo Branchina, Emanuele Messina, and Marc Sher. „Lifetime of the electroweak vacuum and sensitivity to Planck scale physics.“ In: *Phys. Rev. D* 91 (2015), p. 013003. arXiv: 1408.5302 [hep-ph] (cit. on p. 5).

[29] Steve Brooks, Andrew Gelman, Galin Jones, and Xiao-Li Meng, eds. *Handbook of Markov Chain Monte Carlo*. Chapman & Hall/CRC Handbooks of Modern Statistical Methods. Chapman and Hall/CRC, 2011 (cit. on p. 18).

[30] J. Budczies and M.R. Zirnbauer. „Howe duality for an induced model of lattice U(N) Yang-Mills theory.“ In: (2003). arXiv: math-ph/0305058 [math-ph] (cit. on p. 121).

[31] J. Bulava, K. Jansen, and A. Nagy. „Constraining a fourth generation of quarks: non-perturbative Higgs boson mass bounds.“ In: *Phys. Lett. B* 723 (2013), pp. 95–99. arXiv: 1301.3416 [hep-lat] (cit. on p. 6).

[32] John Bulava, Philipp Gerhold, Karl Jansen, Jim Kallarackal, Bastian Knippschild, C. -J. David Lin, Kei-Ichi Nagai, Attila Nagy, and Kenji Ogawa. „Higgs-Yukawa model in chirally-invariant lattice field theory.“ In: *Adv. High Energy Phys.* 2013 (2013), p. 875612. arXiv: 1210.1798 [hep-lat] (cit. on p. 6).

[33] Krzysztof Byczuk and Dieter Vollhardt. „Correlated bosons on a lattice: Dynamical mean-field theory for Bose-Einstein condensed and normal phases.“ In: *Phys. Rev. B* 77 (23 June 2008), p. 235106. URL: http://link.aps.org/doi/10.1103/PhysRevB.77.235106 (cit. on p. 24).

[34] Paolo Cea and Leonardo Cosmai. „A Gauge invariant study of the monopole condensation in nonAbelian lattice gauge theories.“ In: *Phys. Rev. D* 62 (2000), p. 094510. arXiv: hep-lat/0006007 [hep-lat] (cit. on p. 102).

[35] Shailesh Chandrasekharan. „Fermion Bag Approach to Fermion Sign Problems.“ In: *Eur. Phys. J. A* 49 (2013), p. 90. arXiv: 1304.4900 [hep-lat] (cit. on p. 1).

[36] David Y. -J. Chu, Karl Jansen, Bastian Knippschild, C. -J. David Lin, and Attila Nagy. „A lattice study of a chirally invariant Higgs–Yukawa model including a higher dimensional ϕ^6-term.“ In: *Phys. Lett. B* 744 (2015), pp. 146–152. arXiv: 1501.05440 [hep-lat] (cit. on pp. 6, 84, 89, 151).

[37] Thomas D . Cohen. „Functional integrals for QCD at nonzero chemical potential and zero density.“ In: *Phys. Rev. Lett.* 91 (2003), p. 222001. arXiv: hep-ph/0307089 [hep-ph] (cit. on p. 48).

[38] Jac Condella and Carleton E. Detar. „Potts flux tube model at nonzero chemical potential.“ In: *Phys. Rev. D* 61 (2000), p. 074023. arXiv: hep-lat/9910028 [hep-lat] (cit. on pp. 59, 60, 66, 67).

[39] Guido Cossu and Massimo D'Elia. „Finite size phase transitions in QCD with adjoint fermions.“ In: *JHEP* 07 (2009), p. 048. arXiv: 0904.1353 [hep-lat] (cit. on p. 96).

[40] Guido Cossu, Hisaki Hatanaka, Yutaka Hosotani, and Jun-Ichi Noaki. „Polyakov loops and the Hosotani mechanism on the lattice.“ In: *Phys. Rev. D* 89.9 (2014), p. 094509. arXiv: 1309.4198 [hep-lat] (cit. on p. 98).

[41] F. Csikor, Z. Fodor, and J. Heitger. „Endpoint of the hot electroweak phase transition.“ In: *Phys. Rev. Lett.* 82 (1999), pp. 21–24. arXiv: hep-ph/9809291 [hep-ph] (cit. on p. 6).

[42] Thomas A. DeGrand and Doug Toussaint. „Topological Excitations and Monte Carlo Simulation of Abelian Gauge Theory.“ In: *Phys. Rev. D* 22 (1980), p. 2478 (cit. on pp. 9, 117).

[43] Jean-Michel Drouffe and Jean-Bernard Zuber. „Strong Coupling and Mean Field Methods in Lattice Gauge Theories.“ In: *Phys. Rept.* 102 (1983), p. 1 (cit. on pp. 9, 11, 147, 154).

[44] Astrid Eichhorn, Holger Gies, Joerg Jaeckel, Tilman Plehn, Michael M. Scherer, and René Sondenheimer. „The Higgs Mass and the Scale of New Physics.“ In: *JHEP* 04 (2015), p. 022. arXiv: 1501.02812 [hep-ph] (cit. on pp. 6, 78, 89).

[45] Michael G. Endres. „Method for simulating O(N) lattice models at finite density.“ In: *Phys. Rev. D* 75 (2007), p. 065012. arXiv: hep-lat/0610029 [hep-lat] (cit. on pp. 2, 43).

[46] J. R. Espinosa and M. Quiros. „Improved metastability bounds on the standard model Higgs mass.“ In: *Phys. Lett. B* 353 (1995), pp. 257–266. arXiv: hep-ph/9504241 [hep-ph] (cit. on p. 5).

[47] J. Fingberg, Urs M. Heller, and V.K. Mitrjushkin. „Scaling in the positive plaquette model and universality in SU(2) lattice gauge theory.“ In: *Nucl. Phys. B* 435 (1995), pp. 311–338. arXiv: hep-lat/9407011 [hep-lat] (cit. on p. 8).

[48] Philippe de Forcrand and Urs Wenger. „New baryon matter in the lattice Gross-Neveu model.“ In: *PoS* LAT2006 (2006), p. 152. arXiv: hep-lat/0610117 [hep-lat] (cit. on p. 3).

[49] Hidenori Fukaya, Shoji Hashimoto, Takuya Hirohashi, Kenji Ogawa, and Tetsuya Onogi. „Topology conserving gauge action and the overlap-Dirac operator.“ In: *Phys. Rev. D* 73 (2006), p. 014503. arXiv: hep-lat/0510116 [hep-lat] (cit. on p. 153).

[50] Christof Gattringer and Thomas Kloiber. „Lattice study of the Silver Blaze phenomenon for a charged scalar ϕ^4 field.“ In: *Nucl. Phys. B* 869 (2013), pp. 56–73. arXiv: 1206.2954 [hep-lat] (cit. on pp. 2, 41, 43, 51, 53–55, 149).

[51] Christof Gattringer and Thomas Kloiber. „Spectroscopy in finite density lattice field theory: An exploratory study in the relativistic Bose gas.“ In: *Phys. Lett. B* 720 (2013), pp. 210–214. arXiv: 1212.3770 [hep-lat] (cit. on p. 62).

[52] Antoine Georges. „Strongly correlated electron materials: Dynamical mean-field theory and electronic structure.“ 2004 (cit. on p. 23).

[53] Antoine Georges, Gabriel Kotliar, Werner Krauth, and Marcelo J. Rozenberg. „Dynamical mean-field theory of strongly correlated fermion systems and the limit of infinite dimensions.“ In: *Rev. Mod. Phys.* 68 (1 Jan. 1996), pp. 13–125. URL: http://link.aps.org/doi/10.1103/RevModPhys.68.13 (cit. on pp. 23, 25).

[54] Howard Georgi and Yevgeny Kats. „Unparticle self-interactions.“ In: *JHEP* 02 (2010), p. 065. arXiv: 0904.1962 [hep-ph] (cit. on p. 110).

[55] Holger Gies, Clemens Gneiting, and René Sondenheimer. „Higgs Mass Bounds from Renormalization Flow for a simple Yukawa model.“ In: *Phys. Rev. D* 89.4 (2014), p. 045012. arXiv: 1308.5075 [hep-ph] (cit. on pp. 6, 89).

[56] Holger Gies and René Sondenheimer. „Higgs Mass Bounds from Renormalization Flow for a Higgs-top-bottom model.“ In: *Eur. Phys. J. C* 75.2 (2015), p. 68. arXiv: 1407.8124 [hep-ph] (cit. on pp. 6, 89).

[57] Christophe Grojean, Geraldine Servant, and James D. Wells. „First-order electroweak phase transition in the standard model with a low cutoff.“ In: *Phys. Rev. D* 71 (2005), p. 036001. arXiv: hep-ph/0407019 [hep-ph] (cit. on pp. 6, 90, 151).

[58] B. Grzadkowski, M. Iskrzynski, M. Misiak, and J. Rosiek. „Dimension-Six Terms in the Standard Model Lagrangian.“ In: *JHEP* 10 (2010), p. 085. arXiv: 1008.4884 [hep-ph] (cit. on p. 78).

[59] Emanuel Gull, Andrew J. Millis, Alexander I. Lichtenstein, Alexey N. Rubtsov, Matthias Troyer, and Philipp Werner. „Continuous-time Monte Carlo methods for quantum impurity models.“ In: *Rev. Mod. Phys.* 83 (2 May 2011), pp. 349–404. URL: http://link.aps.org/doi/10.1103/RevModPhys.83.349 (cit. on p. 24).

[60] Prasad Hegde, Karl Jansen, C. -J. David Lin, and Attila Nagy. „Stabilizing the electroweak vacuum by higher dimensional operators in a Higgs-Yukawa model.“ In: *PoS* LATTICE2013 (2014), p. 058. arXiv: 1310.6260 [hep-lat] (cit. on pp. 6, 84, 85).

[61] James E. Hetrick. „Lattice Investigations of the Hosotani Mechanism of Spontaneous Symmetry Breaking.“ In: *PoS* LATTICE2013 (2014), p. 102 (cit. on p. 97).

[62] Yutaka Hosotani. „Dynamical Gauge Symmetry Breaking as the Casimir Effect.“ In: *Phys. Lett. B* 129 (1983), p. 193 (cit. on pp. 7, 95).

[63] Yutaka Hosotani. „Dynamical Mass Generation by Compact Extra Dimensions.“ In: *Phys. Lett. B* 126 (1983), p. 309 (cit. on pp. 7, 95).

[64] Nikos Irges and Francesco Knechtli. „Mean-Field Gauge Interactions in Five Dimensions I. The Torus.“ In: *Nucl. Phys. B* 822 (2009). [Erratum: Nucl. Phys. B 840, 438(2010)], pp. 1–44. arXiv: 0905.2757 [hep-lat] (cit. on p. 10).

[65] K. -I. Ishikawa, Y. Iwasaki, Yu Nakayama, and T. Yoshie. „Global Structure of Conformal Theories in the SU(3) Gauge Theory.“ In: *Phys. Rev. D* 89.11 (2014), p. 114503. arXiv: 1310.5049 [hep-lat] (cit. on p. 106).

[66] C. Itzykson and J.M. Drouffe. *Statistical Field Theory: Volume 2, Strong Coupling, Monte Carlo Methods, Conformal Field Theory and Random Systems*. Cambridge Monographs on Mathematical Physics v. 2. Cambridge University Press, 1991. URL: https://books.google.ch/books?id=T2BX%5C_85ZR9QC (cit. on p. 107).

[67] K. Kajantie, M. Laine, K. Rummukainen, and Mikhail E. Shaposhnikov. „Is there a hot electroweak phase transition at m(H) larger or equal to m(W)?“ In: *Phys. Rev. Lett.* 77 (1996), pp. 2887–2890. arXiv: hep-ph/9605288 [hep-ph] (cit. on p. 6).

[68] Pavel Kovtun, Mithat Unsal, and Laurence G. Yaffe. „Volume independence in large N(c) QCD-like gauge theories.“ In: *JHEP* 06 (2007), p. 019. arXiv: hep-th/0702021 [HEP-TH] (cit. on p. 96).

[69] M. Lüscher. „Topology of Lattice Gauge Fields.“ In: *Commun. Math. Phys.* 85 (1982), p. 39 (cit. on p. 8).

[70] G. Mack and E. Pietarinen. „Monopoles, Vortices, and Confinement.“ In: *Nucl. Phys. B* 205 (1982), p. 141 (cit. on p. 8).

[71] Peter N. Meisinger, Michael C. Ogilvie, and Timothy D. Wiser. „PT Symmetry and the Sign Problem.“ In: (2010). arXiv: 1009.0745 [hep-th] (cit. on pp. 3, 4, 59).

[72] Ydalia Delgado Mercado, Hans Gerd Evertz, and Christof Gattringer. „Worm algorithms for the 3-state Potts model with magnetic field and chemical potential.“ In: *Comput. Phys. Commun.* 183 (2012), pp. 1920–1927. arXiv: 1202.4293 [hep-lat] (cit. on p. 68).

[73] Y. Meurice. „A Simple method to make asymptotic series of Feynman diagrams converge.“ In: *Phys. Rev. Lett.* 88 (2002), p. 141601. arXiv: hep-th/0103134 [hep-th] (cit. on p. 8).

[74] Christopher Michael and M. Teper. „Universality and Scaling in SU(2) Lattice Gauge Theory.“ In: *Nucl. Phys. B* 305 (1988), p. 453 (cit. on p. 8).

[75] Joyce C. Myers and Michael C. Ogilvie. „New phases of SU(3) and SU(4) at finite temperature.“ In: *Phys. Rev. D* 77 (2008), p. 125030. arXiv: 0707.1869 [hep-lat] (cit. on p. 100).

[76] David R. Nelson and J.M. Kosterlitz. „Universal Jump in the Superfluid Density of Two-Dimensional Superfluids.“ In: *Phys. Rev. Lett.* 39 (1977), pp. 1201–1205 (cit. on p. 119).

[77] Herbert Neuberger. „Exactly massless quarks on the lattice.“ In: *Phys. Lett. B* 417 (1998), pp. 141–144. arXiv: hep-lat/9707022 [hep-lat] (cit. on p. 79).

[78] Hiromichi Nishimura, Michael C. Ogilvie, and Kamal Pangeni. „Complex Saddle Points and Disorder Lines in QCD at finite temperature and density.“ In: *Phys. Rev. D* 91.5 (2015), p. 054004. arXiv: 1411.4959 [hep-ph] (cit. on p. 3).

[79] Hiromichi Nishimura, Michael C. Ogilvie, and Kamal Pangeni. „Complex spectrum of finite-density lattice QCD with static quarks at strong coupling.“ In: (2015). arXiv: 1512.09131 [hep-lat] (cit. on pp. 3, 4, 59, 63, 73, 150).

[80] Sergey Pankov, Gabriel Kotliar, and Yukitoshi Motome. „Semiclassical analysis of extended dynamical mean-field equations.“ In: *Phys. Rev. B* 66 (4 July 2002), p. 045117. URL: http://link.aps.org/doi/10.1103/PhysRevB.66.045117 (cit. on pp. 2, 30, 36).

[81] Apoorva Patel. „A Flux Tube Model of the Finite Temperature Deconfining Transition in QCD.“ In: *Nucl. Phys. B* 243 (1984), p. 411 (cit. on pp. 3, 59).

[82] Apoorva Patel. „Flux Tube Model Signals for Baryon Correlations in Heavy Ion Collisions.“ In: *Phys. Rev. D* 85 (2012), p. 114019. arXiv: 1111.0177 [hep-ph] (cit. on pp. 3, 59, 151).

[83] Apoorva Patel. „More on the Flux Tube Model of the Deconfining Transition.“ In: *Phys. Lett. B* 139 (1984), p. 394 (cit. on pp. 3, 59).

[84] M. Potthoff. „Self-energy-functional approach to systems of correlated electrons.“ In: *Eur. Phys. J. B* 32 (Apr. 2003), pp. 429–436. eprint: cond-mat/0301137 (cit. on p. 47).

[85] Tobias Rindlisbacher and Philippe de Forcrand. „Lattice simulation of the SU(2) chiral model at zero and non-zero pion density.“ In: vol. LAT2015. 2015. arXiv: 1512.05684 [hep-lat]. URL: http://inspirehep.net/record/1410093/files/arXiv:1512.05684.pdf (cit. on pp. 62, 68).

[86] Tobias Rindlisbacher and Philippe de Forcrand. „Sampling of General Correlators in Worm Algorithm-based Simulations.“ In: (2016). arXiv: 1602.09017 [hep-lat] (cit. on p. 68).

[87] Philipp Rüfenacht and Urs Wenger. „Classically perfect gauge actions on anisotropic lattices.“ In: *Nucl. Phys. B* 616 (2001), pp. 163–214. arXiv: hep-lat/0108005 [hep-lat] (cit. on p. 8).

[88] Erhard Seiler, Denes Sexty, and Ion-Olimpiu Stamatescu. „Gauge cooling in complex Langevin for QCD with heavy quarks.“ In: *Phys. Lett. B* 723 (2013), pp. 213–216. arXiv: 1211.3709 [hep-lat] (cit. on p. 2).

[89] P. Sikivie, Leonard Susskind, Mikhail B. Voloshin, and Valentin I. Zakharov. „Isospin Breaking in Technicolor Models.“ In: *Nucl. Phys. B* 173 (1980), p. 189 (cit. on p. 79).

[90] Charles M Sommerfield. „On the definition of currents and the action principle in field theories of one spatial dimension.“ In: *Annals of Physics* 26.1 (1964), pp. 1–43. URL: http://www.sciencedirect.com/science/article/pii/0003491664902738 (cit. on pp. 109, 110).

[91] Jakob Steinbauer. „Lattice investigations of the Electroweak phase transition in the Standard Model and beyond.“ MA thesis. Zurich, Switzerland: ETH Zurich, 2015 (cit. on pp. 6, 90, 94, 151).

[92] Jakob Steinbauer and Philippe de Forcrand. In: (). in preparation (cit. on pp. 6, 90, 94, 151).

[93] M. A. Stephanov. „Deconstruction of Unparticles.“ In: *Phys. Rev. D* 76 (2007), p. 035008. arXiv: 0705.3049 [hep-ph] (cit. on p. 106).

[94] K. Symanzik. „Continuum Limit and Improved Action in Lattice Theories. 2. O(N) Nonlinear Sigma Model in Perturbation Theory.“ In: *Nucl. Phys. B* 226 (1983), p. 205 (cit. on p. 7).

[95] Michael Thies. „From relativistic quantum fields to condensed matter and back again: Updating the Gross-Neveu phase diagram.“ In: *J. Phys. A* 39 (2006), pp. 12707–12734. arXiv: hep-th/0601049 [hep-th] (cit. on p. 3).

[96] Matthias Troyer and Uwe-Jens Wiese. „Computational complexity and fundamental limitations to fermionic quantum Monte Carlo simulations.“ In: *Phys. Rev. Lett.* 94 (2005), p. 170201. arXiv: cond-mat/0408370 [cond-mat] (cit. on p. 20).

[97] Mithat Unsal and Laurence G. Yaffe. „(In)validity of large N orientifold equivalence.“ In: *Phys. Rev. D* 74 (2006), p. 105019. arXiv: hep-th/0608180 [hep-th] (cit. on p. 96).

[98] Michele Vettorazzo and Philippe de Forcrand. „Electromagnetic fluxes, monopoles, and the order of the 4-d compact U(1) phase transition.“ In: *Nucl. Phys. B* 686 (2004), pp. 85–118. arXiv: hep-lat/0311006 [hep-lat] (cit. on pp. 101, 120, 126).

[99] P. Weisz. „Continuum Limit Improved Lattice Action for Pure Yang-Mills Theory. 1.“ In: *Nucl. Phys. B* 212 (1983), p. 1 (cit. on p. 7).

[100] Kenneth G. Wilson. „Confinement of quarks.“ In: *Phys. Rev. D* 10 (8 Oct. 1974), pp. 2445–2459. URL: http://link.aps.org/doi/10.1103/PhysRevD.10.2445 (cit. on p. 1).

NOTATION

MATHEMATICAL OBJECTS

SYMBOL	MEANING
Z	Partition function
S	Action
$G(x)$	Bosonic propagator in coordinate space
$\widetilde{G}(k)$	Bosonic propagator in Fourier space
$S(x)$	Fermionic propagator in coordinate space
$\widetilde{S}(k)$	Fermionic propagator in Fourier space
Σ	Self-energy
$p(x)$	Probability distribution
μ	Chemical potential
f	Free energy density

LATTICE PARAMETERS

SYMBOL	MEANING
a	Lattice spaing
N	Total number of lattice sites
N_ν	Number of lattice sites in ν direction
V	Lattice volume
L_ν	Lattice extent in ν direction
z	Number of nearest neighbors
$\hat{k}$	lattice momenum
$\hat{\nu}$	Unit vector in ν direction

ACRONYMS

MF	mean field
DMFT	Dynamical Mean Field Theory
EMFT	Extended Mean Field Theory
QFT	quantum field theory
LHC	Large Hadron Collider
SM	Standard Model
EWFT	electroweak finite temperature
EW	electroweak
UV	ultraviolet
IR	infrared
BSM	beyond the Standard Model
FRG	Functional Renormalization Group
QCD	quantum chromodynamics
QGP	quark-gluon plasma
GN	Gross-Neveu
PNJL	Polyakov-Nambu-Jona Lasinio
MCMC	Markov Chain Monte Carlo
CEP	Contraint Effective Potential

COLOPHON

This document was typeset in LaTeX using the typographical look-and-feel `classicthesis`. Most of the graphics in this thesis are generated using `gnuplot`. The bibliography is typeset using `biblatex`.